Facoltà di Scienze Matematiche, Fisiche e Naturali

Corso di Laurea magistrale in Fisica

Tesi di Laurea Magistrale

NON-EQUILIBRIUM COHERENT DYNAMICS OF CORRELATED SYSTEMS

Relatore:

Prof. Claudio Giannetti

Correlatori:

Dott. Adriano Amaricci

Prof. Fausto Borgonovi

Prof. Massimo Capone

Candidato:

Matteo Zendra

Matricola: 4810473

A mia madre

Contents

Introduction

In the last years, the ultra-fast dynamics of quantum materials driven out of equilibrium by electrostatic fields or strong laser pulses has experienced a constant growing interest [1][2][3][4]. The opportunity to investigate the non-equilibrium physics of strongly correlated electron systems on the femtosecond time scale was supported by the increasing development of the new laser technologies, able to generate ultra-short pulses with a temporal duration of few femtoseconds. These types of lasers, characterized by a high irradiance, have opened the way to new experiments and theoretical studies on both equilibrium and non-equilibrium strongly correlated systems. Actually, new striking phenomena such as photo-induced Mott transition [5] or Wannier-Stark dynamical localization [6] can arise in these systems, determined by the interplay between electronic correlations and external electromagnetic fields. Moreover, a very important role is played by the thermalization dynamics of these correlated systems, that takes place at different time scales, according to the microscopical processes the system is experiencing. Indeed, the recent advances in ultra-fast science allow us to resolve in time these processes, disentangling the intertwined electronic and lattice processes.

In particular, the ultimate goal of this thesis is to investigate the effects of combining a static electric field and an intense pulse field on the electric transport in a strongly correlated metal. We tune the coupling with an external heat bath, which provides a dissipation mechanism, in order to move from coherent to diffusive transport regime. The interplay between the coupling with the heat bath, the combination of different electromagnetic fields and the electronic interaction determines the non-equilibrium dynamics of the system, as well as its physical properties.

In order to study the dynamics of strongly correlated metals under the effect of external electromagnetic fields, we use the non-equilibrium dynamical mean-field theory (NEQ-DMFT) theoretical approach. We consider a bidimensional Hubbard model, looking at the excitation and relaxation processes caused by the coupling with a superposition of DC and pulse fields, as well as with the external heat bath.

We find that not only a DC [7][8], but also an intense pulse field can drive a transient *dimensional crossover* effect, leading the system to behave as a lower dimensional equilibrium Hubbard model in the direction orthogonal to the pulse. We discover that the superposition of a strong laser pulse with an orthogonally-directed DC probe allows to obtain an excess of flowing current in the probe field direction, and we study its dependence on the system's localization (provided by the electronic interaction U) and coherence (provided by the coupling with the external bath). Despite lots of non-equilibrium phenomena occurring in strongly correlated materials have not been understood yet, this work can pave the way to further investigations about the dynamics of these systems, with the final aim of controlling the coherent transport of electrons in specific materials.

CHAPTER 1

Equilibrium DMFT: general overview

In this chapter, we briefly discuss the physics of the Hubbard model, that describes the dynamics of interacting electrons in a periodic lattice. We also introduce the dynamical mean field theory (DMFT), a theoretical method used to investigate the physics of strongly correlated systems, based on a self-consistent formulation in terms of an effective single-site impurity problem. In the end, we introduce the Keldysh Green's functions formalism, and we investigate the equilibrium physics and the phase diagram of the Hubbard model, observing the metal-to-Mott insulator phase transition.

1. The Hubbard model

The Hubbard model [9][10] is the simplest model that can be used to describe the dynamics of interacting electrons in a periodic lattice made up by a regular array of fixed nuclear positions (lattice sites). Throughout the entire work, we will refer to the single-band Hubbard Hamiltonian, which represents a huge simplification, by treating the atoms in a solid as a collection of sites each with a single energy level, rather than as a very complex structure, with many different energy levels. The sites of the lattice are therefore constrained by the Pauli principle of exclusion to four configurations: empty, with a single up/down electron or double occupied by a pair of electrons. This model provides a simple way to get insight into how the interactions among electrons give rise to insulating, magnetic, or superconducting effects in a solid. The Hubbard Hamiltonian is made up by two main terms: a kinetic term mediated by the 'hopping' t, allowing for tunnelling of particles between neighbour sites of the lattice and a potential term mediated by U, consisting of an on-site Coulomb interaction, defined as:

$$(1.1) \qquad t = \int dr dr' \psi^*(r) \left[-\frac{\hbar^2}{2m} \nabla^2 + U(r, r') \right] \psi(r')$$

(1.2)
$$U = \int dr dr' |\psi(r)|^2 U(r, r') |\psi(r')|^2$$

where $\psi(r)$ are the atomic orbitals, and $U(r, r')$ is the potential of the crystal lattice. In the Hubbard Hamiltonian, the term mediated by U must vanish if the site is empty or contains only a single electron, and give a contribution U to the energy of the system when the single site is doubly occupied. Formalising these concepts, the Hubbard Hamiltonian reads:

(1.3)
$$H = -t \sum_{\langle ij \rangle, \sigma} \left(c_{i\sigma}^\dagger c_{j\sigma} + c_{j\sigma}^\dagger c_{i\sigma} \right) + U \sum_i n_{i\uparrow} n_{i\downarrow} - \mu \sum_i (n_{i\uparrow} + n_{i\downarrow})$$

where $c_{i\sigma}^\dagger (c_{i\sigma})$ creates (annihilates) an electron with spin σ at the site i of the lattice, $n_{i\sigma}$ is the fermionic occupation number, t is the isotropic hopping and U is the on-site Coulomb repulsion.

The physics of the Hubbard model, as visible in Figure 1.1 [10], is completely determined by the competition between the strength of the hopping integral t and the strength of the interaction term U. Looking at the first term in (1.3), a reasonable
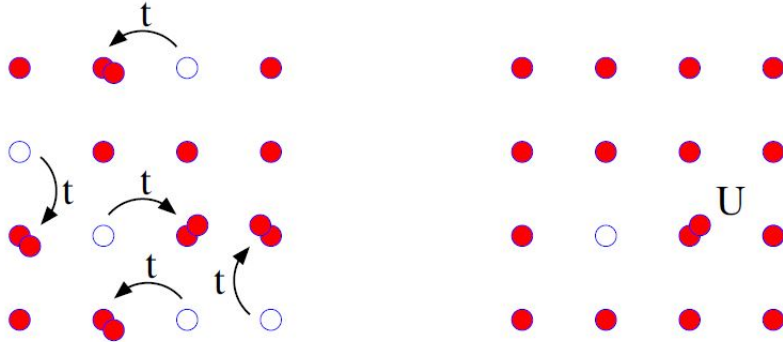

FIGURE 1.1. Pictorial representation of the main terms in the Hubbard model. On the left, the hopping integral t between nearest-neighbour sites, on the right the on-site Coulomb interaction U, when the site is doubly occupied.

representation of the kinetic energy is an expression which destroys an electron of spin σ on site j and recreates it on a neighbour site i. The energy scale which rules this hopping is t, being determined by the overlap of the wavefunctions centred at the two lattice sites, as in (1.1). Since wavefunctions are exponentially damped with the distance, we begin by allowing hopping only between adjacent sites, and express this concept with the symbol $\langle ij \rangle$. The second term of (1.3) is the interaction energy, it runs all over the sites of the lattice and adds an energy U if it finds the site

is doubly occupied. The final term in (1.3), which contains the chemical potential μ, controls the filling. We refer to the situation where there is one electron per site as *half-filling*, since the lattice contains half of the electrons it can contain (two electrons per site).

The Hubbard model is an improvement of the tight-binding model, which includes only the hopping term t and neglects the interaction U. At half filling, the tight-binding method always has a metallic solution. Instead, for strong interactions the results obtained with the model (1.3) are qualitatively different: it correctly predicts the existence of the so-called Mott insulators, transition-metal monoxides which are insulators (because of the strong repulsion between the electrons), although the are predicted to be metals by the band theory, which relies on the independent electrons approximation, which neglects the correlations at all. Throughout the entire work, we will focus on the half-filled case, because it exhibits a lot of interesting phenomena, including the Mott insulating behaviour.

Another important observation about the Hubbard Hamiltonian (1.3) is that the kinetic energy has a particle-hole symmetry. For this reason, it is useful to rewrite the Hubbard Hamiltonian in a way in which this symmetry is present also in the interaction term. Looking at the following term,

$$(1.4) \qquad U\left(n_{i\uparrow} - \frac{1}{2}\right)\left(n_{i\downarrow} - \frac{1}{2}\right) = U n_{i\uparrow} n_{i\downarrow} - \frac{U}{2}(n_{i\downarrow} + n_{i\uparrow}) + \frac{U}{4}$$

one can observe that it is unchanged under a particle-hole transformation. Moreover, the rewriting of that term differs from the original one only by a trivial shift in the chemical potential μ and an overall additive constant to the energy. By substituting (1.4) in (1.3), the Hubbard Hamiltonian can be rewritten as:

$$(1.5) \qquad H = -t \sum_{\langle ij \rangle, \sigma} \left(c^\dagger_{i\sigma} c_{j\sigma} + c^\dagger_{j\sigma} c_{i\sigma}\right) + U \sum_i \left(n_{i\uparrow} - \frac{1}{2}\right)\left(n_{i\downarrow} - \frac{1}{2}\right) - \mu \sum_i (n_{i\uparrow} + n_{i\downarrow})$$

which is completely equivalent to the original one. In particular, when $\mu = 0$, one obtains the half-filled case, and the corresponding Hamiltonian reads:

$$(1.6) \qquad H = -t \sum_{\langle ij \rangle, \sigma} \left(c^\dagger_{i\sigma} c_{j\sigma} + c^\dagger_{j\sigma} c_{i\sigma}\right) + U \sum_i \left(n_{i\uparrow} - \frac{1}{2}\right)\left(n_{i\downarrow} - \frac{1}{2}\right)$$

From (1.6), one can derive the tight-binding Hamiltonian, by considering the non-interacting limit, which reads:

$$(1.7) \qquad H = -t \sum_{\langle ij \rangle, \sigma} \left(c^\dagger_{i\sigma} c_{j\sigma} + c^\dagger_{j\sigma} c_{i\sigma}\right)$$

Firstly, we note that the Hamiltonian (1.7) commutes with the operators $N_\uparrow = \sum_i n_{i\uparrow}$ and $N_\downarrow = \sum_i n_{i\downarrow}$, which count the total number of electrons in the lattice with spin up and down, respectively. Thus, in order to find the eigenstates of (1.7), we can consider the basis of occupation number states $|10000...\rangle$, $|01000...\rangle$, $|00100...\rangle$, ... Focusing on the one dimensional sites chain, the final matrix form of H in this basis reads:

$$
(1.8) \qquad H = \begin{pmatrix}
-\mu & -t & 0 & 0 & \ldots & 0 & -t \\
-t & -\mu & -t & 0 & \ldots & 0 & 0 \\
0 & -t & -\mu & -t & \ldots & 0 & 0 \\
0 & 0 & -t & -\mu & \ldots & 0 & 0 \\
\vdots & \vdots & \vdots & \vdots & & -t & \vdots \\
0 & 0 & 0 & 0 & -t & -\mu & -t \\
-t & 0 & 0 & 0 & \ldots & -t & -\mu
\end{pmatrix}
$$

The Hamiltonian (1.8) can be diagonalized, extracting its eigenvalues $\epsilon(k) = -\mu - 2t\,cos(k)$, which is the well-known one-dimensional tight-binding dispersion. Another very important case, which will be treated throughout the entire work, is the bidimensional square lattice, whose dispersion reads:

$$
(1.9) \qquad \epsilon(k) = -2t\,(cosk_x + cosk_y)
$$

From (1.9), the energy states of the bidimensional system are distributed into a continuous band of width $8t$. The tight-binding Hamiltonian (1.7) can be written in terms of momentum space operators as:

$$
(1.10) \qquad H = \sum_{k,\sigma}(\epsilon_k - \mu)c_{k\sigma}^\dagger c_{k\sigma}
$$

where $c_{k\sigma}^\dagger$ and $c_{k\sigma}$ are the momentum creation/annihilation operators.

If the interaction $U \gg t$, its energy scale is no more negligible with respect to the bandwidth; in this case, the Hamiltonian is no more diagonalizable in the same way, and the problem turns out to be a many-body problem. For this reason, non-perturbative methods that take account of U are necessary, in order to overcome the independent electrons approximation.

Let us now briefly review the fundamental concepts of the Fermi liquid theory [9][11],

focusing in particular on the effective mass m^*. The Fermi liquid theory is a theoretical model used to describe interacting electrons systems, whose motion is altered by the interactions among the particles, generally in a very complex way. In order to quantify how the interactions affect the electronic motion, one can imagine the interacting electrons behave like free electrons, and the net effect of the interactions is to make the electrons behave as 'dressed' particles, called 'quasiparticles', with a different mass m^*, called *effective mass*. In the single-band approximation, the expression for the electronic effective mass m^* reads:

$$(1.11) \qquad \frac{1}{m^*} = \frac{1}{\hbar^2} \frac{d^2\epsilon(k)}{dk^2}$$

where $\frac{d^2\epsilon(k)}{dk^2}$ represents the curvature of the energy band. Looking at (1.9), and expanding around $k \sim 0$, the electronic effective mass reads:

$$(1.12) \qquad m^* = \frac{\hbar^2}{2t}$$

which decreases when the hopping t increases, and viceversa. Looking at (1.11), at the centre of the Brillouin zone the curvature of the dispersion can be approximated with the parabolic one, and the effective mass reduces to the bare electron mass. Instead, at the edges of the Brillouin zone, the effective mass is deeply different from the electronic one, and can become also negative.

2. Introduction to equilibrium DMFT

As introduced in the previous section, the physics of interacting particles is often very complicated, because the motion of the individual particles depends on the position of all the others. In such situations, the particles motion is said to be *correlated*. In this section, we provide an introduction to the dynamical mean-field theory (DMFT) [6], a method used to investigate the physics of strongly correlated systems. This method is the natural generalization of the Weiss mean-field theory used in classical statistical mechanics to quantum many-body problems. It treats the spatial correlations in a mean-field picture, and it is based on a self-consistent formulation in terms of an effective single-site impurity problem. In other words, it consists of mapping the lattice model into a quantum impurity problem embedded in an effective medium, determined self-consistently. In this way, the impurity model offers an intuitive picture of the local dynamics of a quantum many-body system,

while the self-consistency condition captures the translation invariance and coherence effects of the lattice. The final result is that correlations are included only on the average, and the effect of the other particles is replaced by a mean field, leaving an effective single particle problem.

The most important approximation of the DMFT method is given by the local nature of the self energy $\Sigma_{ij} = \Sigma\delta_{ij}$, which is independent on the momentum k. Thus, all spatial fluctuations are frozen, while local quantum fluctuations are taken fully into account. The hybridization between the single site and the bath is represented by a Green's function $\mathcal{G}_0(\tau - \tau')$, which is subjected to a self-consistency condition, as showed in Figure 1.2. This formalism treats the lattice as a collection of
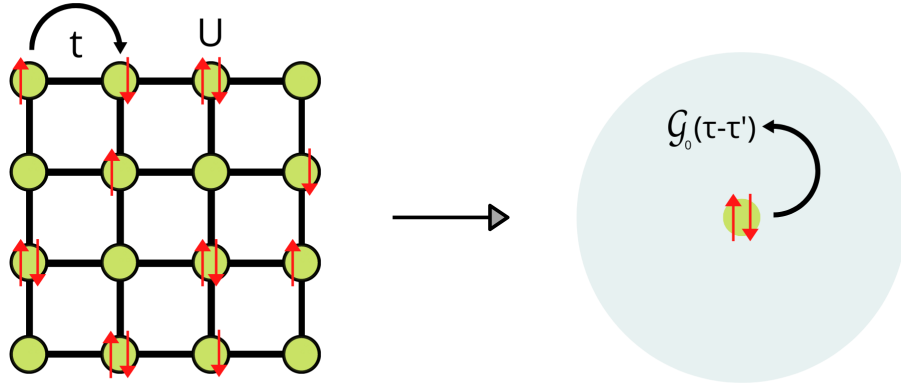
FIGURE 1.2. The DMFT maps the lattice problem (here, a square lattice with hopping integral t between nearest-neighbour sites and Coulomb interaction U for doubly occupied sites) into a quantum impurity problem embedded in a self-consistently determined bath with a hybridization function $\mathcal{G}_0(\tau-\tau')$. In equilibrium, this hybridization function depends only on the relative time $\tau - \tau'$.

atoms (sites) rather than in terms of extended Bloch states, and it is well-suited to treat strong local Coulomb interaction U (the on-site Hubbard interaction) in a non-perturbative manner.

Even if one can naively think that the reduction from a correlated lattice to a single-site impurity problem makes the problem easier, the quantum impurity model is still

a non-trivial many-body system, which needs numerical methods to be solved. Similarly to the classical statistical mechanics, DMFT becomes exact in the limit of large spatial dimensions $d \to \infty$, or more appropriately in the limit of large lattice coordination z. This ensures the internal consistency of the approach and establishes $1/z$ as a control parameter.

Many numerical methods have been implemented for the solution of the dynamical mean-field equations, such as the quantum Monte Carlo algorithm, exact diagonalization algorithms, and numerical renormalization group approaches. None of these techniques is the most appropriate, rather a combination of various numerical methods and analytical approximations are required to understand the many-body phenomena.

2.1. Dynamical mean-field theory equations.

The goal of a mean-field theory is to approximate a lattice problem with many degrees of freedom by a single-site effective problem with less degrees of freedom. The underlying physical idea is that we can treat a system of interacting particles as a system of non-interacting particles in which each particle only interacts with a 'mean field', that captures the average behaviour of the particles around it.

The simplest illustration of this idea is the Ising model [6], with ferromagnetic coupling $J_{ij} > 0$ between nearest-neighbour sites of a lattice with coordination z, whose Hamiltonian reads:

$$(1.13) \qquad\qquad H = - \sum_{\langle ij \rangle} J_{ij} S_i S_j - h \sum_i S_i$$

The Weiss mean-field theory makes each given site l as governed by an effective Hamiltonian H_{eff}:

$$(1.14) \qquad\qquad H_{eff} = -h_{eff} S_l$$

where all interactions with the other degrees of freedom can be put into the effective field h_{eff}:

$$(1.15) \qquad\qquad h_{eff} = h + \sum_i J_{li} m_i = h + zJm$$

where $m = \langle S_i \rangle$ represents the magnetization at site i, the thermodynamic mean of the spin S_i, and translation invariance has been assumed ($J_{ij} = J$ for nearest-neighbour sites, and $m_i = m$).

We have now effectively decoupled the Hamiltonian into a sum of single-body terms. Hence, h_{eff} has been related to a local quantity which can be computed from the

single-site effective model H_{eff}. For this simple case, this reads $m = tanh(\beta h_{eff})$, where $\beta = 1/(k_B T)$, which can be combined with (1.15) to obtain the well-known self-consistency mean-field equation for the magnetization:

$$(1.16) \qquad\qquad m = tanh\left[\beta(h + zJm)\right]$$

This mean-field equation is an approximation of the exact solution of the Ising model, and it becomes exact in the limit of large coordination of the lattice. In fact, it is quite intuitive that the neighbours of a given site can be treated globally as an external bath when their distance from the site becomes large, and the spatial fluctuations of the local field become negligible.

These ideas can be directly extended to quantum many-body systems [6], where the electron on the fixed site couples itself with all other electrons through a 'Weiss field', that in this case depends on energy (frequency) and it is not a scalar quantity. In other words, the DMFT self-consistency equation has not an analytic form, but rather needs to be solved numerically, through an iterative procedure, that ends when the solution converges. The main DMFT problem is the resolution of the impurity solver, which treats the problem of the single-site coupled with the bath. For the sake of simplicity, we will consider a single-band Hubbard model (1.3), with no symmetry breaking, in order to deal with the translation-invariant paramagnetic phase. The mean-field description associates to this Hamiltonian a single-site effective dynamics, which is conveniently described in terms of an imaginary-time action for the electronic degrees of freedom $(c_{l,\sigma}, c_{l,\sigma}^{\dagger})$ at that site:

$$(1.17) \quad S_{eff} = -\int_0^\beta d\tau \int_0^\beta d\tau' \sum_\sigma c_{l,\sigma}^{\dagger}(\tau) \mathcal{G}_0^{-1}(\tau - \tau') c_{l,\sigma}(\tau') + U \int_0^\beta d\tau n_{l,\uparrow}(\tau) n_{l,\downarrow}(\tau)$$

where $\mathcal{G}_0(\tau - \tau')$ plays the role of the Weiss effective field above. Its physical meaning is that of an effective amplitude for an electron to be created on the isolated site at time τ (coming from the external bath) and being destroyed at time τ' (going back to the bath). The main difference with the classical case is that this generalized Weiss function is a function of time instead of a scalar quantity, feature necessary to take into account local quantum fluctuations. $\mathcal{G}_0(\tau - \tau')$ plays the role of a bare Green's function for the local effective action S_{eff}, but it should not be confused with the non-interacting local Green's function of the original lattice model.

A closed set of equations is obtained connecting (1.17) with the expression relating $\mathcal{G}_0$ to local quantities computable from S_{eff} itself, in complete analogy with (1.15).

This self-consistency condition reads:

$$(1.18) \qquad \mathcal{G}_0^{-1}(i\omega_n) = i\omega_n + \mu + G^{-1}(i\omega_n) - R[G(i\omega_n)]$$

where $G(i\omega_n)$ denotes the on-site interacting Matsubara Green's function [9], that can be calculated from the effective action S_{eff}, and $R(G)$ is the reciprocal function of the Hilbert transform of the density of states corresponding to the lattice. In equilibrium, the Matsubara Green's function depends on the relative imaginary time, due to its time-translational invariance:

$$(1.19) \qquad G^M(\tau, \tau') = G^M(\tau - \tau')$$

and its Fourier transform reads:

$$(1.20) \qquad G^M(i\omega_n) = \int_0^\beta d\tau e^{i\omega_n \tau} G^M(\tau) = -\left\langle \mathcal{T} c(\tau) c^\dagger(\tau') \right\rangle_{S_{eff}}$$

where $\omega_n = \frac{(2n+1)\pi}{\beta}$ are the discrete Matsubara frequencies. Note that they contain the inverse temperature β, which gives the temperature dependence of the Green's function. Explicitly, given the non-interacting density of states $D(\epsilon)$:

$$(1.21) \qquad D(\epsilon) = \sum_{\mathbf{k}} \delta(\epsilon - \epsilon_{\mathbf{k}}) \qquad \epsilon_{\mathbf{k}} = \sum_{ij} t_{ij} e^{i\mathbf{k}\cdot(\mathbf{R}_i - \mathbf{R}_j)}$$

the Hilbert transform $\tilde{D}(\xi)$ and its reciprocal function R are defined as:

$$(1.22) \qquad \tilde{D}(\xi) = \int_{-\infty}^{+\infty} d\epsilon \frac{D(\epsilon)}{\xi - \epsilon} \qquad R[\tilde{D}(\xi)] = \xi$$

Since $G(i\omega_n)$ can be computed as a functional of $\mathcal{G}_0$ using the impurity action S_{eff}, the equations (1.17), (1.18) and (1.20) form a closed system of functional equations for the local Green's function $G(i\omega_n)$ and the Weiss function $\mathcal{G}_0(i\omega_n)$. Those equations can be solved through an iterative procedure [6].

The cycle starts with some guess for $\mathcal{G}_0$, after that one can compute G as a functional of $\mathcal{G}_0$ using (1.20), update G and find the updated Weiss field from (1.18), iterating the steps until convergence is reached. It is instructive to check these equations in two simple limits:

(i) In the non-interacting limit $U = 0$, from (1.17) one can obtain $G(i\omega_n) = \mathcal{G}_0(i\omega_n)$ and hence, from (1.18), $G(i\omega_n)$ reduces to the free local Green's function.

(ii) In the atomic limit $t_{ij} = 0$, the lattice is only a collection of disconnected sites and $D(\epsilon)$ becomes a δ function. Then (1.18) implies $\mathcal{G}_0^{-1}(i\omega_n) = i\omega_n + \mu$ and the effective action S_{eff} becomes essentially local in time.

Solving the coupled equations above not only provides the local quantities but also allows us to reconstruct all the **k**-dependent correlation functions of the original lattice Hubbard model. For example, the Fourier transform of the one-particle Green's function $G_{ij}(\tau - \tau')$ reads:

$$(1.23) \qquad G(\mathbf{k}, i\omega_n) = \frac{1}{i\omega_n + \mu - \epsilon_{\mathbf{k}} - \Sigma(i\omega_n)}$$

where the self-energy can be computed from the solution of the effective on-site problem (Dyson equation) as:

$$(1.24) \qquad \Sigma(i\omega_n) = \mathcal{G}_0^{-1}(i\omega_n) - G^{-1}(i\omega_n)$$

In this approach, $\Sigma(i\omega)$ is completely **k**-independent, in other words it is purely local in space $\Sigma_{ij}(i\omega_n) = \delta_{ij}\Sigma(i\omega_n)$. From this expression, one sees that the self-consistency condition (1.18) relating G and $\mathcal{G}_0$, ensures that the local component of the Green's function, given by $G_{ii}(i\omega_n) = \sum_{\mathbf{k}} G(\mathbf{k}, i\omega_n)$, coincides with the Green's function $G(i\omega_n)$ calculated from the effective action S_{eff}.

2.2. Iterated perturbation theory.

Over the years, a lot of impurity solver methods were developed in the context of correlated materials to approach the impurity problem and solve the DMFT cycle [6][12]. Basically, there are two main classes of impurity solvers: the diagrammatic approaches and the Hamiltonian-based approaches. The former treat the impurity action in a perturbative way, using diagrammatic techniques, while the latter solve the time-dependent Hamiltonian directly. In our work, we use the Iterated Perturbation Theory (IPT), an approach that belongs to the first category and is used to investigate the half-filled Hubbard model and the physics of the Mott transition. This method relies on the weak-coupling studies of the half-filled single-impurity model, where it was shown that the second-order perturbation theory in U is a very good approximation. In other words, one can expand in series the self-energy Σ and truncate its diagrammatic expansion at the second order in U. In particular, this method succeeds in capturing the Mott transition in the paramagnetic solution, at half filling. Explicitly, one makes use of the following approximate form for the self-energy:

$$(1.25) \qquad \Sigma(i\omega_n) \simeq \frac{U}{2} + U^2 \int_0^{\beta} d\tau e^{i\omega_n \tau} \mathcal{G}_0^3(\tau)$$

in which the shift $\mathcal{G}_0^{-1}(i\omega_n) = \mathcal{G}_0^{-1} - \frac{U}{2}$ has been made to enforce the particle-hole symmetry. A self-consistent solution $(G, \mathcal{G}_0)$ is then found by going through the

iteration described above. Equation (1.25) represents the heart of the iterated perturbation theory (IPT) approximation. This method can be implemented by using Fourier transforms on the Matsubara axis (imaginary time axis).

Considering the atomic limit, for which $\mathcal{G}_0^{-1} \simeq i\omega_n$, the exact Green's function and self-energy read:

$$(1.26) \qquad G(i\omega_n) = \frac{1}{2}\left[\frac{1}{i\omega_n + U/2} + \frac{1}{i\omega_n - U/2}\right] \qquad \Sigma(i\omega_n) = \frac{U}{2} + U^2\mathcal{G}_0(i\omega_n)/4$$

Hence, (1.25) correctly reproduces this limit. For this reason, the IPT method is actually not limited to moderate couplings (at half-filling), but it also correctly reproduces the exact strong-coupling limit. Actually, it provides an interpolation scheme between weak- and strong-coupling limits, both captured exactly.

The fact that a weak coupling expansion works in the strong coupling case is a coincidence. The reason behind this success is that the Anderson impurity model is analytic in U regardless of the nature of the bath, so that it can be treated perturbatively. The value of the IPT approximation relies largely on its simplicity: it is much easier to implement than the full numerical solution of the model, and allows a fast scan of parameter space. Due to the possibility of interpolation between weak and strong coupling at half-filling, IPT correctly captures the physics of the Mott transition.

2.3. Keldysh version of IPT.

So far, calculations with IPT at finite temperature T have been done using the Matsubara frequency dependent Green's function, defined on the imaginary axis. Actually, iterative perturbation theory (at half-filling) can be formulated in real frequency space using the Keldysh formalism [13], an out-of-equilibrium extension of the equilibrium Green's function algebra.

In the Keldysh formalism, we introduce the contour $\mathcal{C}$, that starts from $-\infty$, passes through the points t_1 and t_2, arrives at $+\infty$ and then returns back to $-\infty$, as illustrated in Figure 1.3 [14]. Ordering along the contour $\mathcal{C}$ means that the points on the return branch of this contour correspond to later times with respect to the points on the original direct branch, and of any two points on the return path the later one is that which is closer to $-\infty$.

The introduction of this formalism is necessary due to the out-of-equilibrium breaking of the Gell-Mann and Low theorem. This theorem allows in fact to relate the $t = -\infty$ vacuum state of a given system to the $t = +\infty$ one, if one starts with a
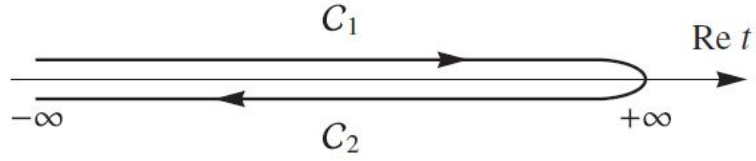
FIGURE 1.3. The Keldysh contour $\mathcal{C}$ along the real time axis, with the two branches $\mathcal{C}_1$ and $\mathcal{C}_2$. The arrows indicate the contour-ordering.

non-interacting system and adiabatically switches on the interactions. In equilibrium, this theorem is very useful, because it allows one to express Green's functions as expectation values of interaction fields in the non-interacting vacuum. However, when the system is driven out-of-equilibrium by a perturbation switched on non-adiabatically, the initial and final states no longer coincide. For this reason, one has to use the same state (at $t = -\infty$) as initial and final state of the dynamics, as illustrated in Figure 1.3.

The Keldysh formalism is very useful to compute results for the half-filled Hubbard model. Its equilibrium version is a generalization of the standard $T = 0$ diagram technique to finite temperatures, and it uses four different Green's functions (G^{11}, G^{22}, G^{12}, G^{21}), i.e. many-body objects that describe the propagation of single particles, which are defined as follows:

(1.27)
$$iG^{11}(x_1, t_1; x_2, t_2) = \left\langle \tilde{\mathcal{T}}_{\mathcal{C}} \psi(x_1, t_1) \psi^\dagger(x_2, t_2) \right\rangle =$$
$$= \theta(t_2 - t_1) \left\langle \psi^\dagger(x_1, t_1) \psi(x_2, t_2) \right\rangle - \theta(t_1 - t_2) \left\langle \psi(x_2, t_2) \psi^\dagger(x_1, t_1) \right\rangle$$

(1.28)
$$iG^{22}(x_1, t_1; x_2, t_2) = \left\langle \mathcal{T}_{\mathcal{C}} \psi(x_1, t_1) \psi^\dagger(x_2, t_2) \right\rangle$$
$$= \theta(t_1 - t_2) \left\langle \psi(x_1, t_1) \psi^\dagger(x_2, t_2) \right\rangle - \theta(t_2 - t_1) \left\langle \psi^\dagger(x_2, t_2) \psi(x_1, t_1) \right\rangle$$

(1.29)
$$iG^{12}(x_1, t_1; x_2, t_2) = \left\langle \psi(x_1, t_1) \psi^\dagger(x_2, t_2) \right\rangle$$

(1.30)
$$iG^{21}(x_1, t_1; x_2, t_2) = \left\langle \psi^\dagger(x_2, t_2) \psi(x_1, t_1) \right\rangle$$

where $\mathcal{T}_{\mathcal{C}}$ indicates ordering along the contour $\mathcal{C}$.

Moreover, one can observe that:

(1.31)
$$G^{22} + G^{11} = G^{12} + G^{21}$$

According to (1.31), only three of four Green's functions are independent. Besides the causal Green's functions defined above, we introduce two others Green's functions, from which many physical quantities are more easily extracted. These are the advanced and retarded Green's functions, which by construction are anti-causal and causal, respectively. In fact, the advanced Green's function is defined as:

$$
iG^A(x_1, t_1; x_2, t_2) = -\theta(t_2 - t_1) \left\langle \psi(x_1, t_1)\psi^\dagger(x_2, t_2) + \psi^\dagger(x_1, t_1)\psi(x_2, t_2) \right\rangle
$$
$$
(1.32) \qquad\qquad\qquad = G^{22} - G^{12} = G^{21} - G^{11}
$$

From the advanced Green's function, one can immediately calculate the retarded Green's function, defined as:

$$
(1.33) \qquad\qquad G^R = (G^A)^\dagger
$$

So far, we have expressed the Green's function in the time domain. However, it is often convenient to represent them in the energy domain. When the system is at equilibrium, the Green's functions are time-translational invariant, depending only on the time difference $t_1 - t_2$. Thus, the Fourier transforms of equations from (1.27) to (1.30) are:

$$
(1.34) \qquad\qquad G^{(0)21}(\omega, k) = 2\pi i n_k \delta(\omega - \epsilon_k + \mu)
$$

$$
(1.35) \qquad\qquad G^{(0)12}(\omega, k) = -2\pi i (1 - n_k)\delta(\omega - \epsilon_k + \mu)
$$

$$
(1.36) \qquad\qquad G^{(0)22}(\omega, k) = \frac{1 - n_k}{\omega - \epsilon_k + \mu + i0^+} + \frac{n_k}{\omega - \epsilon_k + \mu - i0^+}
$$

$$
(1.37) \qquad\qquad G^{(0)11}(\omega, k) = -\left(G^{(0)22}(\omega, k) \right)^*
$$

where n_k is the Fermi factor. Similarly, there are four contributions to the self-energy $\Sigma^{11}, \Sigma^{22}, \Sigma^{21}, \Sigma^{12}$, again related by:

$$
(1.38) \qquad\qquad \Sigma^{11} + \Sigma^{22} = -\Sigma^{21} - \Sigma^{12}
$$

and the advanced self-energy is defined as:

$$
(1.39) \qquad\qquad \Sigma^A = \Sigma^{22} + \Sigma^{12}
$$

The iterative perturbation theory is then performed by iterating the following steps:

(i) We start with a guess for the advanced Green's function $G^A(\omega)$. Then $G_0^A(\omega)$ is determined by:

$$(G_0^A)^{-1}(\omega) = \omega - i\eta - t^2 G^A(\omega) \tag{1.40}$$

Now, there are many physical properties that can be extrapolated from the Green's functions. The imaginary part of the advanced (or retarded) Green's function provides the spectral weight $A(\omega)$ of the system:

$$A(\omega) = \frac{1}{\pi} Im\left[G_0^A(\omega)\right] \tag{1.41}$$

that represents the density of many-body excitations at energy ω.

We introduce $A(t)$ and $\tilde{A}(t)$ as Fourier transform of $A(\omega)$ and $\tilde{A}(\omega) = A(\omega)n_k(\omega)$:

$$A(t) = \int_{-\infty}^{+\infty} \frac{d\omega}{2\pi} A(\omega)e^{-i\omega t} \tag{1.42}$$

$$\tilde{A}(t) = \int_{-\infty}^{+\infty} \frac{d\omega}{2\pi} \tilde{A}(\omega)e^{-i\omega t} \tag{1.43}$$

Using $G^{\sigma\sigma} = \int d\kappa G^{(0)\sigma\sigma}(\omega, \epsilon_k)A(\epsilon_k)$, we can express all four Green's functions in terms of $A(t)$ and $\tilde{A}(t)$:

$$G_0^{22}(t) = \left[\theta(t)\left[A(t) - \tilde{A}(t)\right] + \theta(-t)\tilde{A}(t)\right] \tag{1.44}$$

$$G_0^{11}(t) = \left[-G_0^{22}(-t)\right]^* \tag{1.45}$$

$$G_0^{21}(t) = 2\pi i \tilde{A}(t) \tag{1.46}$$

$$G_0^{12}(t) = -2\pi i \left[A(t) - \tilde{A}(t)\right] \tag{1.47}$$

(ii) These Green's functions are necessary to evaluate the second order self-energy diagrams:

$$\Sigma^{22}(t) = U^2 \left[G_0^{22}(t)\right]^2 G_0^{22}(-t) \tag{1.48}$$

$$\Sigma^{12}(t) = -U^2 \left[G_0^{12}(t)\right]^2 G_0^{21}(-t) \tag{1.49}$$

(iii) Now, one can update the advanced functions:

$$G_0^A(t) = G_0^{22}(t) - G_0^{12}(t) \tag{1.50}$$

$$\Sigma^A(t) = \Sigma^{22}(t) + \Sigma^{12}(t) \tag{1.51}$$

(iv) Finally, one can compute the new Green's function G^A:

(1.52)
$$\left[G^A(\omega)\right]^{-1} = \left[G_0^A(\omega)\right]^{-1} - \Sigma^A(\omega)$$

and returning to (1.40) to close the iteration loop. This process is iterated until convergence is achieved.

In the end, we discuss briefly the difference between the Matsubara and the Keldysh formalism. The choice one has to make is about how the time variable are treated in the complex plane. Matsubara Green's functions are defined on the imaginary time axis, and they can only describe equilibrium properties, relying on the connection between imaginary time and temperature. Instead, the Keldysh formalism is the main way to approach non-equilibrium states [13]. This method can be successfully used to study open non-equilibrium systems, which are coupled to external reservoirs that provide energy dissipation. However, the Keldysh method can also be reduced to study equilibrium situations; for this reason, those can be approached both with Matsubara and Keldysh formalism, as we will see in the next section. However, the physical equilibrium quantities will be defined respectively on the imaginary and on the real axis, and therefore their physical interpretation will be very different.

3. Equilibrium DMFT: results

3.1. Mott transition.

According to the conventional band theory, Mott insulators are materials that should have metallic behaviour, but actually they are insulators. This discrepancy is caused by the electron-electron interactions, which are treated with the independent electrons approximation in the band theory. We study the phase diagram of these materials with the IPT method, by modelling the system within the Hubbard Hamiltonian (1.3). The dynamics of the system is dominated by the ratio U/t between the on-site Coulomb repulsion U and the hopping t. In fact, if $t \gg U$, one expects the existence of a metallic phase, while if $U \gg t$ the electrons will tend to localize on their site, causing the Mott transition and the generation of the Mott insulating phase. For intermediate values of the ratio U/t, we deal with a strongly correlated material, and its behaviour has to be investigated through numerical methods, necessary all above for the approach to the Mott transition. Obviously, the exact transition point is the most difficult to approach due to its first-order character.

We investigate the phase diagram of these materials getting close to the transition

point increasing U gradually, using the self-energy Σ computed for the previous point as a guess to approach the subsequent one, in order to stabilise the solution at the transition. Approaching the transition point, we attend a phenomenon called 'critical slowing down'; the convergence time of the numerical solution becomes the higher the U gets closer to to U_{crit}, at which the transition suddenly occurs.

3.2. Double occupation and quasi-particle weight.

In this section, we study the half-filled Hubbard model, both in the limits of high and low U/t ratios, as well as for intermediate values, by using the equilibrium DMFT, with the IPT method as impurity solver. As introduced in the previous sections, a very important limit for any lattice model is the limit of infinite coordination number, $z \to \infty$. In fact, in this limit DMFT becomes exact, the self energies are exactly local in space, and the Hubbard model can be mapped into a single-impurity problem with self-consistency condition.

In order to investigate the phase diagram of the Hubbard model, and in particular the Mott transition, we introduce the Bethe lattice, visible in Figure 1.4. The Bethe
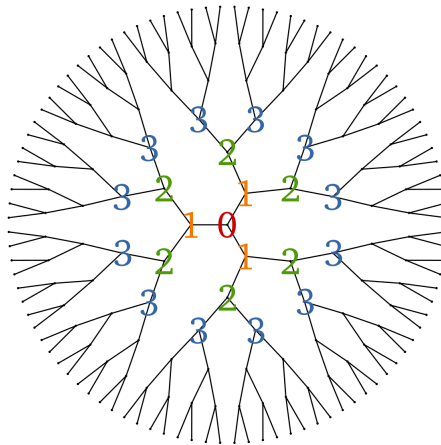

FIGURE 1.4. Example of Bethe lattice with coordination number $z = 3$.

lattice is defined as an infinite coordination number Cayley tree, where any two points are connected by a single line and each vertex has the same coordination number z. It plays an important role in condensed-matter physics, because some problems can be solved exactly when defined on a Bethe lattice [15]. Moreover, its self-similar topological structure implies very useful recurrence relations, that simplify the analysis of some problems.

We consider tight-binding Hamiltonian with nearest-neighbour hopping t, in the limit $z \to \infty$. The resulting semi-elliptical density of states reads:

$$(1.53) \qquad \rho(\epsilon) = \frac{4\sqrt{1 - (2\epsilon/W)^2}}{\pi W}$$

where W is the bandwidth. On this limit, it is well-established [15] that the Mott transition occurs at a particular value of U, called U_{crit}, which is about three times the half-bandwidth. For this reason, we will expect the Mott transition occurs at $U_{crit} \simeq 3$ (all values of U are expressed in units of half-bandwidth $W/2$).

We compute several physical observables, in order to describe and better understand the Mott transition from different points of view. It is very important to underline that during the DMFT resolution process the density of occupation has to be conserved, and the system must remain at the half-filling (density of electrons= 0.5, one electron per site). This can be understood just by considering the impurity solver used; in fact the IPT method interpolates from weak to strong coupling only at the half-filling, which therefore becomes a necessary condition. We first analyse the double occupancy $\langle D \rangle$, which is defined as the probability to have two electrons at the same time on the same site. In the non-interacting limit $U/t = 0$, the value
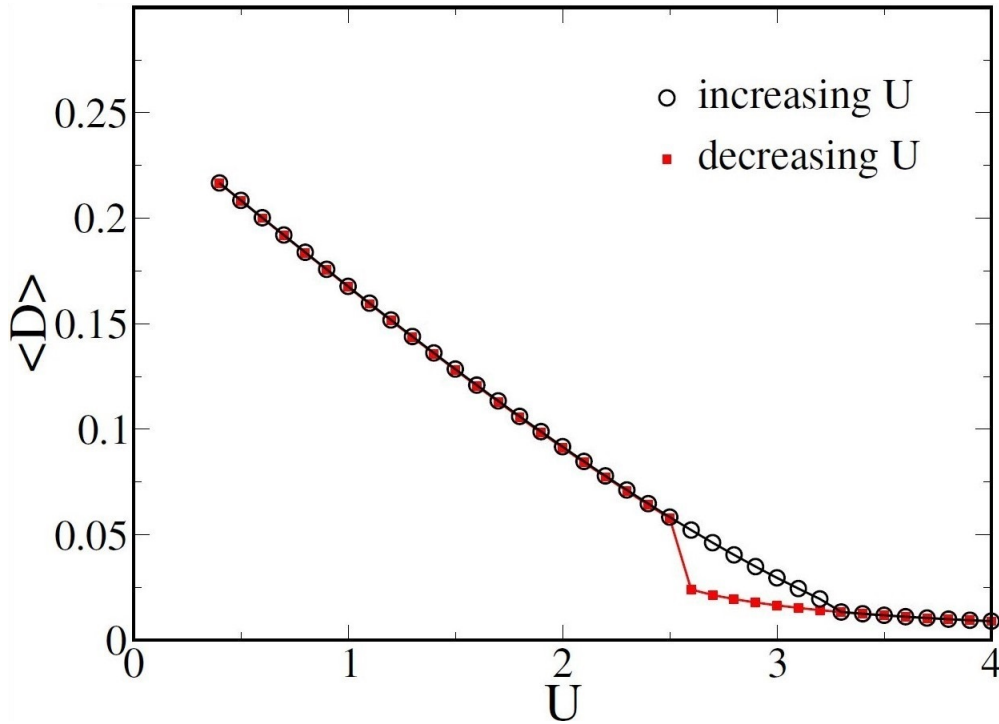

FIGURE 1.5. Double occupancy $\langle D \rangle$ vs interaction strength U, both for increasing and decreasing U. The Mott transition occurs at $U \sim 3$.

of the double occupancy is 0.25, simply because there are four possibilities for the single site: no electron on the site, one electron with spin up/down or two electrons (with spin up and down). Of course, the Pauli principle of exclusion prevents other possibilities.

To better underline the first-order character of the Mott transition, we first increase the ratio U/t from lower values approaching the transition point 'from left', then we repeat the calculation coming 'from right', by decreasing U/t. The double occupancy vs the interaction U, both at increasing and decreasing value of U, is illustrated in Figure 1.5. Increasing the interaction U from low values, the probability of finding two electrons on the same site at the same time starts to decrease, because the presence of the interaction U reduces the wavefunction overlap between neighbour sites, localizing the system. When U approaches the value of U_{crit}, at which the
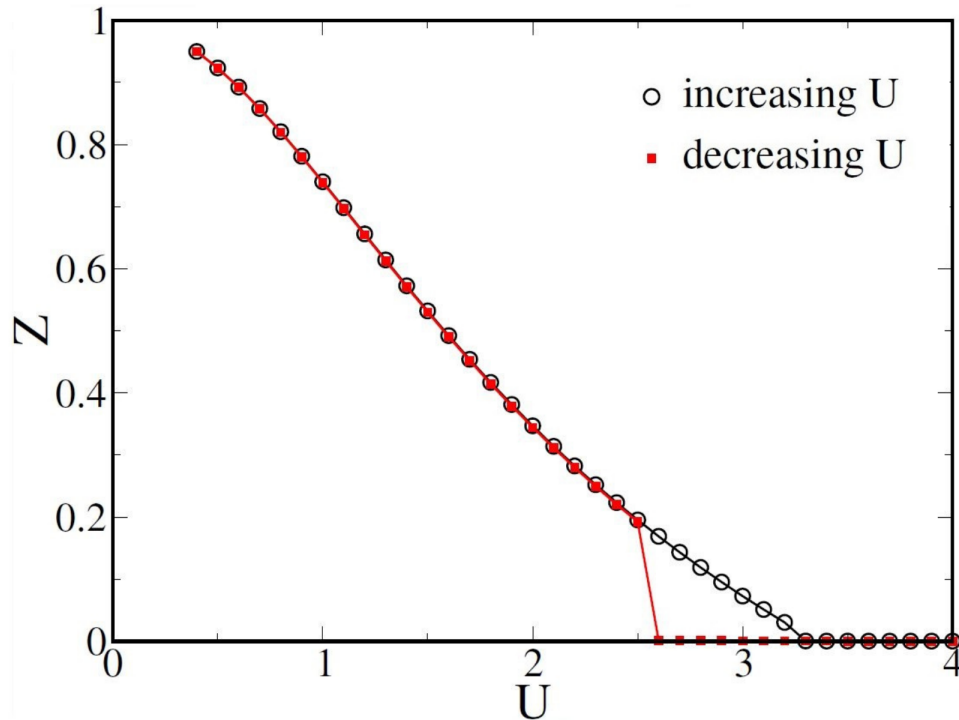

FIGURE 1.6. Quasi-particle weight Z vs interaction strength U, both for increasing and decreasing U. At the Mott transition ($U \sim 3$), the quasi-particle weight suddenly vanishes, and the system becomes insulating.

Mott transition occurs, the double occupation presents a discontinuity; continuing to rise U, the system enters completely in the insulating phase, and the double occupancy tends to zero (actually the double occupancy does not vanish completely

at $T \neq 0$, because of quantum fluctuation). Similarly, we start from high values of U and slowly reduce it, finding a similar behaviour, with a more visible discontinuity placed at lower U. The final picture represents a hysteresis cycle, typical of first-order phase transitions. As we expected, the phase transition occurs near $U_{crit} \sim 3$, as visible in Figure 1.5. Considering the energy of the system, the two discontinuities represent the edges of meta-stable states, while the proper transition is situated between them.

We then compute the quasi-particle weight Z, defined as:

$$(1.54) \qquad\qquad Z = \left(1 - \frac{\partial \Sigma(\omega)}{\partial \omega}\right)^{-1} = \frac{m}{m^*}$$

where $\Sigma(\omega)$ is the self-energy and m^* the effective mass. Ranging from 0 to 1, Z describes the similarity between the electronic excitations and the naked particles. When $Z = 1$, from (1.54) the effective mass coincides with the bare electron mass (the quasi-particles are simply particles), and the system is completely non-interacting ($\Sigma(\omega) = 0$). Viceversa, if $Z = 0$ the system is completely correlated, becoming an insulator (its effective mass diverges, because no electronic transport is allowed). Looking at Figure 1.6, several similarities with Figure 1.5 can be found. In fact, once again the two curves obtained increasing and decreasing U show a discontinuity, typical of the first-order transitions, which occurs at $U_{crit} \sim 3$.

3.3. Green's function and self-energy evolution.

In this section, we focus on the evolution with U of the Green's function and self-energy of the system, looking at their behaviour in the different phases. Imaginary time formalism is very useful when we perform perturbation expansions, like in the IPT method. For this reason, we investigate the behaviour of the system using the Matsubara Green's function $G^M(\tau, \tau')$, where time and frequency are imaginary. During IPT calculations, one can increase the precision of the Fourier series expansion by using a bigger set of Matsubara frequencies, which allows us to resolve better the discontinuous Mott transition.

We look at the evolution of the Green's function and the self-energy of our system. Generally speaking, the Green's function is related to the spectral function $A(\omega)$ through the following relation:

$$(1.55) \qquad\qquad A(\omega) = -\frac{1}{\pi} Im G^R(\omega)$$

where $A(\omega)$ represents the density of single-particle excitations at energy ω of the many-body state and G^R is the retarded component of the Green's function. In
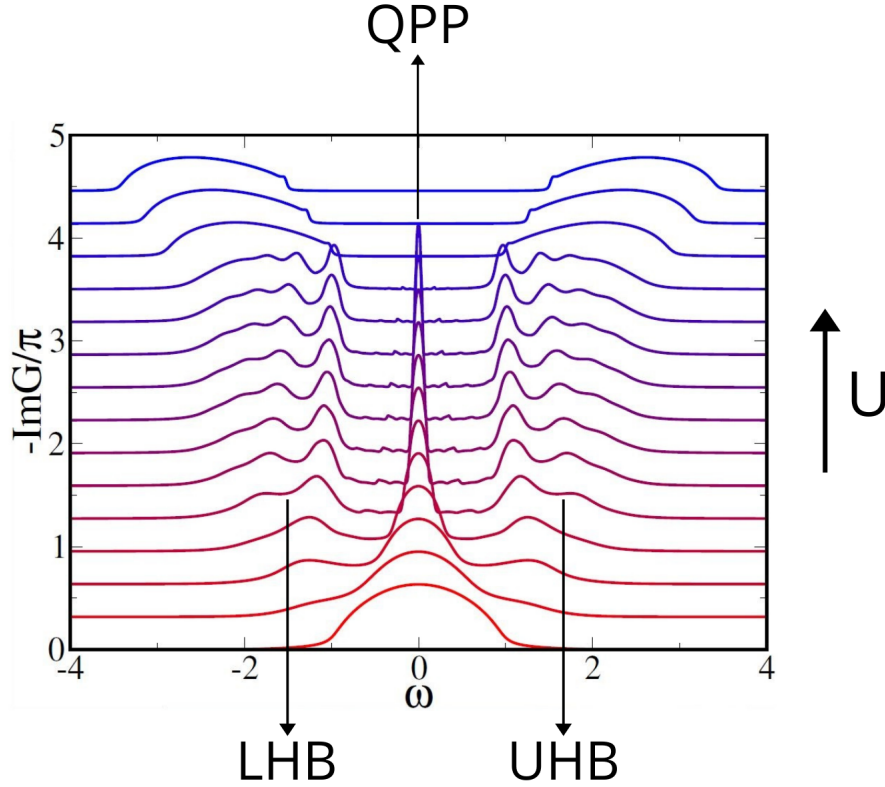
FIGURE 1.7. Spectral function $A(\omega) = -\frac{1}{\pi}G$, defined on the real axis. From below upwards the interaction U is increased. From the initial metallic distribution, the quasi-particle peak (QPP) is then created with the upper and lower Hubbard bands (UHB) and (LHB), until the Mott transition occurs and the QPP vanishes.

other words, $A(\omega)$ it represents how the electronic levels are displaced in energy. The spectral function distinguishes between metal and insulator, whose discriminant is to have/do not have free electronic states near the Fermi level. In the idealized case of free non-interacting electrons, the spectral function is a δ function: an excitation with energy ω can therefore only happen by adding an electron to the same state $\mathbf{k}$ given by $\epsilon_{\mathbf{k}} = \omega$. Generally, due to interactions the spectral function differs from a δ function, acquiring a more broadened profile (still peaked). We plot the imaginary part of the Green's function and the self-energy, both on the imaginary axis (Matsubara) and on the real axis (using the Keldysh formalism, with the retarded component of the Green's function). To explain the difference, one has to consider that the Green's functions are defined on the complex plane, and can be seen from different points of view, each having different behaviour and physical interpretation.

Due to the fact that the imaginary axis intersects the real axis at the origin, the behaviour of the Green's function at the origin (looking on Matsubara axis) has to be the same of the real axis one (it follows from analytical continuation). The best way to visualize this, is thinking to move along the imaginary axis, from which the origin is the only point on the real axis one can cross.

First of all, we plot the evolution with U of the spectral function $A(\omega)$ on the real axis, visible in Figure 1.7. When $U = 0$, the spectral function presents spectral weight at the Fermi level (metallic phase). As long as U is increased, the spectral weight at the Fermi level shrinks, creating a quasi-particle peak (QPP) centred at the Fermi level, and the gap starts to open at the Fermi level. Moreover, the spectral weight move to higher energies and the upper (UHB) and lower (LHB) Hubbard bands arise, giving birth to a three-feature spectral function typical of correlated materials. In the end, when U becomes greater than U_{crit}, the Mott transition occurs, and the QPP disappears, leaving the spectral weight outside the gap.

We then plot the imaginary part of the Green's function on the Matsubara axis, as visible in Figure 1.8. It looks completely different with respect to Figure 1.7, even if the two pictures have the same physical meaning. As already said, the Matsubara axis plot reproduces the behaviour of the Green's function on the real axis only at the origin, so that its physical meaning is not obvious. To interpret it, one has to imagine to move along the imaginary axis, getting closer and further to the real axis. Looking at Figure 1.8, at high $i\omega_n$ we find quite the same behaviour for all values of U: the resulting $\mathrm{Im}G$ is low because we are very far from the real axis. Instead, getting closer to the real axis (reducing $i\omega_n$) allows to resolve the spectral features, generating different behaviours according to the strength of the interaction U.

In the case of a correlated metal, where the spectral function presents a quasi-particle peak at the Fermi level, one expects to see it from the imaginary axis the better the wider is the peak; for this reason as long as U is increased (and the peak shrinks) the curve becomes steeper, because one need to get always closer to the real axis to solve the quasi-particle peak.

The behaviour at the origin is indeed interesting. As already said, due to the analyticity of the Green's function, the continuation of the Matsubara axis at the origin must match up the value on the real axis (actually the real value can be reached only at $T = 0$, when the Matsubara frequencies are a continuum). Moreover, the Luttinger-Ward theorem reads that the spectral weight at the Fermi level is conserved with the interaction U at $T = 0$, until U is lesser than U_{crit}. Therefore, as long
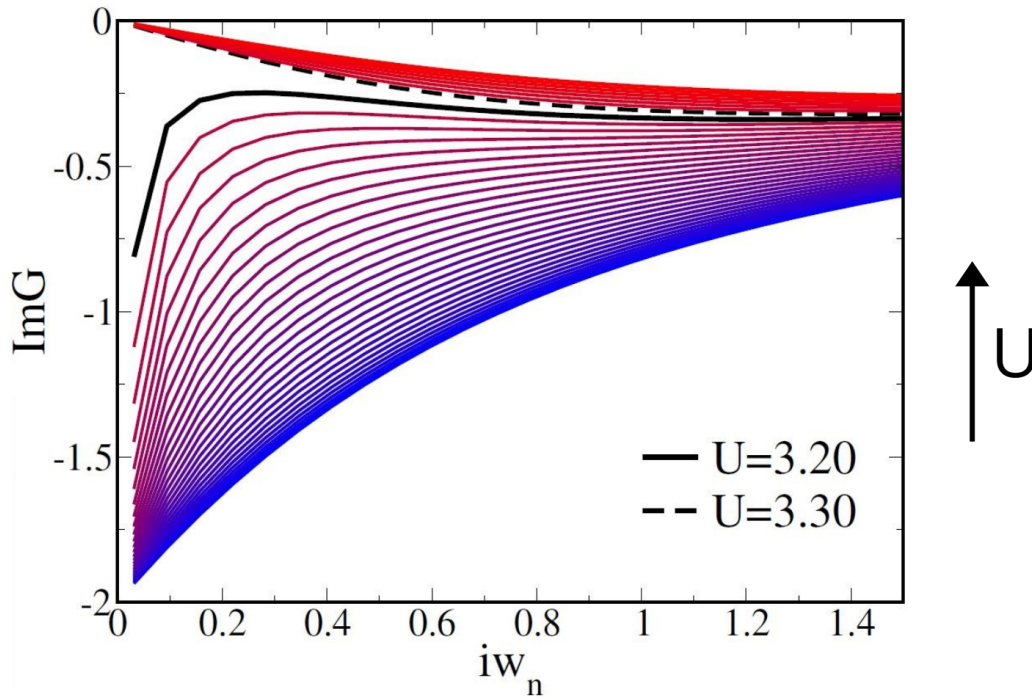
FIGURE 1.8. Imaginary part of the Green's function G defined on the Matsubara axis $i\omega_n$. The interaction U is increased from below upwards. The transition occurs between $U = 3.20$ and $U = 3.30$.

as U is increased, the spectral function goes to the same value in zero (behaviour defined as *spectral pinning*), the sharper the higher is the interaction. As long as U is increased, the quasi-particle peak becomes more and more sharp, and the slope of the curve is steeper, because it is more difficult to see the quasi-particle peak from the Matsubara axis. In the end, when U crosses U_{crit}, the imaginary part of the Green's function suddenly goes to zero, because the quasi-particle peak has totally disappeared. At that moment, the material starts to be an insulator.

To continue our analysis, we plot the self-energy of the system, both on the real and on the Matsubara axis. In a correlated system, the self-energy Σ describes the effects of the interaction on the propagation of single particles. Its behaviour on the real axis is strongly related to the Green's function one, as one can see from Figure 1.9. Looking at the self-energy of the system, in the non-interacting limit $U = 0$ the quasi-particles are actually particles, and the self-energy is flat, being proportional to U, as in (1.25). As long as U is increased, the system starts to be deeply different from the non-interacting one, becoming a strong correlated metal (with a many-body structure and a single wave-function). The system self-energy
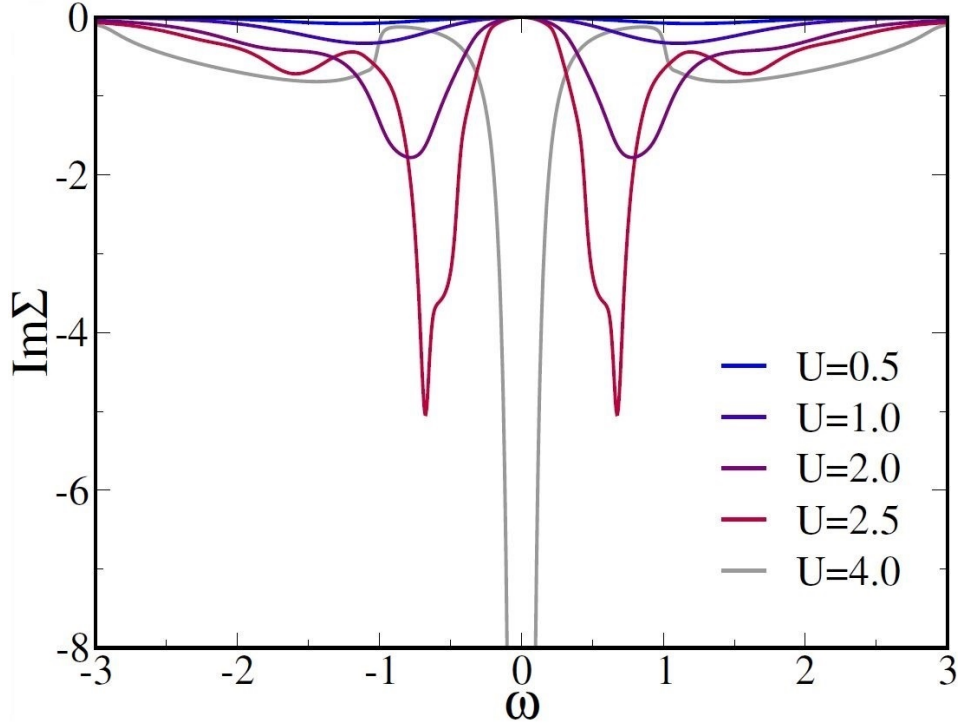
FIGURE 1.9. Evolution with U of the imaginary part of the self-energy Σ, on the real axis. In the correlated phase, ImΣ vanishes at $\omega = 0$, regardless of U. At the Mott transition, ImΣ develops a pole at the Fermi level.

Σ develops its proper structure, but still has to vanish at the Fermi level ($\omega = 0$), due to the Luttinger-Ward theorem (the system can not change in zero at the Fermi level, so the self-energy, which would be responsible for the change, has to vanish). Looking more closely to the Fermi level, the behaviour of ImΣ is parabolic, whose curvature is the quasi-particle weight Z, which represents the number of electronic states in quasi-particle excitations. In the end, the most important feature of Figure 1.9 is that at the Mott transition ImΣ develops a pole at the Fermi level.

In order to understand the striking consequences of this fact, let us consider the Green's function G:

$$(1.56) \qquad\qquad G = \frac{1}{\omega - H(k) - \Sigma}$$

Substituting $\Sigma = \Sigma_R + i\Sigma_I$ and rationalising, one obtains:

$$(1.57) \qquad G = \frac{\omega - H(k) - \Sigma_R}{(\omega - H(k) - \Sigma_R)^2 + \Sigma_I^2} - i\frac{\Sigma_I}{(\omega - H(k) - \Sigma_R)^2 + \Sigma_I^2}$$

Taking $\Sigma_I = \Gamma$, the negative imaginary part of G reads:

$$(1.58) \qquad -ImG = \frac{\Gamma}{(\omega - H(k) - \Sigma_R)^2 + \Gamma^2}$$

which is a Γ-width Lorentzian centred in:

$$(1.59) \qquad \omega - H(k) - \Sigma_R = 0$$

which defines the poles equation. When at the Mott transition $Im\Sigma$ develops a pole, due to the Kramers-Kronig relations also $Re\Sigma$ is discontinuous. Considering

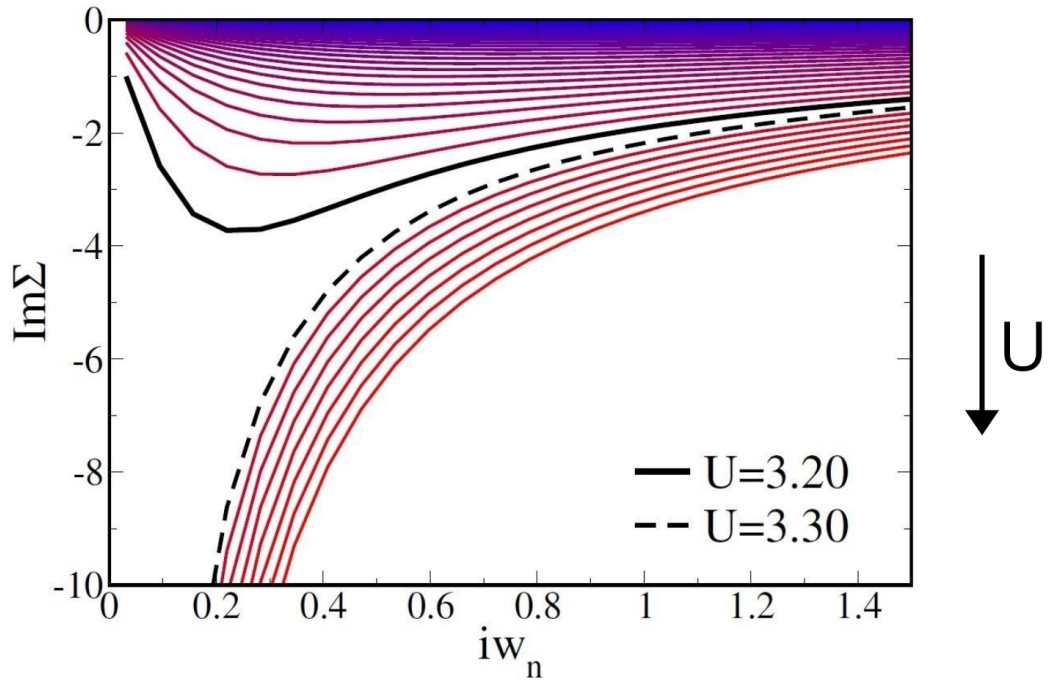FIGURE 1.10. $Im\Sigma$ on the Matsubara axis. U is increased form the top down. In the correlated phase, $Im\Sigma$ vanishes regardless of U, while at the Mott transition it develops a pole at the Fermi level. Both these features are visible also from the imaginary axis (by analytic continuation).

the poles equation (1.59), no solutions can exist near the Σ_R discontinuity, because $H(k)$ has a discrete spectrum, with bounded energies.

Therefore, the net effect of $Re\Sigma$ is to eliminate the poles of G in a finite range of frequencies near the Fermi level, by preventing G to have finite spectral weight in that range, and opening an insulating gap, in a totally many-body way. Of course, others finite energy solutions exist (at higher energies), and form the Hubbard bands.

When the particle-hole symmetry holds, Σ on the real axis diverges at μ. At half-filling, $\mu = 0$ and the divergence of ImΣ can be seen even on the Matsubara axis, as in Figure 1.10. Looking more closely at the Fermi level, one can observe that ImΣ goes linearly to zero (even in a strongly-correlated metal) because of the spectral pinning described above, with slope equal to the quasi-particle weight Z. In the non-interacting case, $Z = 1$ and all electronic states contribute to the quasi-particle peak, while in the correlated material, when $Z < 1$, only a fraction of particles contributes to the quasi-particle peak, until $Z = 0$ is reached, the Mott transition occurs, no states contribute and the peak disappears.

CHAPTER 2

Non-equilibrium dynamics: the NEQ-DMFT

In this chapter, we firstly introduce the non-equilibrium dynamical mean field theory (NEQ-DMFT), a direct out-of-equilibrium extension of the DMFT. This method allows to investigate the non-equilibrium dynamics of correlated systems, through a time-step procedure. We discuss the effects of a DC field on a bidimensional Hubbard model, according to its degree of coherence. We then provide the necessary formalism to couple the system with an external electromagnetic field (that drives the system out-of-equilibrium) and an external thermal bath, responsible for the energy dissipation. In the end, we observe that the coupling with an external heat bath provides to the system a thermalization time, and drives the formation of non-equilibrium steady-states (NESS), characterized by a finite flowing current.

1. Introduction to Non-equilibrium DMFT

DMFT theory was introduced to address strongly correlated systems in equilibrium and has been used successfully to describe key aspects of these systems such as the Mott transition [14].

Now, this method can naturally be adapted to study non-equilibrium correlated systems. In order to investigate the non-equilibrium dynamics of correlated systems, we use the so called Non-equilibrium Dynamical Mean Field Theory (NEQ-DMFT), a direct out-of-equilibrium extension of the DMFT method. Like this last one, its approach is based on a self-consistent formulation in terms of an effective single-site impurity problem. Moreover, the NEQ-DMF relies on an accurate solution of the impurity problem and can be implemented with a multitude of impurity solvers, including diagrammatic perturbative approaches, Quantum Monte Carlo and exact diagonalization.

In order to describe the non-equilibrium steady-states of correlated electrons driven by external electromagnetic fields in the context of NEQ-DMFT, we use the Keldysh formalism [13], that allows us to straightforwardly adapt to non-equilibrium the

equilibrium techniques used to study strongly correlated systems.

We define and adopt here an L-shaped contour $\mathcal{C}$ with three branches $\mathcal{C}_1 : 0 \to t_{max}$, $\mathcal{C}_2 : t_{max} \to 0$ and $\mathcal{C}_3 : 0 \to -i\beta$, as illustrated in Figure 2.1[14], where β is the inverse temperature and t_{max} is the maximum evolution time. We have already illustrated
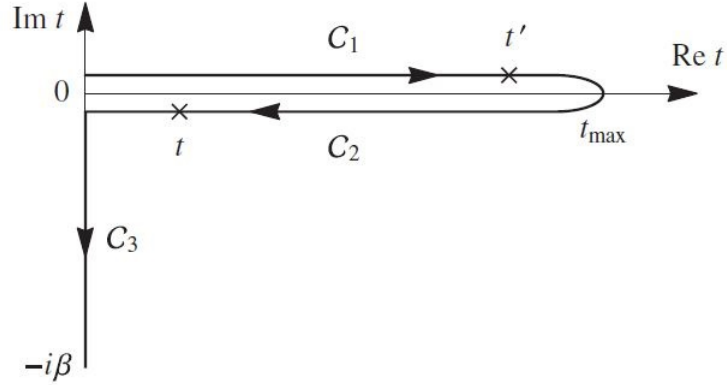

FIGURE 2.1. The L-shaped contour $\mathcal{C} = \mathcal{C}_1 \cup \mathcal{C}_2 \cup \mathcal{C}_3$ in the Keldysh formalism. The arrows indicate the contour-ordering.

the reasons why we adopt this type of contour in the first chapter. However, we now extend the contour to the imaginary time in order to start the non-equilibrium dynamics with an initially correlated state at finite time t.

The non-equilibrium Green's functions are defined on the contour $\mathcal{C}$, and depend on two different times (t, t'), rather than on the difference $(t - t')$ as in the equilibrium case. Once the $\mathcal{C}$-contour has been defined, the $\mathcal{T}_\mathcal{C}$ contour-ordering operator follows straightforwardly. It arranges the operators on the contour $\mathcal{C}$ in the order $0 \to t_{max} \to 0 \to -i\beta$, as indicated by the arrows in Figure 2.1.

In general, given two fermionic operators $\mathcal{A}(t)$ and $\mathcal{B}(t')$, where t, t' belong to $\mathcal{C}$, one can define:

$$(2.1) \qquad \mathcal{T}_\mathcal{C}[\mathcal{A}(t)\mathcal{B}(t')] = \theta_\mathcal{C}(t, t')\mathcal{A}(t)\mathcal{B}(t') - \theta_\mathcal{C}(t', t)\mathcal{B}(t')\mathcal{A}(t)$$

where $\theta_\mathcal{C}(t, t') = 1$ when $t > t'$, and $\theta_\mathcal{C}(t, t') = 0$ when $t < t'$.

The fundamental objects of many-body theories are the single-particle Green's functions. In fact, they describe single-particle excitations and statistical distribution of particles, and are the most important quantities of NEQ-DMFT. In general, we define [14] the non-equilibrium Keldysh Green's functions as the contour-ordered

expectation value:

$$(2.2) \qquad G_{\mathbf{k}}(t,t') =: -i\left\langle \mathcal{T}_{\mathcal{C}}[c_{\mathbf{k}}(t)c_{\mathbf{k}}^{\dagger}(t')]\right\rangle = \begin{pmatrix} G_{11} & G_{12} & G_{13} \\ G_{21} & G_{22} & G_{23} \\ G_{31} & G_{32} & G_{33} \end{pmatrix}$$

Because of the three branches, on which the time arguments t and t' can run, the Green's function has 9 components, depending on the location of each time argument on the contour. It is well-known that the components of the matrix (2.2) are not all independent from each other. Actually, this redundancy can be summarized with the following relation:

$$(2.3) \qquad\qquad G_{11} + G_{22} = G_{12} + G_{21}$$

Thanks to the redundancy (2.3) and the fact that the components of (2.2) are related via their Hermitian conjugates, one can reduce the number of independent components of the Green's function from 9 to 4. There are several possibilities of choice for the 4 independent Green's functions. We will consider the following quartet of independent Green's functions:

$$(2.4) \qquad\qquad G_{\mathbf{k}}^{M}(\tau,\tau') = -\langle\mathcal{T}(c_{\mathbf{k}}(\tau)c_{\mathbf{k}}^{\dagger}(\tau'))\rangle = -iG_{33}$$

$$(2.5) \qquad G_{\mathbf{k}}^{R}(t,t') = -i\theta(t-t')\langle[c_{\mathbf{k}}(t),c_{\mathbf{k}}^{\dagger}(t')]\rangle = \frac{1}{2}(G_{11} - G_{12} + G_{21} - G_{22})$$

$$(2.6) \qquad\qquad G_{\mathbf{k}}^{<}(t,t') = -i\langle c_{\mathbf{k}}^{\dagger}(t')c_{\mathbf{k}}(t))\rangle = G_{12}$$

$$(2.7) \qquad\qquad G_{\mathbf{k}}^{\neg}(t,\tau') = -i\langle c_{\mathbf{k}}^{\dagger}(\tau')c_{\mathbf{k}}(t))\rangle = \frac{1}{2}(G_{13} + G_{23})$$

defined as the Matsubara, retarded, lesser and left-mixing Green's function, respectively. Among all these Green's functions, the Matsubara component plays a very important and special role, because it is time-translational invariant. It means that, while all the other components depend on two different times (τ,τ'), the Matsubara component depends only on the difference $(\tau-\tau')$, and its Fourier decomposition in terms of Matsubara frequencies can be written as in (1.20).

The imaginary part of the retarded Green's function, as in (1.55), gives the so called single-particle spectral function $A(\omega)$, which provides information about the distribution with energy of the electronic states. At equilibrium, all the components of

Green's function are related to the spectral function by:

$$(2.8) \qquad G(t,t') = -i \int d\omega e^{-i\omega(t-t')} A(\omega)[\theta_{\mathcal{C}}(t-t') - f(\omega)]$$

where $f(\omega) = 1/(e^{\beta\omega} - 1)$ is the Fermi occupation function, which determines the probability the energy states are occupied. Moreover, the imaginary part of the lesser Green's function yields the distribution function:

$$(2.9) \qquad -Im G^<(\omega) = 2\pi A(\omega) f(\omega) = 2\pi N(\omega)$$

which furnishes information about the occupation of the electronic states. Actually, equation (2.9) is the fluctuation-dissipation relation for single-particle excitation. Out of equilibrium, all these quantities become meaningless, instead similar quantities must be defined, with different meaning with respect to the equilibrium case. The spectral function $A(\omega, t_{av})$ can be therefore defined as follows:

$$(2.10) \qquad A(\omega, t_{av}) = -\frac{1}{\pi} Im \int dt_{rel} e^{i\omega t_{rel}} G^R(t_{rel}, t_{av})$$

where $t_{av} = \frac{t+t'}{2}$ and $t_{rel} = t - t'$. In the same way, one can define the spectral occupation $N(\omega, t_{av})$ and the distribution $F(\omega, t_{av})$, related by:

$$(2.11) \qquad N(\omega, t_{av}) = A(\omega, t_{av}) F(\omega, t_{av})$$

which extends the fluctuation-dissipation theorem (2.9) out of equilibrium.

The three non-equilibrium functions depend on the frequency ω at every average time $t_{av} = \frac{t+t'}{2}$, and replace the equilibrium quantities, although with some differences. For example, the non-equilibrium spectral function $A(\omega, t_{av})$ is not normalized, therefore it does not represent a probability, but only a qualitative distribution in energy of the electronic states. The non-equilibrium distribution function $F(\omega, t_{av})$ replaces the Fermi-Dirac function $f(\omega)$ out-of equilibrium, and represents an electronic distribution probability out-of-equilibrium, that does not trace the equilibrium one. However, in the non-interacting regime the Hubbard Hamiltonian reduces to an easier tight-binding model (1.10). One can derive the equation of motion for the non-interacting Green's function $G_{0,k}(t,t')$, which reads:

$$(2.12) \qquad [i\partial_t + \mu - \epsilon_k(t)] G_{0,k}(t,t') = \delta_{\mathcal{C}}(t,t')$$

This equation determines $G_{0,k}$ uniquely if solved with the boundary conditions:

$$(2.13) \qquad G(0^+, t) = -G(-i\beta, t) \qquad G(t, 0^+) = -G(t, -i\beta)$$

One can express differently the equation of motion (2.12) by introducing the inverse of the Green's function:

$$(2.14) \qquad G_{0,k}^{-1}(t,t') = [i\partial_t + \mu - \epsilon_k(t)] \, \delta_{\mathcal{C}}(t,t')$$

which is an operator defined on the contour $\mathcal{C}$.

In order to describe a non-equilibrium correlated system by using the Green's function formalism, we need to take into account the self-energy Σ corrections to the non-interacting Green's function G_0. In this context, the self-energy is the sum of all one-particle irreducible diagrams of the interacting Green's function G (diagrams that cannot be separated into two parts by cutting single G_0 lines). The fully interacting Green's function is given then by the Dyson equation:

$$(2.15) \qquad \begin{aligned} G &= G_0 + G_0 * \Sigma * G_0 + G_0 * \Sigma * G_0 * \Sigma * G_0 + ... = \\ &= G_0 + G_0 * \Sigma * G = G_0 + G * \Sigma * G_0 \end{aligned}$$

where the symbol $(*)$ denotes a convolution, defined as follows:

$$(2.16) \qquad [f * g](t,t') = \int_{\mathcal{C}} d\bar{t} f(t,\bar{t}) g(\bar{t},t')$$

The evaluation of the self-energy Σ is the true non-equilibrium quantum many-body problem, for which one needs additional techniques. Once the self-energy is fixed, the full Green's function is determined from the integral equation (2.15). We can transform the Dyson equation from its integral form into a differential form by convoluting the equation (2.15) with the operator G_0^{-1} from the left (or right):

$$(2.17) \qquad [G_0^{-1} - \Sigma] * G = G * [G_0^{-1} - \Sigma] = \delta_{\mathcal{C}}$$

This result is conveniently expressed by:

$$(2.18) \qquad G^{-1} = G_0^{-1} - \Sigma$$

Equation (2.18) is formally identical to its equilibrium version (1.24), even if the two equations have deeply different physical meaning. One can see that the interacting Green's function $G_{\mathbf{k}}$ satisfies the Dyson equation which relates it to the self-energy function $\Sigma_{\mathbf{k}}$ and to the non-interacting propagator $G_{0,\mathbf{k}}$ in the integral-differential form:

$$(2.19) \qquad [i\partial_t - h(\mathbf{k},t)]G_{\mathbf{k}}(t,t') - \int_{\mathcal{C}} d\bar{t} \, \Sigma_{\mathbf{k}}(t,\bar{t})G_{\mathbf{k}}(\bar{t},t') = \delta_{\mathcal{C}}(t,t')$$

The equations (2.19) are causal, and provide a time-propagation scheme for G. Moreover, on the imaginary branch the same equations provide a boundary-value problem for the Matsubara Green's functions of an equilibrium state, which can be

used as initial value for the time propagation.

The equation (2.19) can be decomposed into a set of coupled differential equations for the independent components ((2.20) to (2.23)):

$$(2.20) \qquad \left[i\partial_\tau - h(\mathbf{k}, 0^-) \right] G_\mathbf{k}^M(\tau) = \delta(\tau) + \int_0^\beta ds \, \Sigma^M(\tau - s) G_\mathbf{k}^M(s)$$

$$(2.21) \qquad \left[i\partial_t - h(\mathbf{k}, t) \right] G_\mathbf{k}^R(t, t') = \delta(t - t') + \int_{t'}^t ds \, \Sigma^R(t, s) G_\mathbf{k}^R(s, t')$$

$$(2.22) \qquad \begin{aligned} \left[i\partial_t - h(\mathbf{k}, t) \right] G_\mathbf{k}^<(t, t') &= \int_0^t ds \Sigma^R(t, s) G_\mathbf{k}^<(s, t') + \\ & \int_0^{t'} ds \Sigma^<(t, s) G_\mathbf{k}^A(s, t') - i \int_0^\beta ds \, \Sigma^\neg(t, s) G_\mathbf{k}^\llcorner(s, t') \end{aligned}$$

$$(2.23) \quad \left[i\partial_t - h(\mathbf{k}, t) \right] G_\mathbf{k}^\llcorner(t, \tau') = \int_0^t ds \Sigma^R(t, s) G_\mathbf{k}^\llcorner(s, \tau') + \int_0^\beta ds \, \Sigma^\neg(t, s) G_\mathbf{k}^M(s, \tau')$$

where $G_\mathbf{k}^A$ and $G_\mathbf{k}^\llcorner$ are the advanced and right-mixing Green's functions.

The first of these equations can be solved by Fourier transforming to Matsubara frequency domain, and its solution represents the Green's function of the initial equilibrium state:

$$(2.24) \qquad G_\mathbf{k}^M(i\omega_n) = \left[i\omega_n - h(\mathbf{k}, 0^-) - \Sigma^M(i\omega_n) \right]^{-1}$$

Concerning the remaining equations, if one keeps fixed the second time argument on a suitable branch of the contour $\mathcal{C}$, it is easy to recognize that each of the equations (2.21) to (2.23) has the general form:

$$(2.25) \qquad \frac{d}{dt} f(t) + H(t) f(t) + \int_0^t ds K(t, s) f(s) = Q(t)$$

which is a linear Volterra Integro-Differential Equations (VIDE) [16] of the 2$^{\text{nd}}$ type, for a given choice of Q, H and the kernel K. These equations, as well as the related Volterra Integral Equations (VIE):

$$(2.26) \qquad f(t) + \int_0^t ds K(t, s) f(s) = Q(t)$$

have a causal structure, which is evident from the limits of the integral.

In order to solve a large number of coupled Volterra equations, very stable and high-accurate methods must be used. Remarkably, for our purposes a 2$^{\text{nd}}$-order algorithm already gives good results. Let us assume we have a stable algorithm to solve (2.25) and (2.26). The non-equilibrium DMFT algorithm is implemented with a time-propagation scheme: once you have obtained self-consistent solutions for G and $\mathcal{G}_0$ at time t through the DMFT-loop, you can proceed with the next time-step $t_1 = t + \Delta t$, and proceed always looking for convergence, generating a
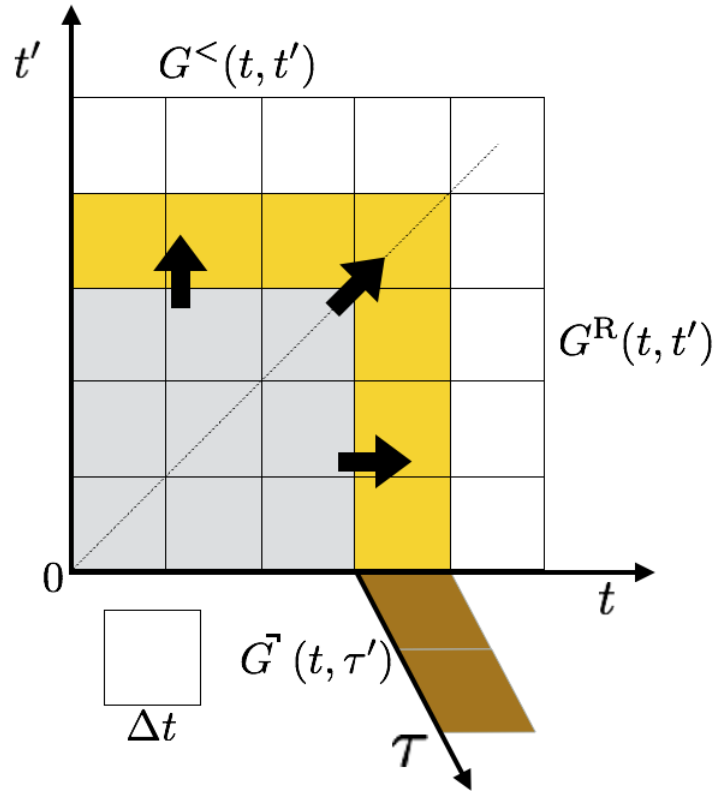
FIGURE 2.2. An example of time-step procedure. For graphical reason, the propagation of the lesser (<) component is 'vertical' (with respect to t'). This corresponds to a different choice of the Kadanoff-Baym equation to solve (the conjugate equation).

time dynamics. The Green's function propagation, called time-step, allows us to evolve the Green's function on horizontal/vertical and imaginary edges, linked to (t, t', τ), where τ is the imaginary time. In contrast with the equilibrium case, the non-equilibrium DMFT loops are computationally more costly, because the contour-ordered Green's functions depend on two time variable (t, t'). Specifically, the non-equilibrium DMFT algorithm consists in:

1. Read the equilibrium solution of the problem of interest, obtaining:

$$\Sigma(i\omega_n) \rightarrow \Sigma^M(\tau)$$

$$G_{\text{loc}}(i\omega_n) \rightarrow G_{\text{loc}}^M(\tau)$$

$$\mathcal{G}_0(i\omega_n) \rightarrow \mathcal{G}_0^M(\tau)$$

for all $\tau > 0$.

2. Set the initial condition for the Keldysh Green's functions. This step extends the equilibrium solution from the imaginary time interval to the initial time for the non-equilibrium Green's function.

   2.i Extend the Weiss-field components:

$$\mathcal{G}_0^<(0,0) = -i\mathcal{G}_0^M(\beta)$$

$$\mathcal{G}_0^R(0,0) = -i$$

$$\mathcal{G}_0^\urcorner(0,\tau) = -i\mathcal{G}_0^M(\beta - \tau)$$

  2.ii Extend the self-energy components. So far this step depends on the solver, we used IPT here.

$$\Sigma_0^<(0,0) = i^3\, U^2(0^+)\, \mathcal{G}_0^M(\beta)\, \mathcal{G}_0^M(0)\, \mathcal{G}_0^M(\beta)$$

$$\Sigma_0^>(0,0) = i^3\, U^2(0^+)\, \mathcal{G}_0^M(0)\, \mathcal{G}_0^M(\beta)\, \mathcal{G}_0^M(0)$$

$$\Sigma_0^R(0,0) = \Sigma^>(0,0) - \Sigma^<(0,0)$$

$$\Sigma_0^\urcorner(0,\tau) = i^3\, U(0^+)\, U(0^-)\, \mathcal{G}_0^M(\beta - \tau)\, \mathcal{G}_0^M(\tau)\, \mathcal{G}_0^M(\beta - \tau)$$

  2.iii Get the Green's functions for each $\mathbf{k}$-point in the Brillouin zone. In the current scheme this is the largest chunk of memory, of size $L_\mathbf{k}N_t^2$, where $L_\mathbf{k}$ is the number of $\mathbf{k}$ points and N_t is the maximum number of time steps.

$$G_\mathbf{k}^M(i\omega_n) = \left[i\omega_n - h(\mathbf{k},0^-) - \Sigma^M(i\omega_n)\right]^{-1} \rightarrow G_\mathbf{k}^M(\tau)$$

$$G_\mathbf{k}^<(0,0) = -iG_\mathbf{k}^M(\beta)$$

$$G_\mathbf{k}^R(0,0) = -i$$

$$G_\mathbf{k}^\urcorner(0,\tau) = -iG_\mathbf{k}^M(\beta - \tau)$$

  2.iv Get the derivative of the Green's function at the initial time. Note that these objects do not take much memory because we need them only at the boundary of the considered time-step. At the initial time, we obtain these quantities from the equations of motion they should satisfy:

$$\frac{d}{dt}G_\mathbf{k}^<(0,0) = -ih(\mathbf{k},0)G_\mathbf{k}^<(0,0) - \int_0^\beta ds\Sigma^\urcorner(0,s)G_\mathbf{k}^\lceil(s,0)$$

$$\frac{d}{dt}G_\mathbf{k}^R(0,0) = -ih(\mathbf{k},0)G_\mathbf{k}^R(0,0)$$

$$\frac{d}{dt}G_\mathbf{k}^\urcorner(0,\tau) = -ih(\mathbf{k},0)G_\mathbf{k}^\urcorner(0,0) - \int_0^\beta ds\Sigma^\urcorner(0,s)G_\mathbf{k}^M(s,\tau)$$

One can now start the time-stepping algorithm. At each step a full DMFT cycle is performed until convergence is obtained from an arbitrary error evaluation (we choose 1% of error allowed). The every-time-step-convergence provides to the system the necessary stability, and prevents the degradation of the dynamics.

3. For a fixed time step $I = 2, \ldots, N_t$ and $t = Idt$, initialize or guess the Weiss field $\mathcal{G}_0^{<,R}(I,J)$ for all $J \leq I$ and $\mathcal{G}_0^{\neg}(I,J)$ with $J = 1, \ldots, L_\tau$ and $\tau = Jd\tau$. The solution for $\mathcal{G}_0^{<}(I,J)$ with $I \leq J$ is obtained by symmetry. Similarly the greater component $>$ is obtained from $<$ and R components, as well as the $\llcorner$ component is obtained from the $\neg$ one. The guess for the new time-step is obtained by quadratic extrapolation of the Weiss field at past times.

4. Start the DMFT iterations at the time step I:

4a. Solve the impurity problem (using IPT), get the self-energy for all $t' \leq Idt$ and $\tau' \in [0,\beta]$:

$$\Sigma_U^{<}(t,t') = U(t)\, U(t')\, \mathcal{G}_0^{<}(t,t')\, \mathcal{G}_0^{>}(t',t)\, \mathcal{G}_0^{<}(t,t')$$

$$\Sigma_U^{>}(t,t') = U(t)\, U(t')\, \mathcal{G}_0^{>}(t,t')\, \mathcal{G}_0^{<}(t',t)\, \mathcal{G}_0^{>}(t,t')$$

$$\Sigma_U^{\neg}(t,\tau') = U(t)\, U(0^-)\, \mathcal{G}_0^{\neg}(t,\tau')\, \mathcal{G}_0^{\neg}(\tau',t)\, \mathcal{G}_0^{\neg}(t,\tau')$$

$$\Sigma_U^{R}(t,t') = \Sigma_U^{>}(t,t') - \Sigma_U^{<}(t,t')$$

for all $t = Idt$, $t' \in [0,t]$ and $t' = Idt$, $t \in [0,t']$.

4b. Add the thermostat bath to the self-energy function: $\Sigma(t,t') = \Sigma_U(t,t') + \Sigma_{\text{bath}}(t-t')$.

4c. Solve for all the $\mathbf{k}$ points in the Brillouin zone the Kadanoff-Baym equations for the independent components of the non-equilibrium Green's functions ((2.21) to (2.23)) using VIDE solutions with respect to $t = Idt \to (I+1)dt$ and for all fixed $t' = 1, \ldots, Idt$ or $t' = \tau$:

(2.27)
$$\frac{d}{dt}G_{\mathbf{k}}^{R}(t,t') + ih(\mathbf{k},t)G_{\mathbf{k}}^{R}(t,t') + i\int_{t'}^{t} ds\, \Sigma^{R}(t,s)G_{\mathbf{k}}^{R}(s,t') - i\delta(t-t')$$

(2.28)
$$\frac{d}{dt}G_{\mathbf{k}}^{<}(t,t') + ih(\mathbf{k},t)G_{\mathbf{k}}^{<}(t,t') + i\int_{0}^{t} ds\, \Sigma^{R}(t,s)G_{\mathbf{k}}^{<}(s,t') =$$
$$-i\int_{0}^{t'} ds\, \Sigma^{<}(t,s)G_{\mathbf{k}}^{A}(s,t') - i\int_{0}^{\beta} ds\, \Sigma^{\neg}(t,s)G_{\mathbf{k}}^{\llcorner}(s,t')$$

(2.29)
$$\frac{d}{dt}G_{\mathbf{k}}^{\neg}(t,\tau') + ih(\mathbf{k},t)G_{\mathbf{k}}^{\neg}(t,\tau') + i\int_{0}^{t} ds\, \Sigma^{R}(t,s)G_{\mathbf{k}}^{\neg}(s,\tau') =$$
$$-i\int_{0}^{\beta} ds\, \Sigma^{\neg}(t,s)G_{\mathbf{k}}^{M}(s-\tau')$$

Obtain the local interacting Green's function as: $\hat{G}_{\text{loc}} = \sum_{\mathbf{k}} \hat{G}_{\mathbf{k}}$.

4d. Impose the self-consistency condition. This is done by recasting the self-consistency $\mathcal{G}_0^{-1}(Idt, t') = G_{\text{loc}}^{-1}(t, t') + \Sigma(t, t')$ into the form of a VIE with respect to t:

$$\mathcal{G}_0(t, t') + [K * \mathcal{G}_0](t, t') = G_{\text{loc}}(t, t')$$

where $K = G_{\text{loc}} * \Sigma$ and $t = Idt$, $t' = 1, \ldots, Idt$ or $t' = \tau'$.

4e. Measure the observables at time $t = Idt$. Evaluate the error

$$E = \frac{\left| \int_{\mathcal{C}} \mathcal{G}_0(t, s) - \mathcal{G}_0^{\text{OLD}}(t, s) \right|^2}{\left| \int_{\mathcal{C}} \mathcal{G}_0(t, s) \right|^2}$$

.

If $E > \varepsilon$ convergence is not yet achieved: restart from point 4a.

If $E < \varepsilon$ convergence is achieved: go to point 3.

A simplified flowchart of the NEQ-DMFT algorithm is reported in Figure 2.3.
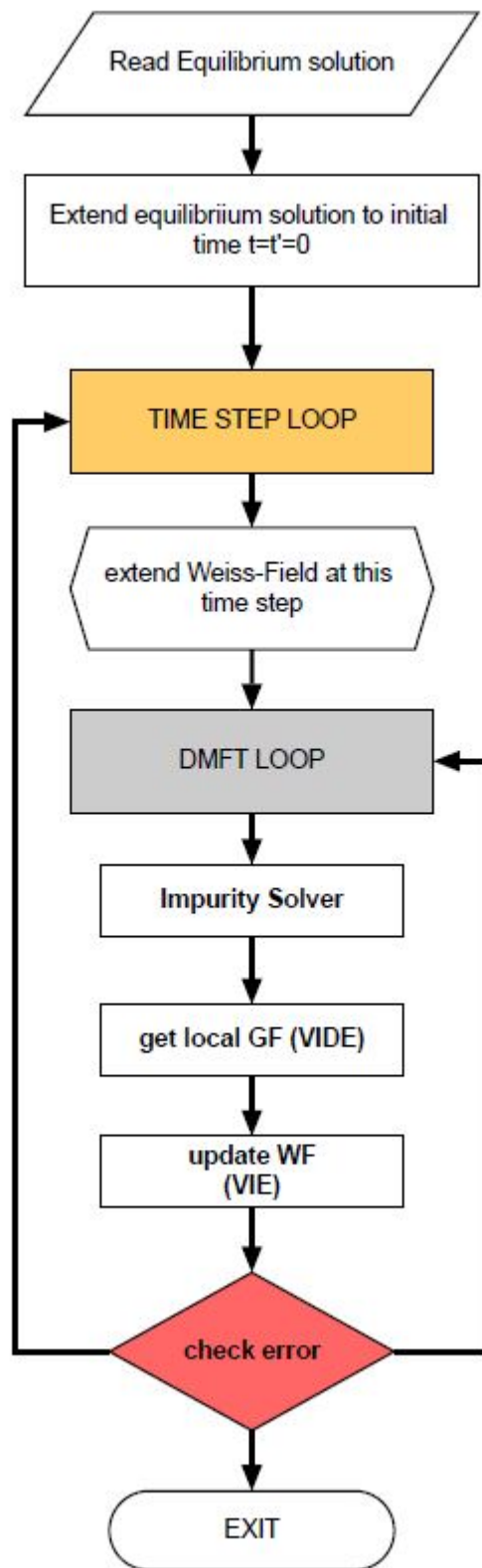
FIGURE 2.3. Flowchart of the non-equilibrium DMFT algorithm, with the DMFT loop incorporated in the time-step loop.

2. Bloch oscillations and the need for a scattering mechanism

The effects of an applied DC field on a lattice system are deeply different accord-
ing to the presence or absence of scattering mechanism in the system itself. In the
absence of electron scattering mechanism, we deal with a completely coherent sys-
tem, without any type of energy dissipation. In this ballistic regime, a DC field
applied to the metallic system will result in an undamped oscillating current, a phe-
nomenon known as *Bloch oscillations*[11][17]. This phenomenon derives from the
semi-classical studies of the motion in a crystal of an electron having wave-number
$\mathbf{k}$, subjected to a steady electric field $\mathbf{E}$, directed in the positive x direction. When
the strength of the electric field is sufficiently small, or the band gaps are sufficiently
large, the inter-band Zener tunnelling can be neglected. In this situation, an electron
in a given energy band of a perfect periodic crystal, subjected to the electric field $\mathbf{E}$
for a small time dt, gains the following energy:

$$(2.30) \qquad dE = -e\mathbf{E}vdt = -e\mathbf{E}\frac{1}{\hbar}\frac{dE}{dk}dt$$

From (2.30), the following equation can be obtained:

$$(2.31) \qquad d\mathbf{k} = -e\mathbf{E}\frac{1}{\hbar}dt \quad \rightarrow \quad \mathbf{k}(t) = \mathbf{k}_0 - \frac{e}{\hbar}\mathbf{E}t$$

where $\mathbf{k}_0 = \mathbf{k}(t_0)$ is the electron wave-number at the initial time t_0 and e is the elec-
tron charge. The equation (2.31) is known as *acceleration theorem*, and represents
the semi-classical equation of motion for the electrons in an energy band subjected
to the electric field $\mathbf{E}$.

With reference to Figure 2.4 [11], an electron of initial $\mathbf{k}_0 = 0$ is first accelerated
under the influence of the electric field $\mathbf{E}$, acquiring energy and velocity. At the top
of the energy band $(k = -\pi/a)$ its velocity vanishes; in the absence of inter-band
tunnelling, the electron continues its path on the same band from $k = +\pi/a$ and it
begins to lose energy, until it reaches again the initial state at $k = 0$. This motion
is periodic in reciprocal space as well as in real space, where the electron oscillates
between its initial position and the end point. The result is an oscillating current
(Bloch oscillations) that prevents transport inside the material. The frequency and
the period of these oscillations are respectively:

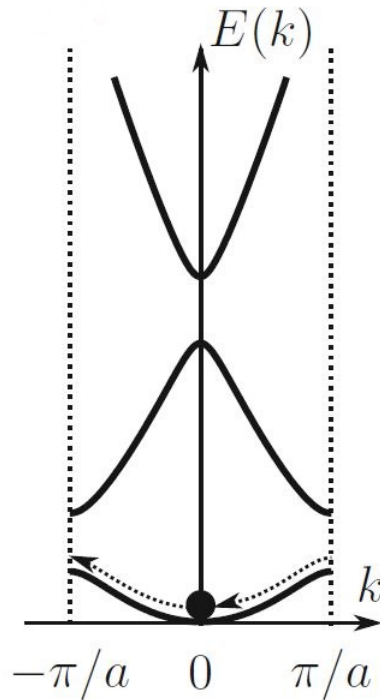$$(2.32) \qquad \omega_B = \frac{ae\mathbf{E}}{\hbar} \qquad T_B = \frac{2\pi\hbar}{a}\frac{1}{e\mathbf{E}}$$

FIGURE 2.4. Representation of the motion of an electron in an energy band. The electron, accelerated by the electric field **E**, travels through the Brillouin zone, generating an oscillating motion (Bloch oscillations) in the real space, that does not contribute to electric current.

By substituting typical values of a in crystals (several tenths of nanometres), one can find that the period of the Bloch oscillation is typically much longer that the electron-electron scattering time (which is in the femtoseconds regime). For this reason, it is very difficult to experimentally observe Bloch oscillations in real metals, which in fact generally show diffusive electric transport.

Until now, we have considered the semi-classical motion of the electron in the highly idealized situation of a collisionless regime. To explain how real metals could transport electric current, some deviations from the ideal periodic lattice must be taken into account.

Treating the microscopic behaviour of electrons classically, we assume that the motion of electrons is limited by a thermalization time τ, that represents the mean time between two consecutive collisions, and that can be used to explain the phenomenon of electric transport, being inserted in the equation of motion of the electron, which

reads:

$$(2.33) \qquad m^* \, \frac{d\mathbf{v}(t)}{dt} = -e\mathbf{E} - \frac{m^*\mathbf{v}(t)}{\tau}$$

where $\mathbf{v}(t)$ is the electron velocity at time t and m^* is the effective mass. The last term in equation (2.33) is a dissipative term, which takes into account electronic collisions. One can easily see [11] that Bloch oscillations result damped when a scattering time τ appears in the system, and the motion of electrons in real space is no more oscillatory. The explanation of this effect is a loss of electronic coherence with time, caused by the dissipative mechanism τ, that provides a channel of relaxation. As a result of this process, the quantum behaviour of electrons is apparently lost, just as energy appears to be lost by friction in classical mechanics, and transport properties of the material can be observed.

In the next sections, we will analyse the role of the scattering time τ in the system, and how is possible to couple our system, modelled as a Hubbard model, both with an external heat bath and an external electromagnetic field, in order to study its dynamics.

3. Coupling with an external thermostat

The coupling with an external heat bath in the out-of-equilibrium dynamics of a correlated system is of crucial importance [14][18][19]. The role of the external bath, which has a lot more degrees of freedom than the system itself, is to dissipate the energy injected in the system by the external field. Actually, in a real material many different scattering mechanisms take place, such as electron-phonon, electron-electron or electron-bosons interaction, or the coupling with spin or magnetic degrees of freedom. All these scattering mechanisms provide relaxation channels for the system, making the transport diffusive enough to allow the current flow. In other words, the external environment provides the dissipation of the energy injected by the external electric field. In this situation, the temperature of the system does not increase indefinitely, rather the system approaches a stable non-equilibrium steady state (NESS), under continuous external field driving. The NESS are hidden states not accessible thermally, characterized by the flow of finite electric current, that lets the non-equilibrium system maintain the internal energy conserved on average, thanks to the coupling with the external bath.

One of the simplest model of dissipative bath is the free fermion bath [19], which consists in coupling the system to a set of fermionic reservoirs that impose a constraint on the equations of motion of the system, as illustrated in Figure 2.5. Exploiting
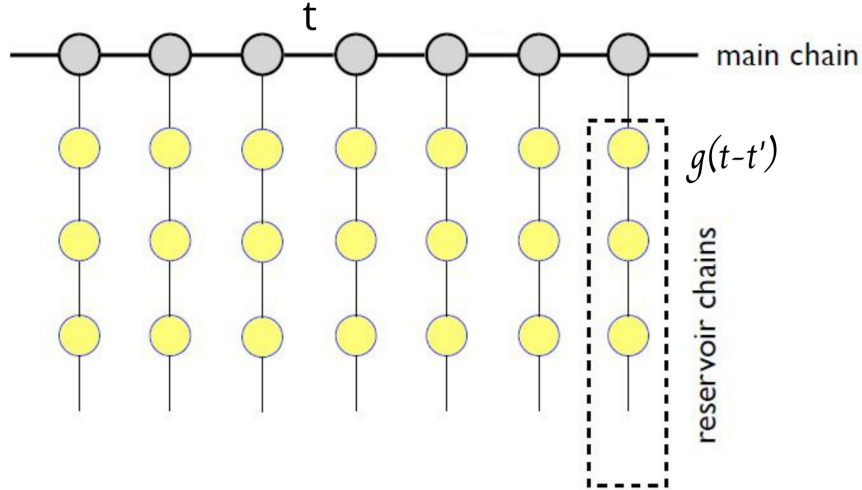

FIGURE 2.5. Schematic representation of a one-dimensional tight-binding lattice with hopping t coupled to an external bath. Each lattice site is connected to an identical fermionic bath, which provides the dissipation mechanism.

the local nature of DMFT, one can locally couple the conduction electrons to an external bath of non-interacting electrons at a fixed temperature T (β is the inverse temperature, rescaled by k_B, the Boltzmann constant). This coupling breaks the momentum conservation, and allows the conduction electrons' momenta (accelerated by the application of the field) to relax and drive the formation of NESS. Despite its simplicity, the fermionic thermostat represents a minimal set-up for the studies of strong correlation effects in driven lattice models.

We call V_p the hybridization between the system and the mode p of the bath, and we take $V_p = V$ to be constant and homogeneous. Each site of the lattice is coupled with a thermostat, such that an electron can hop between the lattice and the thermal bath, which is assumed to be unaffected by the presence of the electric field. In addition, the particular details of the internal structure of the thermal bath are irrelevant with respect to the physics of the NESS.

Thus, we consider a set of identical systems with a constant flat density of states

with bandwidth W [19]. The system with the thermostat has to obey the following Dyson equation on the contour $\mathcal{C}$:

$$(2.34) \qquad G_k(t,t') = G_{0k}(t,t') + [G_{0k} * \Sigma_k * G_k](t,t')$$

where all quantities are continuous operators depending on two time variables (t,t') defined on the contour $\mathcal{C}$, $\Sigma_k(t,t')$ is the Keldysh self-energy and the symbol $(*)$ denotes the convolution product (2.16). One can write down the equation (2.34) in terms of the renormalized non-interacting lattice Green's function G_{0k}:

$$(2.35) \qquad G_{0k}^{-1}(t,t') = [\bar{G}_{0k}^{-1}(t,t') - \Sigma_{bath}(t-t')]$$

obtained from the bare non-interacting lattice green's function

$$(2.36) \qquad \bar{G}_{0k}^{-1}(t,t') = [i\vec{\partial}_t - \epsilon(k)] \cdot \delta_{\mathcal{C}}(t,t')$$

by integrating out locally the electronic degrees of freedom of the external thermostat. The net effect of the external thermostat on the non-equilibrium dynamics of the system is to introduce an additional self-energy $\Sigma_{bath}(t-t')$:

$$(2.37) \qquad \Sigma_{bath}(t-t') = V^2 g(t-t')$$

where $g(t-t')$ is the Fourier transform of the non-interacting local bath Green's function corresponding to a flat density of states:

$$(2.38) \qquad g(\omega) = \frac{1}{W}\left[ln|(W/2+\omega)/(W/2-\omega)| - i\pi\theta\left(\frac{W}{2} - |\omega|\right)\right]$$

The bath self-energy is by construction time-translation invariant (it does not have momentum dependence) because it neglects the effects of the external electric field on it, but rather has the only role to dissipate the energy coming from the electric field. Moreover, one can divide Σ_{bath} into its real and imaginary part. The latter component represents the spectral function of the bath, while the former can be absorbed into the chemical potential, because it represents only a potential shift due to the coupling with the bath. For this reason, only ImΣ affects the dynamics of the system. Furthermore, from (2.38), one can identify the parameter:

$$(2.39) \qquad \Lambda = \frac{V^2}{W}$$

as an effective coupling of the system with the external thermal bath, that will be used through the entire our work as reference for the strength of the bath coupling. Roughly speaking, Λ can be interpreted as the probability of the electron to 'hop' into the bath V, propagate inside the bath $(1/W)$ and 'hop' again into the system

V. During the future calculations, one will always has to compare the value of Λ with the hopping t, which in our case is equal to 1. A general warning is to keep $\Lambda \leq 1$, in order to avoid a dynamics completely dominated by the coupling with the external bath. Otherwise, the single site would have more probability to couple with the bath rather than with the other sites of the system, and the bath would become actually part of the system itself.

4. Coupling with an external electric field

In this section, we will formalise the interaction of our system with an external electric field $\mathbf{E}$, which drives the system out-of-equilibrium [14][20]. We consider a bidimensional single-band Hubbard model on a tight-binding square lattice of spacing a at half-filling, with paramagnetic solution (no long-range order is established). The coupling with an external electric field is included in the Hamiltonian of the system, which reads:

$$(2.40) \qquad H = \sum_{\mathbf{k}\sigma} \epsilon \left[\mathbf{k} - \frac{e}{\hbar} \mathbf{A}(t) \right] c^{\dagger}_{\mathbf{k}\sigma} c_{\mathbf{k}\sigma}$$

where $\mathbf{A}(t)$ is the internal vector potential. This model describes non-interacting electrons with only nearest-neighbour hopping t, whose amplitude is fixed $t = 1$ throughout our calculations, as the energy unit (at which every quantity is referred). The hopping determines the dispersion relation for the bidimensional square lattice:

$$(2.41) \qquad \epsilon(\mathbf{k}) = -2t \left[cos(k_x a) + cos(k_y a) \right]$$

in agreement with (1.9).

In general, the Hubbard Hamiltonian can contain external perturbations, such as electromagnetic fields. For the single-band model, the coupling with the electromagnetic field is realized through the Peierls substitution. This method introduces the vector potential $\mathbf{A}(\mathbf{r}, t)$ as a phase factor in the hopping matrix elements, as follows:

$$(2.42) \qquad t_{ij}(t) = t_{ij} \ exp\left(-\frac{ie}{\hbar} \int_{\mathbf{R}_i}^{\mathbf{R}_j} d\mathbf{r} \cdot \mathbf{A}(\mathbf{r}, t) \right)$$

Thus, the hopping term becomes time-dependent due to the introduction of the Peierls substitution for the time-dependent (but spatially uniform) electric field. The electric field is described via a spatially uniform vector potential in the Hamiltonian gauge:

$$(2.43) \qquad \mathbf{E}(t) = -\frac{d\mathbf{A}(t)}{dt}$$

The Peierls substitution derives from the requirement that the Hamiltonian H has to be invariant under the following gauge transformations:

$$(2.44) \qquad c_{i\sigma} \to c_{i\sigma} \, exp\left(\frac{ie}{\hbar} \, \chi(\mathbf{R}_i, t)\right)$$

$$(2.45) \qquad \mathbf{A}(\mathbf{r}, t) \to \mathbf{A}(\mathbf{r}, t) + \nabla\chi(\mathbf{r}, t)$$

$$(2.46) \qquad \Phi(\mathbf{r}, t) \to \Phi(\mathbf{r}, t) - \frac{\partial\chi(\mathbf{r}, t)}{\partial t}$$

For this reason, the $\mathbf{r}$ dependence of $\mathbf{A}(\mathbf{r}, t)$ is neglected, under the approximation that the field $\mathbf{A}(t)$ varies slowly on the atomic scale, having long (optical) wavelengths. The resulting dispersion, after the Peierls substitution, reads:

$$(2.47) \qquad \epsilon_{\mathbf{k}}(t) = \epsilon\left(\mathbf{k} - \frac{e}{\hbar}\mathbf{A}(t)\right)$$

where $\epsilon(\mathbf{k})$ is the equilibrium dispersion, in absence of fields.

Once the coupling with the external electric field has been defined, the study of the system can be carried out by evaluating some physical observables. Equal time observables such as current density, occupation density and kinetic energy can be computed directly from the lattice Green's functions.

Actually, when an external electromagnetic field is applied on the system, the Green's functions are not *a priori* gauge invariant. Under the gauge transformation, the Green's functions $G_{ij}(t, t') = -i\left\langle \mathcal{T}_{\mathcal{C}}[c_i(t)c_j^\dagger(t')]\right\rangle$ transform as:

$$(2.48) \qquad G_{ij}(t, t') \to G_{ij}(t, t') \, exp\left(\frac{ie}{\hbar} \, [\chi(\mathbf{R}_i, t) - \chi(\mathbf{R}_j, t')]\right)$$

Physical observables such as the current density or the kinetic energy have to be gauge invariant (independent on the choice of the gauge). For this reason, the Green's functions can not be used in the form (2.48), instead they need a covariant transformation in order to eliminate the change of the phase, and leave a $\tilde{G}$ gauge invariant. This transformation is given by:

$$(2.49) \qquad \tilde{G}_{ij}(t, t') = G_{ij}(t, t') \, exp\left(\frac{-ie}{\hbar} \int_{(\mathbf{R}_j, t')}^{(\mathbf{R}_i, t)} [d\bar{\mathbf{r}} \cdot \mathbf{A}(\bar{\mathbf{r}}, \bar{t}) - d\bar{t}\Phi(\bar{\mathbf{r}}, \bar{t})]\right)$$

For a uniform electric field, one can take the temporal gauge ($\Phi = 0, \mathbf{A} = \mathbf{A}(t)$), in order to make the local Green's function gauge invariant ($G_{ii}(t, t') = \tilde{G}_{ii}(t, t')$). On the other end, the equal time Green's functions become gauge invariant if one shifts the momentum k according to:

$$(2.50) \qquad G_{\mathbf{k}+\mathbf{A}(t)}(t, t) = \tilde{G}_{\mathbf{k}}(t, t)$$

Now, it is possible to construct and calculate the gauge invariant physical observables. The number of occupation $n_{i,\sigma}(t)$, for example, represents the number of electrons with spin σ on site i at time t, and it is defined as:

$$(2.51) \qquad n_{i,\sigma}(t) = \left\langle c_{i\sigma}^{\dagger}(t)c_{i\sigma}(t) \right\rangle = -iG_{ii,\sigma}^{<}(t,t) = -i\tilde{G}_{ii,\sigma}^{<}(t,t)$$

Out of equilibrium, the Fermi-Dirac function is no more the distribution function, instead it is proportional to $G^{<}$, which gives information about the electronic levels population. Moreover, the current density is defined as:

$$(2.52)$$
$$\mathbf{j}(t) = -\frac{ie}{V}\sum_{\mathbf{k}\sigma}\mathbf{v}_{\mathbf{k}\text{-}\mathbf{A(t)}}G_{\mathbf{k},\sigma}^{<}(t,t) = -\frac{ie}{V}\sum_{\mathbf{k}\sigma}\mathbf{v}_{\mathbf{k}}G_{\mathbf{k}+\mathbf{A}(t),\sigma}^{<}(t,t) = -\frac{ie}{V}\sum_{\mathbf{k}\sigma}\mathbf{v}_{\mathbf{k}}\tilde{G}_{\mathbf{k},\sigma}^{<}(t,t)$$

where $\mathbf{v}_k$ is the group velocity of the wave packet (Bloch electrons), defined as:

$$(2.53) \qquad \mathbf{v}_{k}(t) = \frac{1}{\hbar}\partial_{\mathbf{k}}\epsilon_{\mathbf{k}}(t) = \frac{1}{\hbar}\partial_{\mathbf{k}}\epsilon\left(\mathbf{k} - \frac{e}{\hbar}\mathbf{A}(t)\right)$$

In the end, from the Green's functions, one can also get the kinetic energy:

$$(2.54) \qquad E_{kin}(t) = \frac{-i}{L}\sum_{jl}t_{jl}(t)G_{lj,\sigma}^{<}(t,t)$$

where L is the number of lattice sites.

4.1. IPT method out-of-equilibrium.

Even in out-of-equilibrium systems, like in equilibrium ones, the conservation of the density at half-filling is crucial, in order to obtain reliable results. Unfortunately, once the coupling with the thermal bath Λ is fixed, one can not increase U indiscriminately, and approach the Mott transition. The reason is that out of equilibrium the fortuitous coincidence that allowed IPT to interpolate from weak to strong coupling is no more valid. As already said, in equilibrium the non-conservative IPT method has a large convergence radius, that allows the investigation of the systems even at high U, until the Mott transition. Out of equilibrium, this fact is no more valid, and the IPT method regains its perturbative character, working only at low U [12]. As we will see, the convergence radius of the theory is deeply connected with the dissipation Λ. When $\Lambda = 0$, the dynamics does not conserve the energy and the number of particles. Instead, it was shown that the presence of a finite coupling Λ expands the convergence radius (even if it is not possible to arrive at the Mott transition). The reason of this is that the bath is at half-filling by construction, and a strong coupling Λ helps the system to remain at half-filling, conserving the density.

Actually, nowadays there are no known methods (exact or approximated) that allow to investigate the properties of a correlated system driven out of equilibrium at the

Mott transition point. If one wants to investigate the Mott transition, more accurate and conservative methods can be used (Monte-Carlo or DMRG), which however do not allow very long dynamics. Another opportunity is the non-crossing approximation, which allows a strong-coupling expansion. Actually, it works well in the Mott insulator phase but it is not able to approach the transition point. In the rest of our work, we will tune properly the coupling Λ, according to the maximum value of interaction U we want to address, in order to keep the density in a fixed range (we allow a maximum error of 1%).

5. Units of measurement conversion

In this section, we discuss the conversion between the units of measurement we use throughout the entire work and the corresponding real values. First of all, all the energy values are expressed in unit of the hopping t, which from here will be used as the reference energy unit. We consider the hopping $t = 0.5$ eV, from which all the other quantities can be derived. Recalling that $\hbar = 6.582... \cdot 10^{-16}$ eV·s, the time unit T is:

$$(2.55) \qquad\qquad T = \hbar/t \sim 1.3 \cdot 10^{-15} \; s$$

From (2.31), the electric field unit is:

$$(2.56) \qquad\qquad \mathbf{E} = \frac{t}{ea} = 10^9 \; V/m$$

where we choose the lattice constant $a = 0.5$ nm. We define the frequency unit as:

$$(2.57) \qquad\qquad \omega_0 = \frac{t}{\hbar} \sim 0.76 \cdot 10^{15} Hz$$

Generally, a correlated system has a Mott gap in the order of 1.5 eV. Let us consider the relation between the photon energy and the wavelength of the light:

$$(2.58) \qquad\qquad E_{photon}(eV) = \frac{hc}{e\lambda}$$

where c is the speed of light and λ the light wavelength.
Using (2.58), we choose a light wavelength $\lambda = 800$ nm, that corresponds to an energy of about 1.5 eV, in the order of the Mott gap. The frequency ν of the light is therefore:

$$(2.59) \qquad\qquad \nu = \frac{c}{\lambda} = 0.375 \cdot 10^{15} Hz$$

The corresponding angular frequency is:

$$(2.60) \qquad\qquad\qquad \omega = 2\pi\nu = \pi$$

in units of frequency.

From equation (2.59), the period of oscillation is:

$$(2.61) \qquad\qquad\qquad \tau = \frac{1}{\nu} \sim 2.67 fs$$

In the end, we fix the inverse temperature $\beta = \frac{1}{k_B T}$, where k_B is the Boltzmann constant, equal to 10 throughout the entire work. Thus, $k_B T = 0.1$ (in hopping unit), whose conversion reads:

$$(2.62) \qquad\qquad\qquad k_B T = 0.1 \cdot 0.5 eV = 0.05 eV$$

Recalling $k_B = 8.617... \cdot 10^{-5} eV \cdot K^{-1}$, the temperature of the system is therefore:

$$(2.63) \qquad\qquad\qquad T = 580 K$$

The choice of $\beta = 10$, which is a quite high temperature, is done taking into account that the application of an external electric field on the system causes a sudden rise of temperature, that remains high also when NESS are formed.

6. The thermalization time

The coupling of the system with an external environment that provides a relaxation channel is crucial in order to describe the energy dissipation of the system itself. In our tight-binding system, this scattering channel is provided by the coupling Λ with a free fermion bath, that allows the formation of NESS [18][21]. In the non-interacting model, the phenomenological effect of the thermal bath can be summarized with the introduction of a thermalization time τ, which limits the collisionless motion of the electrons. This time scale represents the average time between two successive collisions of one electron, and can be used to quantify the relaxation time of the system.

Actually, the coupling of the system with the bath generates its own dynamics, even in the absence of an electric field **E**. This happens because the system is initially prepared as decoupled from both the thermal bath and the electromagnetic field. This type of dynamics (in the absence of electric field) can be investigated looking at the time evolution of the system kinetic energy (2.54), which shows a relaxation dynamics caused by the coupling Λ between the system and the external fermionic

bath.

In Figure 2.6, we plot the temporal evolution of the system kinetic energy at different values of coupling Λ, in order to establish a relation between the thermalization time τ and the strength of the coupling. Looking at Figure 2.6, one can observe that the
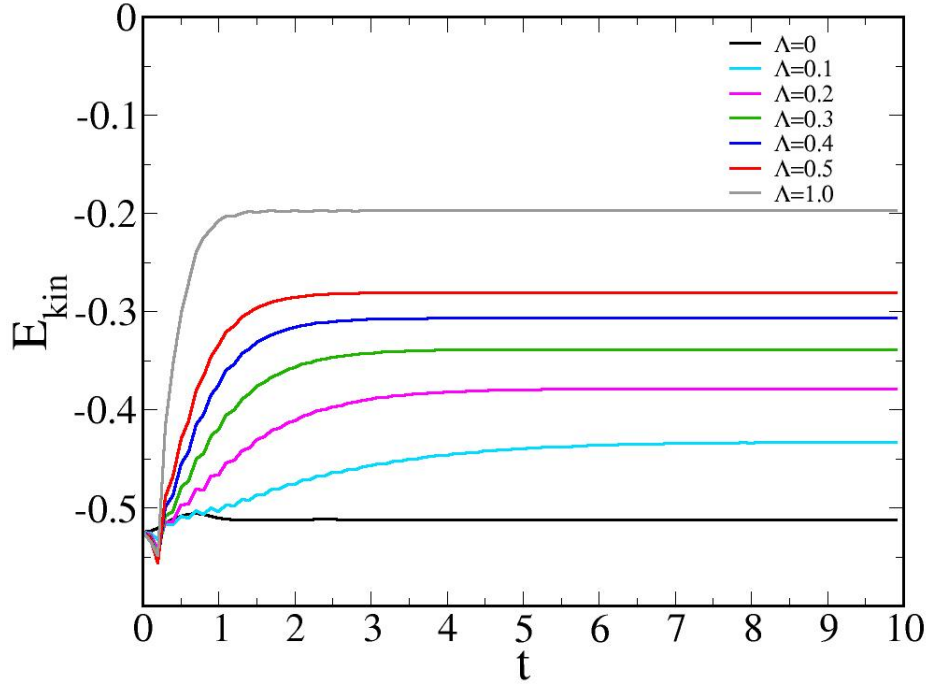

FIGURE 2.6. Time-evolution of the kinetic energy of the system, at different coupling Λ with the thermostat. The kinetic energy of the system relaxes at a finite value in a characteristic time τ, taken as the thermalization time of the system.

kinetic energy is always negative, whichever is the coupling Λ used. A negative kinetic energy indicates that the system is bound, as we expected from our model. Each of the curves has an initial dynamics, before relaxing to a fixed value after some time, pointing out that the system has equilibrated with the external thermal bath. In order to estimate the characteristic time of the system, *i.e.* the time taken by the system to go in equilibrium with the external bath, we fit each of these curve with a negative exponential decreasing function:

$$(2.64) \qquad y = A_0 + A_3 \cdot exp\left[-\frac{(x - A_1)}{A_2}\right]$$

where A_0, A_1, A_2 and A_3 are the fitting parameters and A_2 was chosen as the characteristic time. In Figure 2.7, we plot the extracted characteristic time τ vs the
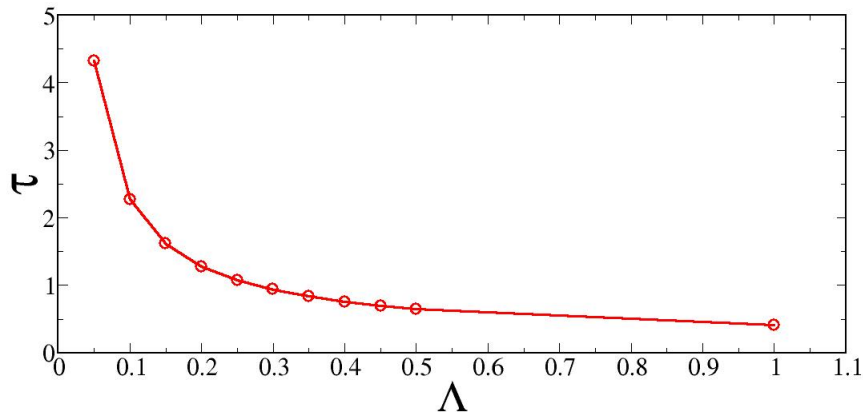
FIGURE 2.7. Thermalization time τ vs coupling Λ with the thermo-
stat. The decreasing behaviour of τ with Λ is consistent with the
Drude scattering, so that a system more coupled with the external
bath presents a lower scattering time τ.

coupling strength Λ; as we expected, the thermalization time τ decreases when Λ
increases. In fact, as Λ is increasing, the system is more coupled with the external
thermal bath; for this reason it will take less time to go in equilibrium with it, and
the thermalization time will be lower. We obtain therefore a connection between the
coupling Λ and the scattering time τ, which represents the relaxation time scale of
our system. As visible in Figure 2.7, the thermalization time τ of an intermediate
value of Λ, such as $\Lambda = 0.3$, is about 0.94, which is equivalent to 1.2 fs, in agreement
with typical electron-electron scattering time in solids.

7. Non-equilibrium steady-states

In this section, we use the already described NEQ-DMFT algorithm to solve the set
of coupled differential equations for the lattice Keldysh Green's function, by using
the second-order IPT as impurity solver. This method allows to extend the non-
equilibrium solution at any time (taking into account that the computational cost
of the single time-step is continuously growing).
According to the problem one has to face, two time parameters can be tuned to
choose the length of the system dynamics: the time-step Δt, which gives the time
unit, and the total number of time-steps N_t. Of course, the total temporal length
of the dynamics will be $\Delta t \, N_t$. One can modify the values of these parameters,
in order to better approach the variety of problems; generally, the lower Δt is,

the more precise will be the numerical solution. Of course, N_t can be neither too low, because it would prevent us to investigate longer dynamics, nor be too high, because the entire calculation would be too computationally expensive. The real challenge consists in properly tuning these two parameters, adapting their values to the specific dynamics considered, depending on the external electric field $\mathbf{E}$ and the bath coupling Λ. Throughout our work we fix $\Delta t = 0.1$, in order to have a good temporal resolution, and vary N_t according to the desired length of the dynamics. We also fix the number of Matsubara frequencies $N_M = 8192$, that must be a power of 2 in order to reduce the computational cost of the algorithm.

7.1. NESS: results.

In this section, we investigate the dynamics of a bidimensional single-band Hubbard model on a square lattice of spacing a, at half filling. A constant and homogeneous electric field $\mathbf{E}$, derived from a vector potential $\mathbf{A}(t)$, drives the metallic system (we fix $U = 0$) out of equilibrium. We consider a sudden switch of the electric field,
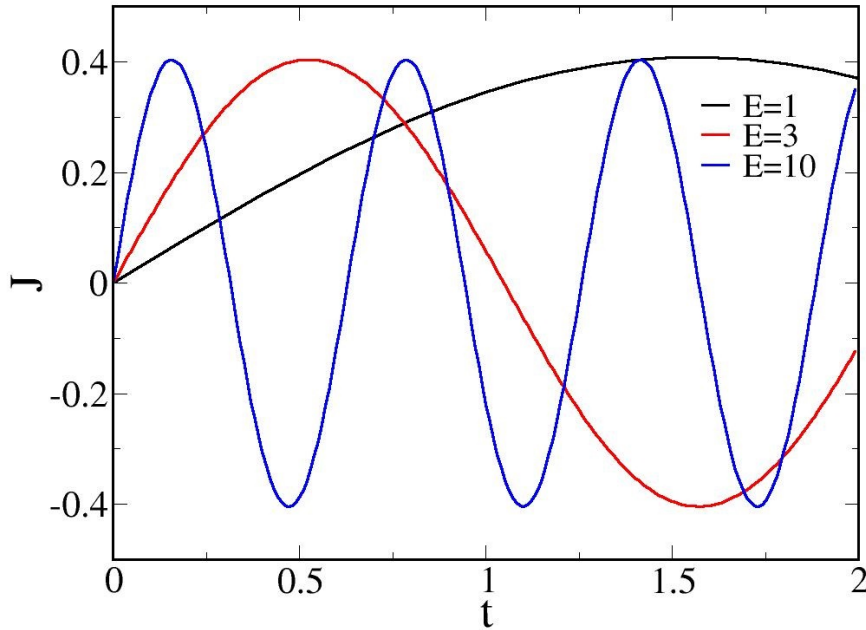

FIGURE 2.8. Current density $\mathbf{J}(t)$ flowing in the completely coherent system ($\Lambda = 0$), varying the applied DC field $\mathbf{E}$. Bloch oscillations (with period depending on the strength of the electric field) are recovered.

as well as of the coupling dynamics with the external thermostat, at $t = 0$. The combination of the two couplings favours the formation of NESS, by suppressing the

Bloch oscillations of the current [18][22]. Let us first consider a completely coherent system, with coupling ($\Lambda = 0$). In this situation, when an electric field **E** is applied on the system, Bloch oscillations are recovered, as visible in Figure 2.8. For graphical reasons, we plot the current density until $t = 2$. As expected from (2.32), the period of Bloch oscillations decreases with the field intensity. In Figure 2.9, we plot this period T vs the amplitude of the electric field **E**. As expected, the period T of
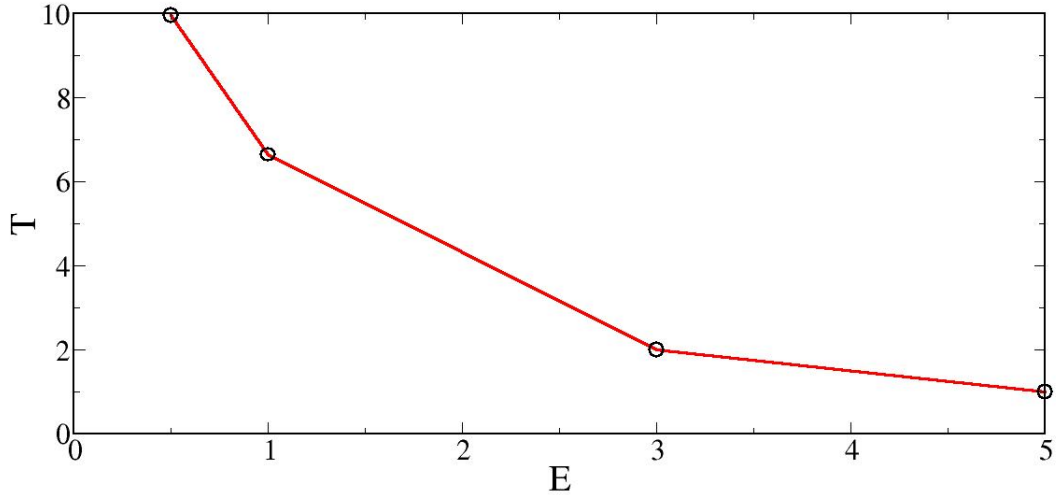
FIGURE 2.9. Period T of Bloch oscillations vs applied electric field **E**. The period T of Bloch oscillations is inversely proportional to the electric field applied.

the Bloh oscillations is inversely proportional with the applied field **E**, according to (2.32). Moreover, combining (2.32) with (2.55) and (2.56), we obtain the relation $T = 2\pi/\mathbf{E}$, consistent with the simulations results.

As already said, the presence of an external heat bath, which provides the scattering mechanism and absorbs the work done on the system by the field, drives the formation of finite-current non-equilibrium steady states.

We now concentrate on the approach to the NESS, that can be characterized following the real-time dynamics of suitable observables, such as the local current density $\mathbf{J}(t)$:

$$(2.65) \qquad\qquad \mathbf{J}(t) = -\frac{ie}{\pi} \sum_k \mathbf{v}_k G_k^<(t,t)$$

where $\mathbf{v}_k = \nabla_k \epsilon(k)$ is the electronic velocity, defined as the gradient of the dispersion $\epsilon(k)$. We look at the time-evolution of the local current density $\mathbf{J}(t)$ obtained at fixed value $\mathbf{E} = 1$, varying the coupling Λ with the thermal bath. As illustrated in
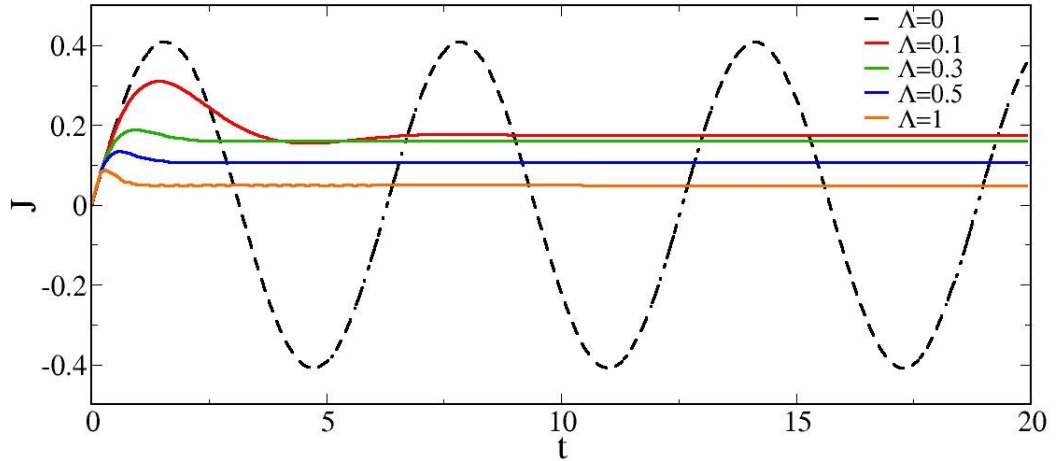
FIGURE 2.10. Time evolution of the local current density $\mathbf{J}(t)$, at different values of coupling Λ. The black dashed line is a Bloch oscillation, obtained in the completely coherent regime. When $\Lambda \neq 0$, Bloch oscillations are damped, and the system relaxes to a NESS.

Figure 2.10, the application of a DC field on a periodic lattice structure gives rise to very different results in terms of current density $\mathbf{J}(t)$, according to the coupling Λ with the thermostat. First of all, the dashed line represents the current density obtained in the system at $\Lambda = 0$. As we expected, an oscillating current (Bloch oscillations) is recovered, because of the total lack of scattering mechanism in the system. The introduction of a non-vanishing coupling Λ with the external bath suppresses the Bloch oscillations [23], leading the local current density $\mathbf{J}(t)$ to relax to a finite value, corresponding to the formation of NESS.

As visible in Figure 2.10, the current density initially follows the trend of the dashed line, and then is damped by the coupling with the bath, and saturates at a finite value in a non-linear way. This damping and the subsequent saturation process take place on different time scales [22], according to the strength of the coupling with the bath. In fact, the higher is the coupling Λ with the external bath, the higher is the damping of the Bloch oscillations. This phenomenon can be explained recalling the meaning of the coupling Λ: as it is increased, the scattering of the conduction electrons is increased, the system becomes less and less coherent and the Bloch oscillations are damped faster. Therefore, the relaxation time required to reach the NESS decreases with increasing coupling to the external bath.

If $\Lambda = 0$, the system will be in a perfectly coherent state and no NESS will be created,

on the contrary, for the largest investigated coupling ($\Lambda = 1$) only a few time units are required for the system to relax. The approach to the NESS is independent on
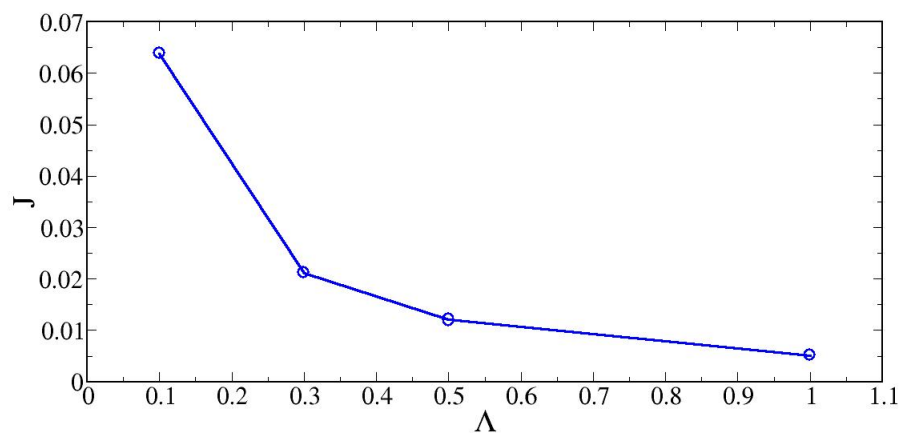

FIGURE 2.11. NESS current **J** vs coupling Λ. As Λ is increased, the scattering time τ in the system decreases, and the NESS current value becomes lower.
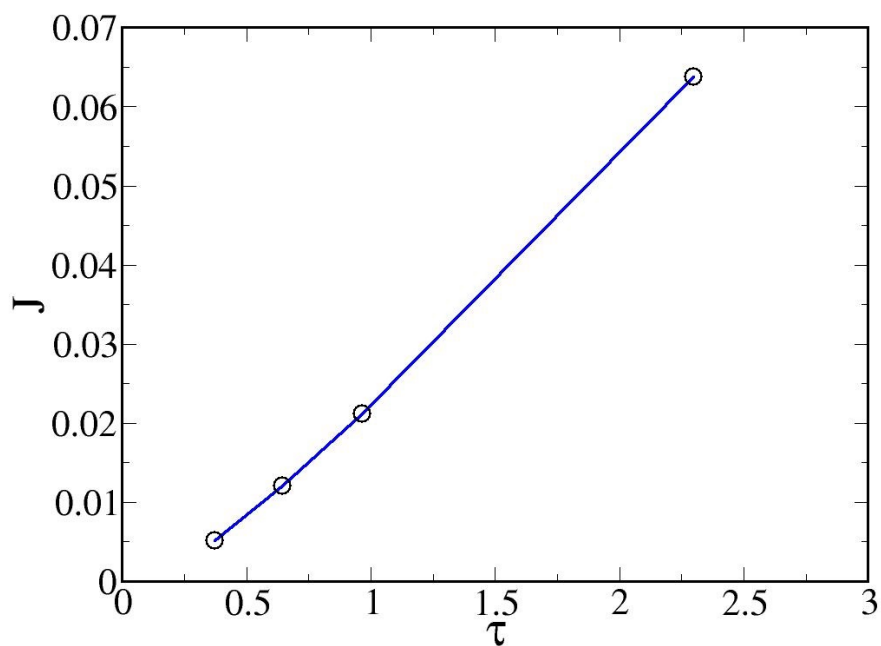

FIGURE 2.12. Steady-state current **J** vs scattering time τ of the system. The relation, similarly to the Drude model case, is linear.

the initial conditions, confirming that the non-equilibrium physics is governed by the field **E** and the dissipation term Λ. In the end of this section, we want to establish a relation between the value of the NESS current density and the coupling with

the external bath Λ. We apply to our tight-binding system a DC field of intensity $\mathbf{E} = 0.1$, and extrapolate the finite-current values of NESS at different values of Λ, as illustrated in Figure 2.11. As we expected, we find out a decreasing behaviour of $\mathbf{J}$ vs the coupling Λ, that can be easily explained. In fact, if Λ in the system is higher, there will be more electronic scattering in the system (τ will be lower), and the electric transport will be weakened.

Using the conversion between Λ and τ obtained before, one can represent the steady-state current $\mathbf{J}$ vs the scattering time τ (Figure 2.12). The relation between the steady-state current and the scattering time (at constant electric field) is linear, as in the Drude model, where:

$$(2.66) \qquad \mathbf{J} = \frac{e^2 n \mathbf{E}}{m} \tau$$

This linearity is caused by the low applied electric field $\mathbf{E}$, condition under which (2.66) is derived. In the next chapter, we will investigate non-linear effects in correlated systems, caused by the coupling with high electric fields.

CHAPTER 3

High electric fields effects

In this chapter, we investigate the effects of large electric fields on a periodic system. We provide a description of the Wannier-Stark localization and of the positive-negative resistivity crossover, both caused by the application of high electric fields. We then introduce the effect of the dimensional crossover, that consists in a dimensional reduction of a non-equilibrium system coupled with a large electromagnetic field, that makes the system behave as an equilibrium one, in lower dimensions.

1. The Wannier-Stark localization

In the previous chapter, we obtained that in a fully coherent system without any type of scattering ($\Lambda = 0$), one observes an oscillating response to an applied DC electric field, with oscillations at the Bloch frequency ω_B.

In order to experimentally observe Bloch oscillations of frequency ω_B in a real solid, we must require $T_B \ll \tau$, so that the electrons may complete several Bloch oscillations before scattering events take place. Looking at (2.32), one can reduce the Bloch oscillations period by increasing the electric field $\mathbf{E}$, which accelerates the electrons moving in the Brillouin zone. However, the application of a DC field of strength $\mathbf{E}$, makes the top and the bottom of the band tilt of a quantity $e\mathbf{E}x$. Strictly speaking, the application of an electric field breaks the translational symmetry of the system, so that the band structure scheme can at most be a pictorial initial approximation [24]. If one develops a full quantum mechanical treatment of electrons in a periodic potential under the influence of an electric field $\mathbf{E}$, one obtains the Wannier-Stark ladder [25], which shows that a strong electric field can localize electrons in a finite region of space, inducing an insulating behaviour in the solid.

In order to understand the nature of electronic states in a potential, given by the sum of the periodic potential $V(x)$ and a linearly varying potential $e\mathbf{E}x$, let us consider

the following stationary eigenvalues equation:

$$(3.1) \qquad \left[\frac{p^2}{2m} + V(x) + e\mathbf{E}x \right] \Psi(x) = E\Psi(x)$$

where $\Psi(x)$ is an eigenfunction of energy E. The role of a uniform electric field $\mathbf{E}$ in the one-band approximation is to replace itinerant crystalline states by a ladder of spaced bound levels. By making the translation $x \rightarrow (x - na)$, where n is an integer, we have that $\Psi(x - na)$ is also an eigenfunction of (3.1) with eigenvalue $E + e\mathbf{E}na$. Therefore, the solutions of the Schrödinger equation (3.1) form a discrete Wannier-Stark ladder of separation $\Delta E = e\mathbf{E}a$ between rungs, as illustrated in Figure 3.1. In very strong electric fields the difference of energy between adjacent sites
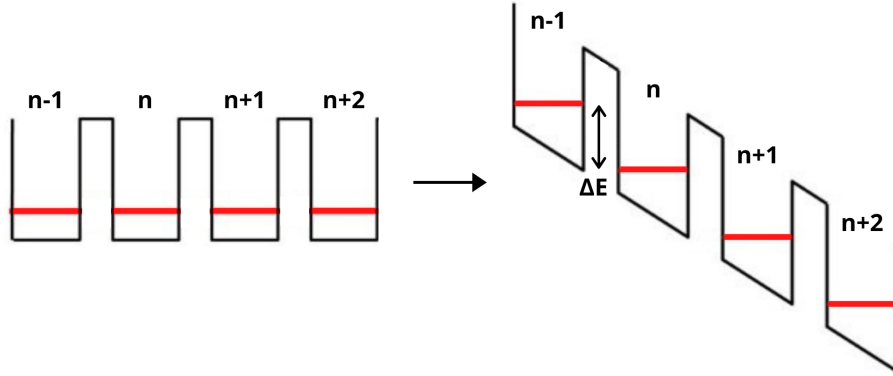

FIGURE 3.1. The Wannier-Stark ladder. The energy levels are split of a quantity $\Delta E = e\mathbf{E}a$, which is increased as long as $\mathbf{E}$ becomes higher. In the limit of very high electric field, the energy level are extremely separated, and the Wannier-Stark insulator arises.

exceeds the original width of the band, and $\Psi(x)$ becomes localized on the single site, giving birth to the Wannier-Stark dynamical localization. A picture of how this localization occurs can be given by considering each atomic site as a potential well. Imagine initially symmetric potential wells, made a little asymmetric by the application of an electric field $\mathbf{E}$. As long as the field $\mathbf{E}$ is increased, the potential wells tilt more and more, and the wavefunctions become more localized on the single site. Interestingly, when the electric field $\mathbf{E}$ is very high, the sites are strongly localized, and the hopping integral vanishes. In this situation, electrons can only travel hopping between localized sites, and their transport is promoted by the scattering Λ, which acts as a 'bridge' between localized Wannier-Stark states.

2. The positive-negative resistivity crossover

Having illustrated the formation of the NESS through the non-equilibrium dynamics of the system, and the creation of an insulating phase when a high electric field is applied, we now turn our attention to the response in terms of $\mathbf{J}$ of the system coupled to the thermal bath subjected to growing $\mathbf{E}$, at different couplings Λ and in the non-interacting limit $U = 0$.

In order to approach the problem, we compute the current density along the x direction $\mathbf{J}_x(t)$ of a given system subjected to a given electric field $\mathbf{E}_x$, choosing a number of total time-steps N_t that allows the relaxation of the system. Then, we extract the value of the steady-state current $\mathbf{J}_x$, and we plot it vs the applied electric field $\mathbf{E}_x$.

We repeat the entire process changing the coupling Λ with the external bath, always choosing values that allow us to see the formation of NESS. The results are shown in Figure 3.2. We find a linear-nonlinear crossover of $\mathbf{J}_x$ as a function of the electric
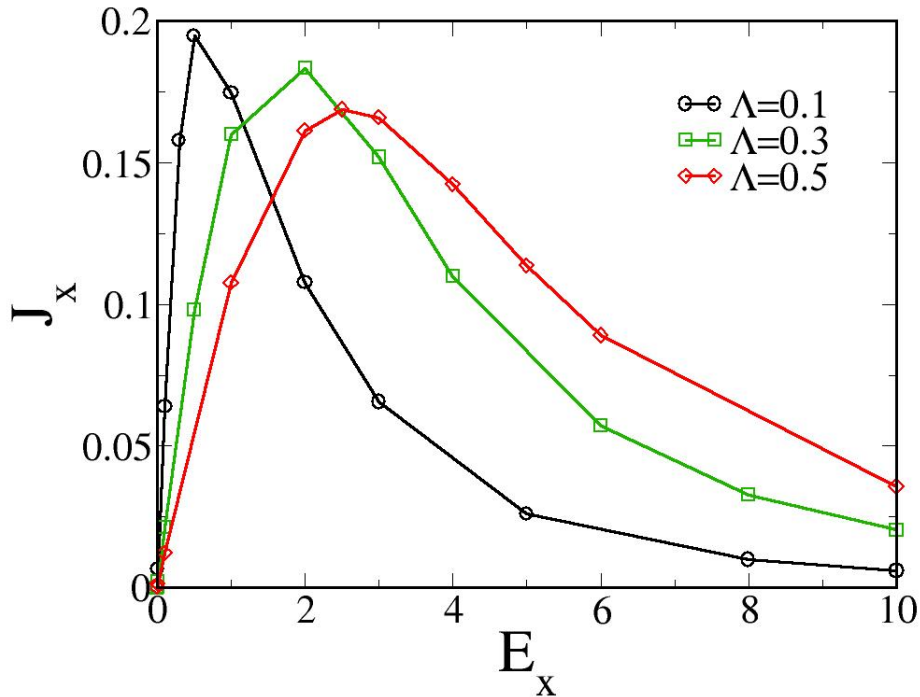

FIGURE 3.2. Steady-state current $\mathbf{J}_x$ vs electric field $\mathbf{E}_x$, varying the coupling Λ, at $U = 0$. At high electric field, the system experiences a positive-negative resistivity crossover.

field $\mathbf{E}_x$, for every value of Λ. In fact, increasing the electric field $\mathbf{E}_x$, the system

response starts to be non-linear; the steady-state current reaches a maximum before decreasing as the field is further increased. This last behaviour is caused by the Wannier-Stark localization [25]; as the field is further increased, the localized Wannier-Stark states are formed and the system becomes more insulating. As already said, the existence of a residual current at large values of the field is an effect due to the presence of the thermal bath, which allows conduction electrons to 'hop' between Wannier-Stark states.

Looking at the curves in Figure 3.2, the maximum height reduces increasing Λ, due to the rise of the scattering, and the maximum moves to higher electric fields, because when the system is strongly coupled with the bath, higher electric fields are needed to reach the Wannier-Stark insulator phase.

Moreover, keeping Λ fixed, one can observe that at very small electric fields the current $\mathbf{J}_x$ is linear with the field $\mathbf{E}_x$, as expected by continuity perturbing the equilibrium state. In this region of low fields, we attend the so called *linear regime*, where the response of the system is linear with the perturbation, as visible in Figure 3.3, a particular of Figure 3.2 for low electric fields. At low electric fields, the
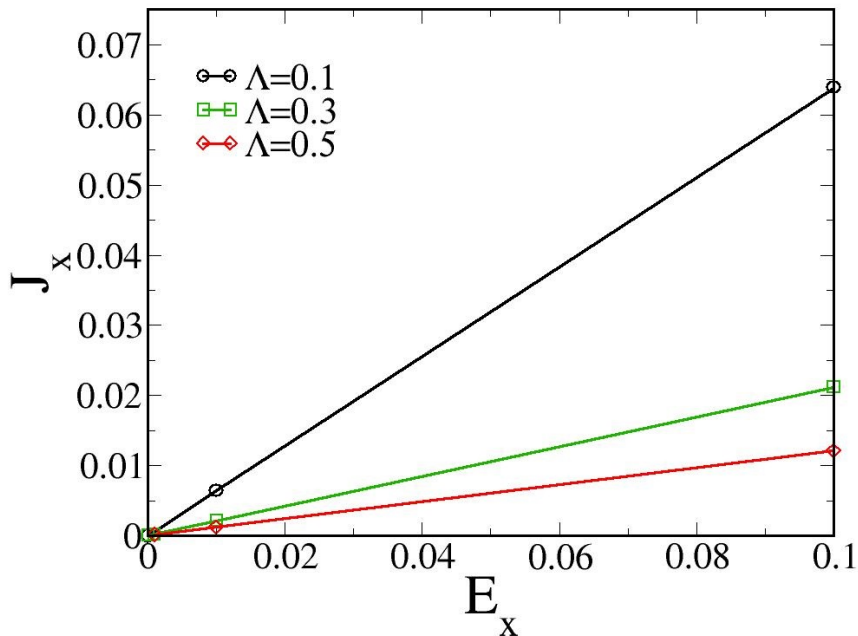

FIGURE 3.3. Particular of Figure 3.2. For electric fields lower than $\mathbf{E}_x = 0.1$, the linear regime holds, and the response to an external perturbation in terms of steady-state current is linear for all investigated couplings Λ.

steady-state current is linear in the applied field, according to $\mathbf{J}_x = \sigma_0 \mathbf{E}_x$, where σ_0 is the static conductivity. We find out that for electric fields lower than $\mathbf{E}_x = 0.1$, the linear regime holds, even in the case $\Lambda = 0.1$. By increasing the coupling Λ, the conductivity σ_0 in the linear regime of fields decreases, as we expected from the presence of more scattering, and the linear regime extends to higher fields.

2.1. Interaction U.

In this section, we investigate the effects of the Coulomb interaction U on the dynamics of the system, focusing on the formation of the NESS and investigating the dependence of the current density $\mathbf{J}(t)$ on the interaction strength.

We consider a bidimensional single-band Hubbard model on a square lattice of spacing a, at half-filling. The Hamiltonian of the system reads:

$$(3.2) \qquad H = \sum_{\mathbf{k}\sigma} \epsilon[\mathbf{k} - e\mathbf{A}(t)]c^{\dagger}_{\mathbf{k}\sigma}c_{\mathbf{k}\sigma} + U \sum_i n_{i,\uparrow}n_{i,\downarrow}$$

where $\mathbf{A}(t)$ is the internal vector potential, and U is the local Coulomb repulsion. This model describes interacting electrons with nearest-neighbour hopping t, whose amplitude is fixed $t = 1$ throughout our calculations, as unit of energy. The system is driven out-of-equilibrium by a DC field of strength $\mathbf{E}$, and it is coupled with an external thermal bath Λ. Moreover, the coupling with the external electromagnetic field is realized through the Peierls substitution, as in (2.47). The electric field $\mathbf{E}$ and the correlation U are switched on at the same time $t = 0$, representing the starting point of the non-equilibrium dynamics.

Once again, the establishment of a finite NESS current is possible, thanks to two different scattering processes. In addition to the thermal bath Λ, also the electronic interaction U can help the system to relax towards a NESS. However, the interaction U alone can not relax completely the system, that always needs a finite Λ to reach NESS. In fact, if $\Lambda = 0$, we find out that the steady-state current has to vanish at long time (if $U \neq 0$) or it has to average to zero (if $U = 0$), recovering the limit of completely coherent system and the Bloch oscillations.

When the system is coupled with an external electromagnetic field $\mathbf{E}$, this one is responsible for the heating of the system (and the consequent decoherence), due to the energy it injects in. For this reason, the system always needs a dissipation channel that provides degrees of freedom for its relaxation.

Actually, U is a new scattering channel, which provides a similar dynamics with respect to Λ. However, the two processes are physically very different: the Coulomb

interaction U involves two particles that interact exchanging energy and momentum, while the coupling with the thermal bath Λ is a quadratic hybridization of the system, a single-particle process that does not conserve momentum as well (which is the condition for dissipation).

Once again, we look at the formation of NESS, by computing the current density $\mathbf{J}(t)$ at fixed electric field $\mathbf{E} = 0.1$, keeping a small coupling $\Lambda = 0.016$, which provides dissipation, and varying the on-site Coulomb interaction U. We choose $\mathbf{E} = 0.1$ in order to stay in the linear regime of fields and eliminate all possible non-linear effect, while the choice of Λ is made trying to maximize the value of the steady-state current. The additional presence of U forces us to solve the problem at equilibrium firstly, and then use the equilibrium solution as initial guess for the non-equilibrium dynamics.

The parameters between the two algorithms have to be consistent. For this reason, we fix the inverse temperature $\beta = 10$ and the number of Matsubara frequencies $N_M = 8192$. The results are illustrated in Figure 3.4. One can clearly see that the
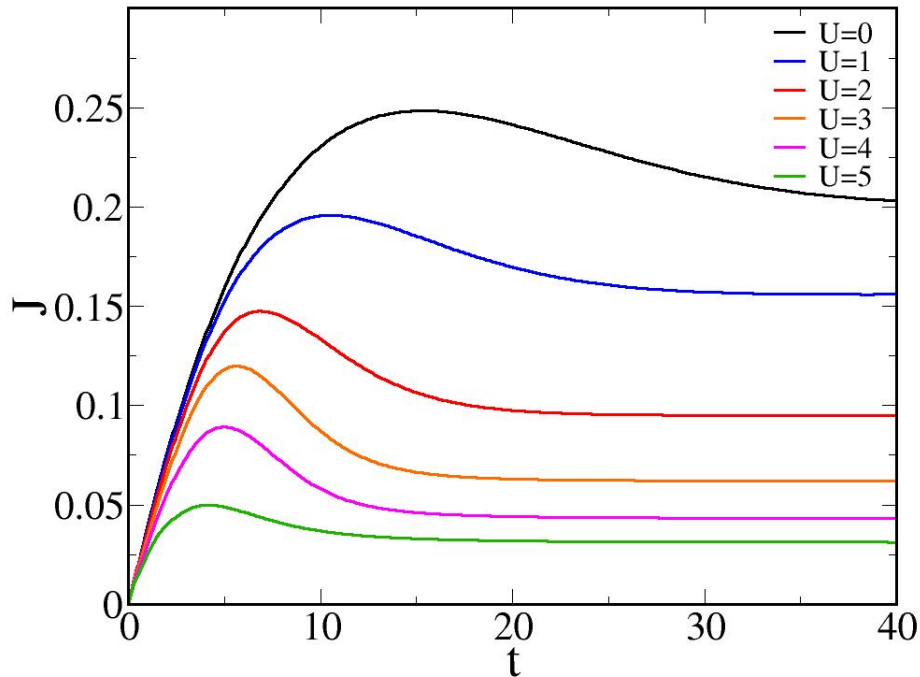

FIGURE 3.4. Time evolution of the local current density $\mathbf{J}(t)$, at fixed coupling Λ and electric field $\mathbf{E}$, varying the interaction U. Increasing the interaction U, the system accelerates its relaxation dynamics, and the final NESS current is lower.

presence of the on-site Coulomb interaction U helps the relaxation of the system towards a lower steady-state current [22]. In the absence of coupling to the external bath, the electron-electron interactions would suppress the Bloch oscillations, leading to an exponentially decaying current which converges to zero at very long times. Viceversa, when Λ is finite, the system becomes more and more incoherent as U is increased, and low-current NESS are formed. Looking at Figure 3.4, the initial current dynamics is the same for all values of U; while the interaction is increased, the steady-state current is damped, the more the higher is U. Looking at Figure 3.4, one can note how U is kept low, to preserve the half-filling. After having computed

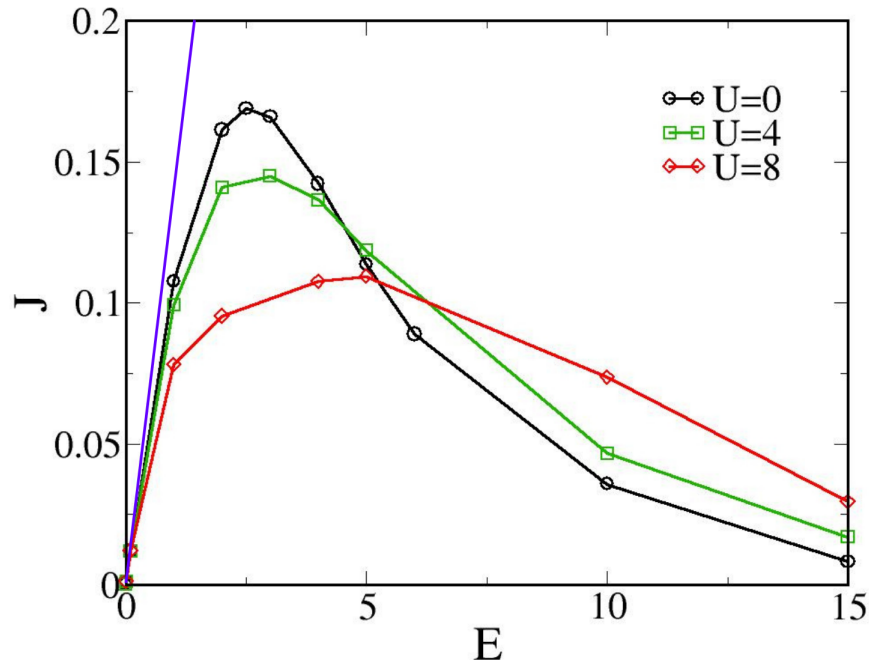
FIGURE 3.5. Evolution with the interaction U of the steady-state current $\mathbf{J}_x$ vs applied electric field $\mathbf{E}_x$, at fixed coupling $\Lambda = 0.5$. The presence of U shifts the maximum of the curve at higher fields, and lower its height. The blue line indicates the linear regime of fields, and its slope is the static conductivity, universal in U.

the current $\mathbf{J}_x(t)$ and observed the formation of NESS, in Figure 3.5 we represent the steady-state current values vs the applied electric field $\mathbf{E}_x$, where the current is collected in the same direction (x) of the applied field. We repeat the process at different values of interaction U, all at fixed coupling Λ. In order to succeed in increasing the interaction U, we choose $\Lambda = 0.5$, that allows the investigation of the correlated system until $U = 8$, by increasing the convergence radius of the IPT.

Looking at Figure 3.5, the $U = 0$ curve can be reduced to the situation in Figure 3.2, which shows a positive-negative resistivity crossover. Actually, the steady-state current shows the same behaviour for all values of the electronic interaction U. In fact, after going through a maximum, the current is exponentially damped at very strong fields. One more time, the maximum of the curve gets lower increasing U, because the correlation tends to localize the system and prevents electric transport. In the end, looking at very low electric fields, where the linear regime holds, one can see that the linear conductivity is independent on U; in fact, all the curves have the same initial slope (represented in Figure 3.5), and out of the linear regime they deviate the faster the higher is U. It can be shown [9] that, regardless of microscopic details (coupling Λ and interaction U), the static conductivity σ_0 in the linear regime is universal. In fact, the calculation for σ_0 has important contributions only from electrons near the Fermi surface (actually in a sharp region of width $k_B T$ around the Fermi level). Due to the Luttinger-Ward theorem, the spectral function can not vary with U at the Fermi level; for this reason, the static conductivity in the linear regime is independent on U.

3. The dimensional crossover

In this section, we want to better understand the effect of a strong electric field $\mathbf{E}$ on the dynamics of correlated systems, coupled with an external thermal bath. In particular, we focus our work on very strong DC fields, that can cause a phenomenon known as *dimensional crossover*[7][8].

This phenomenon consists of a dimensional reduction of the non-equilibrium system coupled with a strong electric field, that makes the system behaving as an equilibrium Hubbard model in lower dimensions. In fact, when the energy scale associated to the DC field is much larger than any other energy scale present in the system (including Λ), we observe a reduction of the dimensionality of the system. This phenomenon can be linked to the Bloch oscillations: when a large electric field $\mathbf{E}$ is applied along one direction of the bidimensional system (let us choose the x direction), the electrons start to oscillate along that direction. If the electric field $\mathbf{E}$ is strong enough, the period of Bloch oscillation, inversely proportional to the strength of the field, becomes lower than the thermalization time τ. In this particular situation, Bloch oscillations survive in the transient of time in which the system is relaxing, before being damped by the relaxation processes. This continued existence of Bloch

oscillations, due to the strong field $\mathbf{E}$, makes the hopping t to fall as $t/\mathbf{E}$ along the direction of the field, localizing the system. Ideally, one can imagine electrons moving so fast that they are stationary on average, causing a dynamical localization. Analytically [7][8], the explanation can be given by the form of the non-interacting retarded Green's function, defined as:

$$(3.3) \qquad G_0^R(\tau, k) = -i\ exp\left(i \int_{-\tau/2}^{\tau/2} d\tau' \epsilon(k - e\mathbf{E}\tau') - i\tau\Sigma_0^R\right)\theta(\tau)$$

According to (3.3), the Green's function depends on the time-integral of the dispersion $\epsilon(k - e\mathbf{E}\tau)$, which in turn depends on time τ through the minimal coupling with the field. If the electric field $\mathbf{E}$ is directed along the x direction, it couples with the k_x component through the minimal coupling. Thus, one can split the dispersion $\epsilon(k - e\mathbf{E}\tau)$ into two components, parallel and perpendicular to the field, as follows:

$$(3.4) \qquad \epsilon(k_x - e\mathbf{E}_x\tau + k_y) = -2t\left[cos(k_x - e\mathbf{E}_x\tau) + cos(k_y)\right]$$

In the limit of large $\mathbf{E}_x$, the time integral of the x-component of the dispersion averages to zero, because it is a strongly oscillating function. Thus, the free dispersion loses its dependence on k_x, by reducing the bidimensional problem to a one-dimensional one, as follows:

$$(3.5) \qquad \epsilon(k) = -2t\left[cosk_y\right]$$

As a consequence, the bandwidth of the system reduces from $8t$ (in the 2D case the bandwidth is within the range $[-4t, +4t]$) to $4t$ (in the 1D case the bandwidth is within the range $[-2t, +2t]$).

The dimensional crossover has also important consequences on the spectral features of the system; as the electric field $\mathbf{E}$ increases, the bidimensional spectral function $A(\omega)$ acquires typical one-dimensional features, developing symmetrical Van Hove singularities at the edges of the reduced band. In a typical one-dimensional equilibrium tight-binding system, Van Hove singularities are the features that occur in the DOS function at the k-point where the dispersion relation $\epsilon(k)$ has vanishing derivative.

Moreover, the dimensional crossover transforms a non-equilibrium problem in an equilibrium one of lower dimension. This fact can be observed by the distribution function $N(\omega)$, which evolves from a totally non-equilibrium function to its equilibrium version, the Fermi-Dirac distribution. In equilibrium, this is ensured by the fluctuation-dissipation theorem; out of equilibrium, this fact is no more true, and

the distribution function becomes a more complex function, that depends both on k_x and k_y (at least for low electric fields).

In the end, the dimensional crossover can be obtained only when the field has remarkable components along a specific direction. Actually, it would be possible to recover the atomic limit, when the dispersion loses both the dependence on k_x and k_y, also in the bidimensional lattice, simply by applying a strong electric field in the (x, y) direction.

4. Pulsed electric fields

In this section, we will briefly illustrate how an intense ultra-fast laser pulse can be modelled and used to drive correlated systems out-of-equilibrium. In the rest of our work, we will consider the laser pulse as an oscillating electric field of amplitude $\mathbf{E}$ convoluted with a Gaussian envelope, with the following form:

$$(3.6) \qquad \mathbf{E}_{pulse} = \mathbf{E} \ cos[\omega(t - t_0)] \ exp\left(-\frac{(t - t_0)^2}{\tau^2}\right)$$

where ω is the angular frequency of the oscillating field, t_0 is the centre of the Gaussian and $\tau = \sqrt{2}\sigma$, where σ is the standard deviation of the Gaussian envelope. A very useful quantity often used in optics to indicate the duration of a laser pulse, at which we will refer throughout all our work, is the Full Width at Half Maximum (FWHM), defined as $\tau_0 = 2\sqrt{2ln2}\sigma = 2\sqrt{ln2}\tau$.

In our work, we properly tune the parameters of the pulse signal (pump protocol) to get closer to a realistic situation. First of all, we choose $\omega = \pi$ (in the frequency unit (2.57)) as the oscillating field frequency, which gives to the photon an energy in the order of the Mott gap (see (2.58)), in order to use the laser pump to inject excitation in the system through the Mott gap itself.

Then, with reference to time units (2.55), we choose the FWHM $\tau_0 = 8$ ($\sim 10fs$), that combined with the frequency allows to have about 4 optical cycles inside the Gaussian envelope ($N_{cycles} = \tau\nu$).

We set the centre of the pulse at $t_0 = 11$, in order to position the tail of the Gaussian envelope at $t = 0$. In this way, the pulse affects the dynamics of the system from the very beginning of the simulation.

The choice of the pulse parameters plays a key role in our work: each time the pulse signal is present in our calculation, we compare its time scale with the thermalization time τ given by the coupling Λ with the external bath, necessary for the current

transport. This comparison, and the interplay between the two time scales, are crucial for the understanding of the dynamics of the system.

In fact, it is conceptually very different if the system is hit by the laser pulse before, during or after its coupling process with the thermal bath. Generally speaking, we identify three different cases, distinguished by the relation between the two time scales:

- We deal with the *completely coherent limit* when the pulse dynamics is very short with respect to the coupling dynamics; in this case the laser pulse hits a totally decoupled system, which still has all its coherence properties;

- The second and opposite limit is the *completely incoherent limit*, when the laser pulse hits a completely coupled system, that has already reached its thermal equilibrium;

- In the end, the *intermediate regime*, when the system is hit by the laser pulse during its coupling with the thermal bath.

Actually, this last case is also the most physically interesting, because it allows to exploit the coherence effects of the system. In fact, as long as the system has not thermalized with the bath, the quasi-particles are not completely incoherent, and coherent transport could be achieved. For this reason, in the next chapter we will always tune the value Λ of the thermal coupling looking at the pulse time scale, according to the desired dynamics.

CHAPTER 4

Superposition of DC and pulse fields on a correlated metal

In this chapter, we study the effects of DC and pulse fields on differently correlated systems. We want to prove that our system undergoes a dimensional crossover when a strong electric field is applied on it, and show why our bidimensional out-of-equilibrium system reduces to an one-dimensional effective one in equilibrium.

In order to do that, we solve the NEQ-DMFT equations with the usual IPT impurity solver. We analyse several physical quantities, such as the electric current $\mathbf{J}(t)$, the spectral function $A(\omega)$, the occupation function $N(\omega)$ and the distribution function $F(\omega)$, to support our thesis. The resulting dimensional reduction of our bidimensional square lattice system has brought us to think to the importance of dimensionality in correlated systems, feature that can influence all their properties and physical observables.

We will concentrate on the current flowing in the system in a particular direction (we take the y axis) under the effect of a probe DC field in the linear regime, when a carrier DC field or pulse field is applied, both in the same direction and in the orthogonal one with respect to the probe field. Consequently, we will analyse a total of four different cases: when the carrier DC or pulse field is parallel to the probe field and when it is orthogonal to it. We will demonstrate how the application of large fields on a particular direction of the lattice can induce a dynamical localization in the same direction, reducing the dimensionality of the system itself.

Moreover, we prove that the direction of collection of the current has a crucial importance for the understanding of the system dynamics. Throughout all this chapter, we will consider a bidimensional single-band Hubbard model on a square lattice (we will use x and y axes to indicate the two main directions) with nearest neighbour hopping, with dispersion:

$$\epsilon(k) = -2t \left[cos(k_x a) + cos(k_y a) \right]$$

(4.1)

where a is the lattice constant.

All the simulations are carried on both in the metal phase ($U = 0$) and in the correlated metal phase, with intermediate values of interaction ($U \neq 0$). The maximum of these values is chosen according to the strength of the coupling Λ, which helps the IPT method to work at higher correlations U.

1. Parallel fields

1.1. Parallel DC-DC.

In this first section, we investigate the case of two DC fields applied on the system in the same x direction. We choose to work at coupling $\Lambda = 0.3$, with an associated thermalization time $\tau \sim 0.94$, in order to obtain a stable steady-state current in a quite brief time window.

We investigate the dependence of the steady-state current (collected along the x direction as well) vs the applied field $\mathbf{E}_x$. Even in this simplified situation, we distinguish two different DC fields: the carrier field, which determines the dynamics of the system and eventually leads the dimensional crossover, and the probe field, which is in the linear regime (in order to eliminate non-linear effects) and is used to measure the current and to obtain information about the conductivity of the system (For $\Lambda = 0.3$, the linear regime of fields extends until $\mathbf{E}_x = 0.1$). This important distinction is redundant in this simplified case, but it will be crucial in the following sections. We will always take the probe field fixed, varying the carrier field, always measuring the current in the probe field direction. In this particularly simplified situation, of course we collect the final steady-state current in the x direction, where both the fields are orientated.

Actually, one can reduce this situation to the already faced case of a single DC field acting on a particular direction of the system. In Figure 4.1, we reported the behaviour of the difference $\mathbf{J}_x(t)$ between the steady-state current obtained with the superposition of the fields with the one obtained with only the probe field, vs the carrier DC field $\mathbf{E}_x$, at different values of interaction U.

We choose the probe field $\mathbf{E}_{probe} = 0.01$, completely in the linear regime. As already described, the establishment of a finite steady-state current is made possible by the combination of the scattering processes caused by Λ and U. From Figure 4.1, one can observe that for all values of U, the steady-state current is first linear with the field intensity, and after going through a maximum, is exponentially damped at very strong fields.
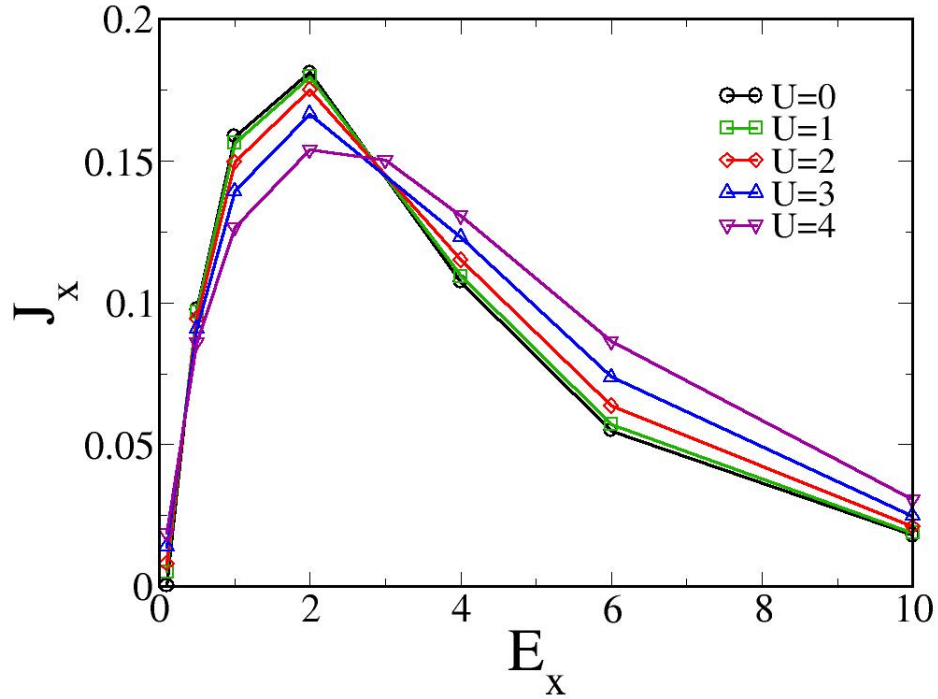
FIGURE 4.1. Net steady-state current $\mathbf{J}_x$ vs DC field $\mathbf{E}_x$, at different values of interaction U. For all values of U, the steady-state current is first linear with the field intensity and exponentially damped at very strong fields.

These results confirm the calculations made in the third chapter, where the damping of the steady state current was interpreted as an effect caused by the Wannier-Stark localization. This damping can be interpreted also as the effect of a dimensional crossover occurring at very strong fields. In fact, the increasing carrier field on the x axis tends to localize the system in the same direction, preventing the flowing of electric current along the x axis.

1.2. Parallel DC-PULSE.

In this second section, we consider the same system coupled with two different types of external electromagnetic fields: a DC field used as a probe and an oscillating pulse field, both orientated in the same x direction. Once again, we choose to work at coupling $\Lambda = 0.3$, with a thermalization time $\tau = 0.94$, in order to obtain a stable steady-state current in a quite brief time window. Comparing this scattering time with the pulse time scale (the pulse signal is centred at $t_0 = 11$), we find out we are in the completely incoherent regime, in which the pulse impinges on a system that is already thermalized with the bath.

We superimpose the two electric fields in order to simulate the injection of free charges in the system by the pulse field, and their transport by the DC probe $\mathbf{E}_{probe}$ = 0.1 (still in the linear regime).

In order to evaluate the effect of the superposition of the DC and the pulse fields on the system, we systematically make three different simulations for each different value of interaction U: we simulate the DC+PULSE case, where both the fields impinge at the same time on the system, the DC case and the pulse case, where only the static and the pulse field act on the system, respectively.

In order to isolate the net effect caused by the superposition of the two fields, we operate the difference between the DC+PULSE case, the DC and the pulse cases, relying on the linear regime of the probe. Of course, being the pulse field a transient signal, this difference is limited in time, and the current can not be evaluated from the long-time stationary states. For this reason, we operate the time integral of the difference-curve, which represents the difference of total charge flowing in the system in the two cases. In the upper panels of Figure 4.2, we illustrate the three

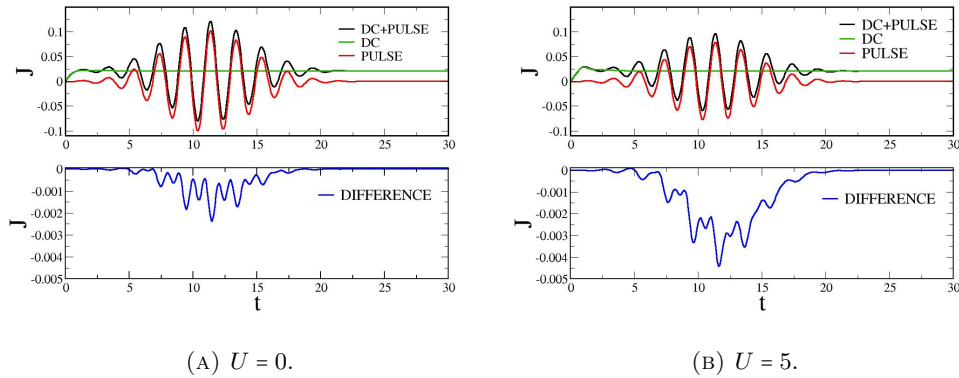(A) $U = 0$.   (B) $U = 5$.

FIGURE 4.2. *Upper panels.* Current $\mathbf{J}(t)$ flowing in the system with superposition of DC+PULSE pulse field, and with the two fields taken separately. *Lower panels.* Difference curve between DC+PULSE case and DC and PULSE taken separately.

simulations done both for $U = 0$ (Fig. 4.2 (A)) and $U = 5$ (Fig. 4.2 (B)), while in the lower panels the difference-curve is represented. We choose DC field of amplitude $\mathbf{E}$ = 0.1 and pulse field of amplitude $\mathbf{E}_{pulse}$ = 1. In both panels of Figure 4.2, the difference-curve starts from zero, develops a negative structure corresponding to the pulse, and vanishes again, regardless of the value of U.

In order to understand better this phenomenon, as the interaction U is varied, we

plot in Figure 4.3 the values of the flowing charge ΔQ (obtained integrating in time the difference-curve) vs U, again with $\Lambda = 0.3$. Looking at Figure 4.3, we
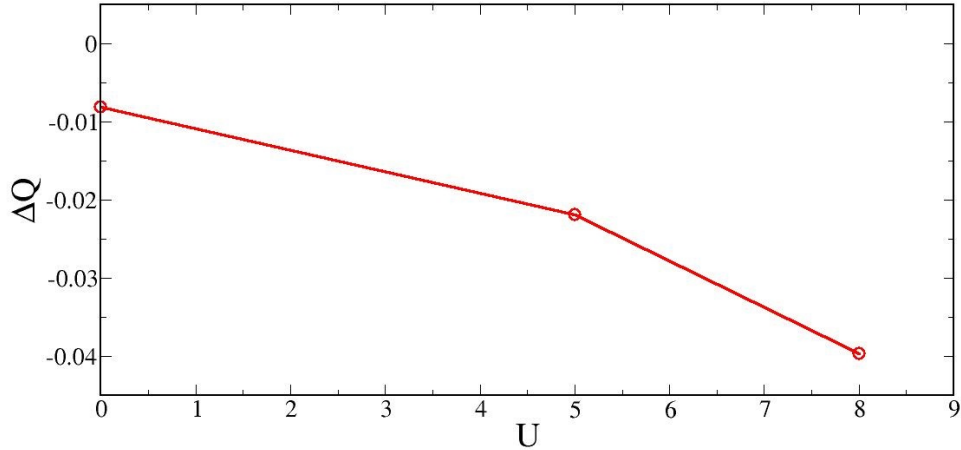

FIGURE 4.3. Flowing charge ΔQ (integral of the difference-curve) vs the interaction U, at $\Lambda = 0.3$. As U is increased, the conduction due to the superposition of DC+PULSE becomes always worse with respect to the single cases DC and pulse, taken separately.

find that the time-integral of the difference-curve between the DC+PULSE case and the single DC and pulse cases has an always decreasing behaviour with the interaction U, for all values of Λ tested ($\Lambda = 0.1$, 0.3, 0.5, 1.0). For this reason, as the interaction U is increased (both in the metallic and in the correlated metal phase), the DC+PULSE flowing charge becomes always worse with respect to the sum of DC and pulse flowing charges, taken separately. These results are consistent with the dimensional crossover we have already introduced: when the system is subjected to the DC+PULSE field, it experiences a bigger 'effective' field, and it is dynamically more localized, preventing the charge flowing.

Hence, the superposition of the two fields worsens the conduction of the system, with respect to the cases of single fields separately. Moreover, the inclusion of interaction U induces an even stronger localization with respect to the non-correlated case. Increasing U from a non-correlated system, the system coupled with the DC+PULSE field conducts even worse, until the insulating phase is reached, and the superposition of the two fields can generate free charge transport.

2. Perpendicular fields

In the previous section, we observed that an applied large field $\mathbf{E}$ induces a dimensional crossover in the system, that localizes along the direction of the field and reduces to a lower dimensional system, in the orthogonal direction with respect to the field. For example, a bidimensional system subjected to a strong electric field behaves as a one dimensional system in the orthogonal direction. For this reason, if a strong electric field is coupled with a bidimensional system, this last one can seriously change its geometrical properties, and the electric transport along x or y direction can be deeply different.

In the next sections, we will investigate a bidimensional single-band Hubbard model on a square lattice, coupled with two different electric fields, one orthogonal with the other. First of all, we take a DC field as a probe (in the linear regime of fields) along the y direction of the lattice, used to give information about the conductivity of the system. Along the other x direction, we set the carrier field (DC or pulse), responsible for driving the dimensional crossover.

Of course, the directions of fields become crucial, and their perpendicularity is the key to obtain an excess of current in the probe direction when they are superimposed, with respect to the single probe field situation. We always collect the final current along the y direction, where the probe field is orientated. In the next two sections, we will provide an evidence for the dimensional crossover, caused not only by the DC field [7][8], but also by the pulse field. We will analyse deeply the flowing current and the spectral properties of our system, such as the spectral function, distribution and occupation functions and the Fermi surface evolution.

2.1. Perpendicular DC-DC.

In this section, we investigate the case of two perpendicular DC fields applied on the system, one as a probe in the y direction, and the other as a carrier field in the x direction. We choose to work at $\Lambda = 0.3$, in order to obtain a stable steady-state current in a quite brief time window. We look at the conductivity of the system, measuring the steady-state current $\mathbf{J}_y$ vs the applied carrier field $\mathbf{E}_x$.

In the linear regime, the conductivity tensor is diagonal [17][26], and no $\mathbf{J}_y$ can derive from $\mathbf{E}_x$, or viceversa. Out of the linear regime, when strong fields are applied on the system, the conductivity can be represented as a 2×2 matrix, whose diagonal element are not vanishing. This is the reason why the current measured along the

y axis can depend on the electric field applied along the x direction, and viceversa. We take $\mathbf{E}_y = 0.01$ as the probe field, varying the carrier field $\mathbf{E}_x$. For each value of the carrier field, we measure the value of the steady-state current flowing in the y direction. We repeat the entire process for several values of the carrier field, both at $U = 0$ and at finite values of U (allowed by the coupling Λ), always keeping the probe field constant. The results are reported in Figure 4.4. The behaviour of the
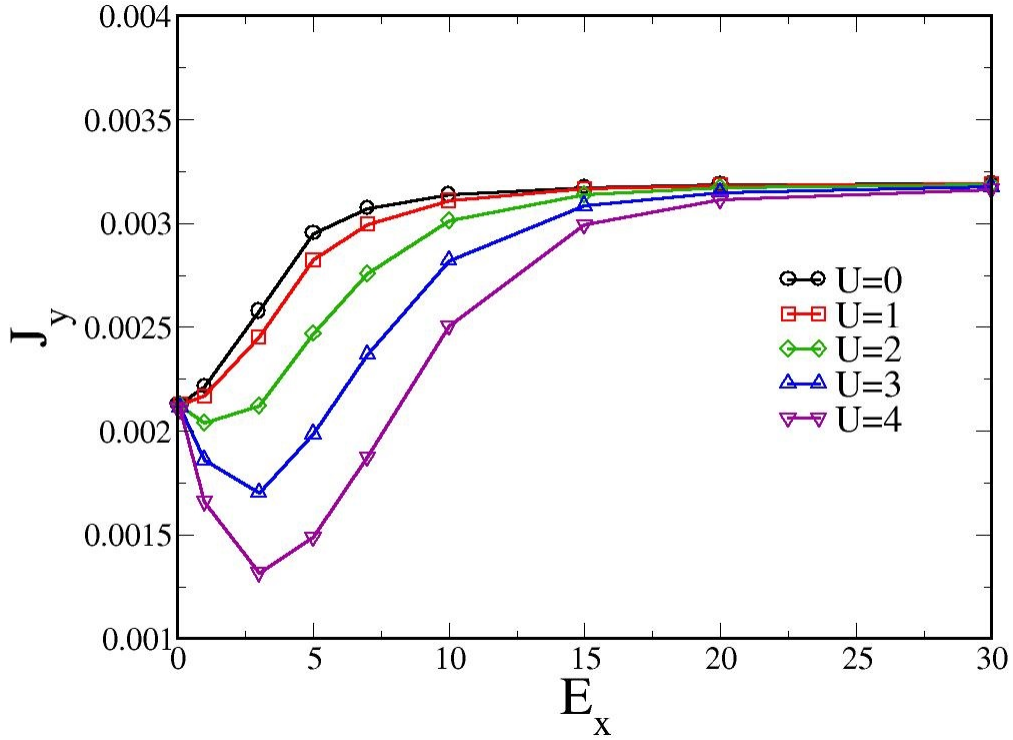

FIGURE 4.4. Flowing current $\mathbf{J}_y$ vs DC field $\mathbf{E}_x$, at different values of U. The value at $\mathbf{E}_x = 0$ is universal in U, because the probe field lays in the linear regime. Increasing $\mathbf{E}_x$, the dynamical localization effect competes with the localization provides by the interaction U, resulting in different behaviours of the $\mathbf{J}_y$ vs $\mathbf{E}_x$ curves, according to the value of U. However, at large electric fields, an asymptotic maximum is reached, when the system is completely one-dimensional due to the effects of the dimensional crossover.

curves, both at $U = 0$ and $U \neq 0$, can be explained with the help of the dimensional crossover, also looking at the spectral function, distribution and occupation function of the system. Let us first concentrate on the $U = 0$ curve in Figure 4.4. When the carrier field $\mathbf{E}_x$ vanishes, $\mathbf{J}_y$ is simply determined by the probe field, and it is

universal in U. We find that its value in zero is consistent with the one obtained in the previous chapter, when the system was coupled with only one DC field, directed in the same direction along which the current was measured. When the carrier field $\mathbf{E}_x$ starts to increase, the current increases too, until an asymptotic maximum value is reached, which is also universal in U.
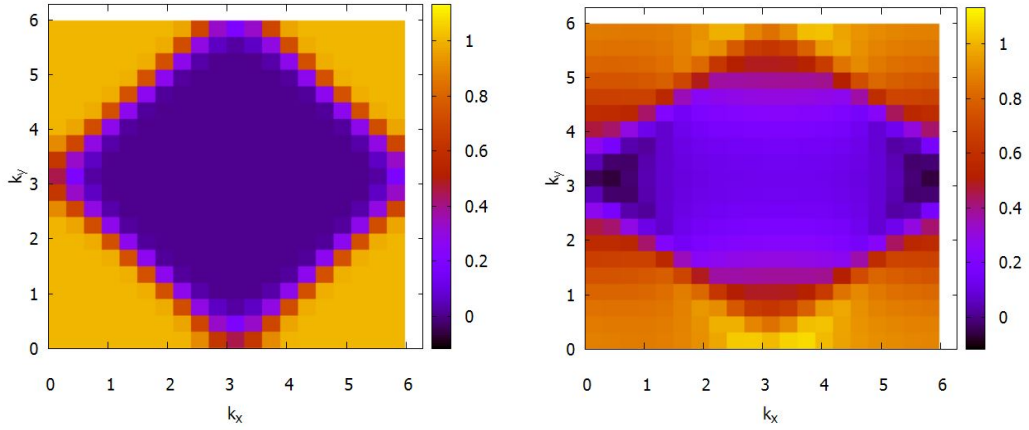
(A) *Fermi surface at t = 0 (initial time).*

(B) *Fermi surface at t = 1 (during the coupling with the external bath).*
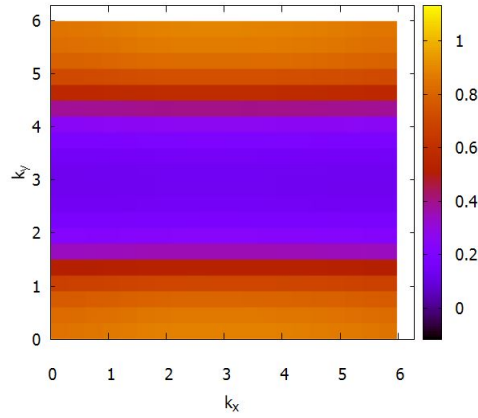
(C) *Fermi surface at t = 20 (when the system is completely thermalized).*

FIGURE 4.5. Time evolution of the Fermi surface of a system driven by a DC field ($\mathbf{E}_x = 30$). Because of the large DC field, the Fermi surface after the system has thermalized is completely one-dimensional, losing the dependence on k_x.

This current asymptote indicates that at very high carrier fields, $\mathbf{J}_y$ becomes independent on $\mathbf{E}_x$, because the system has completely experienced the dimensional crossover, and it has become completely one-dimensional in the y direction. To support our idea of the dimensional reduction, we provide a first evidence of the DC driven dimensional crossover. In Figures 4.5, we plot the evolution in time (for $t = 0, 1, 20$) of the Fermi surface, which represents the locus of momentum space points that divides occupied and unoccupied electronic states. We choose these specific instants of time in order to represent respectively the initial Fermi surface, its middle-time evolution and its final shape, when the system is totally thermalized (the thermalization time is $\tau \sim 0.94$, coupled to $\Lambda = 0.3$). Conventionally, we define the Brillouin zone in the range $[0, 2\pi]$, and we plot the evolution of the Fermi surface of the system driven by a field $\mathbf{E}_x = 30$, in the non-interacting case $U = 0$.

From Figure 4.5, we observe that the large applied DC field deeply modifies in time the shape of the Fermi surface, that starts to become k_x-independent, assuming a one-dimensional shape (completely invariant under k_x translations) when the system is totally thermalized. This modification has to be imputed to the strong carrier DC field, which makes the dispersion k_x-independent, reducing the system dimensionality.

Continuing looking at the evolution of the $U = 0$ curve, we note that the rise of the flowing current $\mathbf{J}_y$ is caused by the effects of the dimensional crossover, simply because the probe field is fixed, as well as the y-dispersion and the coupling Λ. A possible explanation of that, is that the localization of the system, led by the carrier field, increases the charge carrier density near the Fermi level, and therefore the electric current. In order to prove this, we study the evolution of the non-equilibrium spectral quantities of the system, when this last one is subjected to a DC carrier field $\mathbf{E}_x$ that drives it out-of-equilibrium.

First of all, we focus our attention on the non-equilibrium spectral function $A(\omega, t_{av})$ of the system, evaluated at $t_{av} = 20$, when the system is completely thermalized and NESS is formed. The results, obtained for different values of the carrier DC field (1, 3, 7, 30) in the $U = 0$ case, are reported in Figure 4.6. We choose these particular $\mathbf{E}_x$ values in order to focus on the critical points of Figure 4.4, where the interplay between the strength of the carrier field and the interaction U induces different behaviours of the $\mathbf{J}_y$ vs $\mathbf{E}_x$ curves.

First of all, we note that the spectral function $A(\omega)$ is always positive, as in the
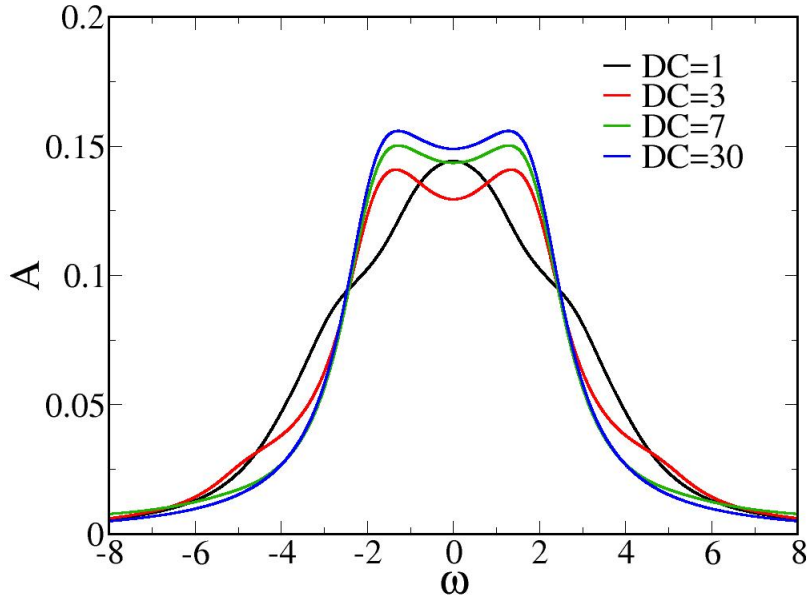
FIGURE 4.6. Evolution with DC field of the non-equilibrium spectral function $A(\omega, t_{av})$, evaluated at $t_{av} = 20$, in the $U = 0$ case. Increasing the electric field, the spectral function of the system acquires typical one-dimensional features, developing symmetrical Van Hove singularities at the edges of the reduced band $[-2, +2]$.

equilibrium case, even if it is not renormalized, and it does not describe a distribution probability. As we expected, the dimensional crossover deeply affects the spectral function of the system; as the electric field $\mathbf{E}_x$ increases, the bidimensional spectral function $A(\omega)$ acquires typical one-dimensional features, developing symmetrical Van Hove singularities at the edges of the reduced band.

In order to understand even better the effect of the increasing carrier field on the flowing current in the system at $U = 0$, we plot the evolution with the carrier field of the occupation function $N(\omega, t_{av})$ and the distribution function $F(\omega, t_{av})$, both evaluated at $t_{av} = 20$. We choose again the same values for the DC carrier field (1, 3, 7, 30). Figures from 4.7a to 4.7d represent the evolution with the DC carrier field of the occupation function $N(\omega)$, which gives information about the electronic occupied states, and the non-equilibrium distribution function $F(\omega)$, which replaces the equilibrium Fermi-Dirac distribution. For graphical reasons, the distribution function was rescaled by a factor 10. Figure 4.7 highlights that the rise of the DC carrier field affects deeply the distribution function $F(\omega)$, and consequently the occupation function $N(\omega)$.
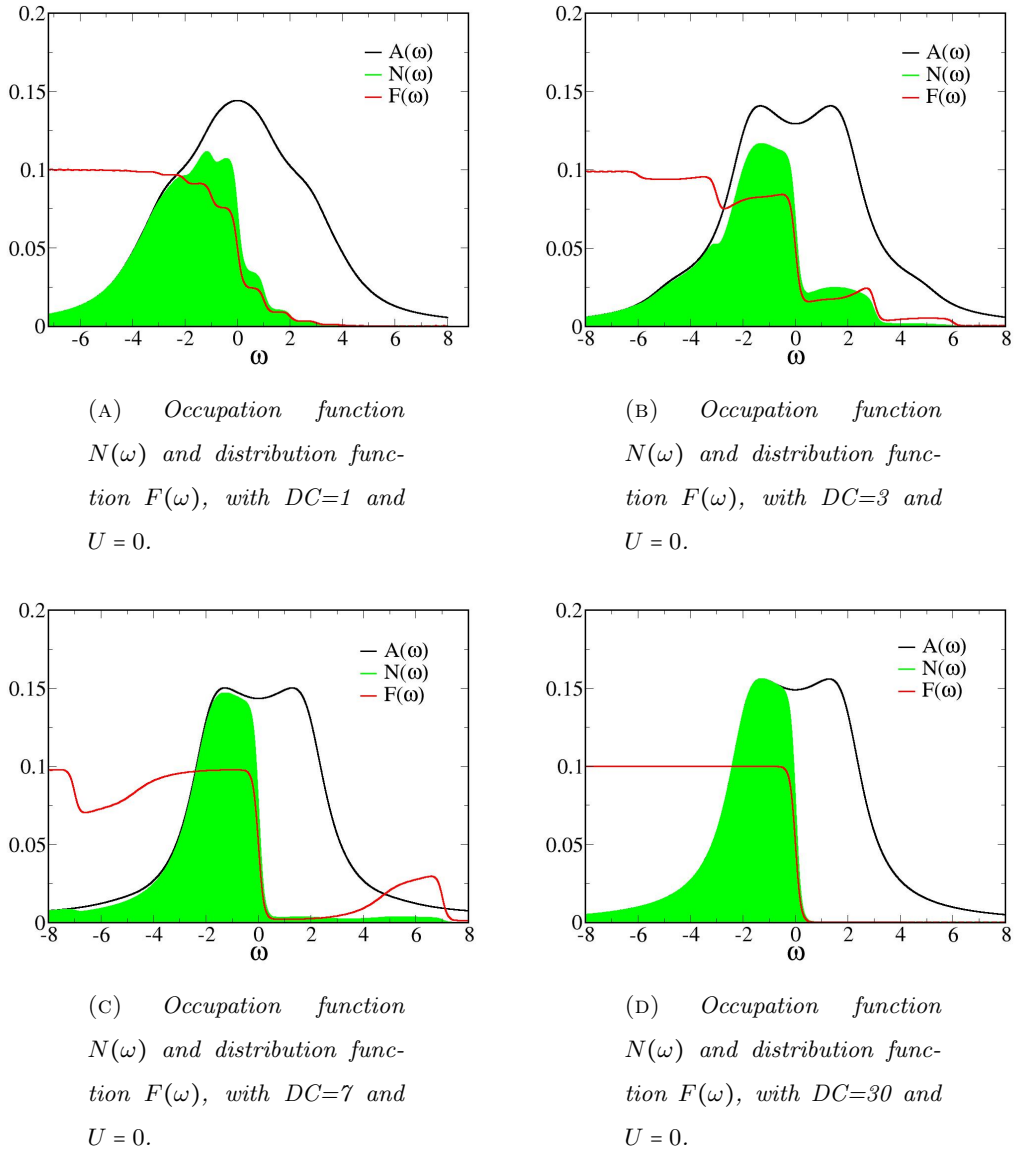
(A) *Occupation function $N(\omega)$ and distribution function $F(\omega)$, with DC=1 and $U = 0$.*

(B) *Occupation function $N(\omega)$ and distribution function $F(\omega)$, with DC=3 and $U = 0$.*

(C) *Occupation function $N(\omega)$ and distribution function $F(\omega)$, with DC=7 and $U = 0$.*

(D) *Occupation function $N(\omega)$ and distribution function $F(\omega)$, with DC=30 and $U = 0$.*

FIGURE 4.7. Out-of-equilibrium spectral functions, distribution functions and occupation functions of the $U = 0$ system subjected to different DC carrier fields. Increasing the DC field, the distribution function approaches the Fermi-Dirac function, the equilibrium distribution. The resulting occupation (at high DC fields) traces the equilibrium one at finite temperature, with occupied electronic states below the Fermi level and unoccupied electronic states above it. This behaviour confirms the DC-driven dimensional crossover, which drives the system in equilibrium.

Moreover, the occupation function $N(\omega)$, given by the product between the distribution function and the spectral function, is represented. It shows how the electronic excitations in the system are distributed in energy. At low electric field, the system has significant portions of spectral weight placed at high energy; increasing the carrier DC field, the system relaxes to equilibrium, until at large electric fields the occupation function $N(\omega)$ shows totally occupied states below the Fermi level and unoccupied states above it. This occupation reflects the Fermi-Dirac function at finite temperature T.

Looking again at Figure 4.4, the behaviour of the curves at finite U is quite different from the non-interacting case. In fact, we identify a first region (placed at low values of carrier electric field) where the current decreases by increasing the carrier field, followed by a minimum and a subsequent increase up to the asymptotic maximum. The universality in U of the current asymptote confirms that the conductivity in the linear regime of fields does not depend on U, as already noted. However, the presence of interaction U modifies the way one arrives to the dimensional crossover, although not the dimensional crossover itself. At low electric fields, the system, still
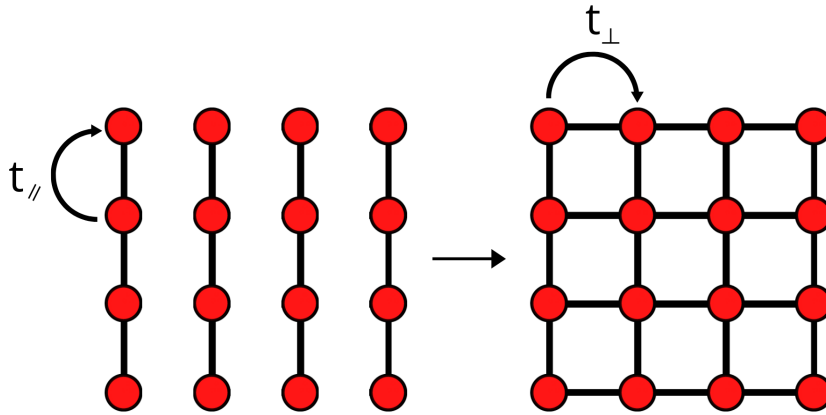

FIGURE 4.8. Schematic representation of our 2D system as a collection of 1D chains with parallel hopping $t_\parallel$, subjected to a transverse hopping $t_\perp = t_\parallel$, that makes the system bidimensional. If $t_\perp = 0$, the system remains one-dimensional.

maintaining its bidimensional features, starts to interpolate between a 2D and 1D system. To visualize it, let us image our system as a collection of 1D chains with transverse hopping $t_\perp$, such that if $t_\perp = 0$ the system is one-dimensional, while if $t_\perp = t_\parallel$ the system is bidimensional, as represented in Figure 4.8. In this context,

we interpret the decreasing of the current at low fields (when $U \neq 0$) as a hopping renormalization induced by the interaction U, which increases as long as the carrier field is increased. From that point, the non monotonous behaviour of the current is the marker of the dimensional crossover, which depends on the carrier field, but it is also affected by the interaction U. In other words, we have to remember that the dimensional crossover is a dynamical localization effect, that happens at higher carrier fields the higher is U, because the electrons are more localized and resist more the movement.

In order to prove this fact, we study the evolution of the non-equilibrium spectral function $A(\omega, t_{av})$ of the system, when this last one is subjected to a DC carrier field $\mathbf{E}_x$ that drives it out-of-equilibrium. We evaluate it at $t_{av} = 20$, when the system is completely thermalized with the thermal bath ($\Lambda = 0.3$). The results, obtained for
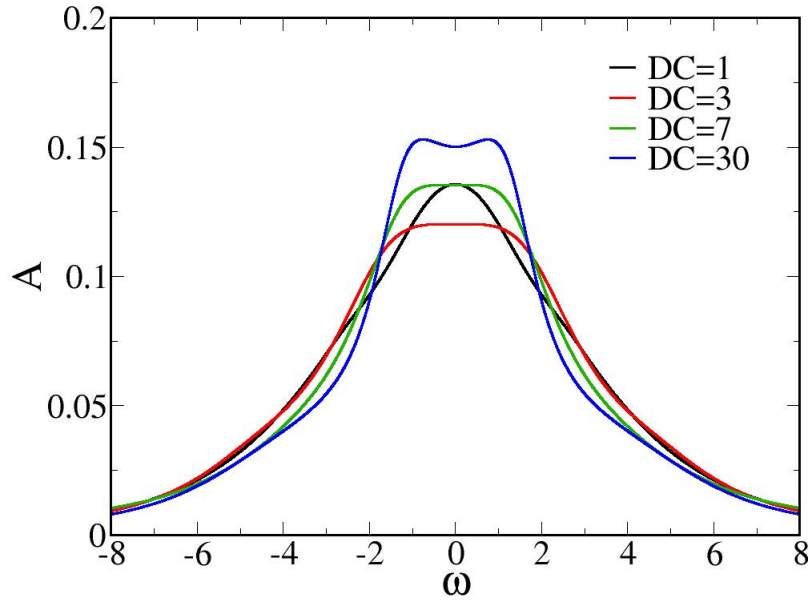

FIGURE 4.9. Evolution with DC field of the non-equilibrium spectral function $A(\omega, t_{av})$, evaluated at $t_{av} = 20$, in the $U = 4$ case. One more time, the effect of the dimensional crossover makes the spectral function develop a one-dimensional structure, even if the localization provided by U slows down this process.

different values of the carrier DC field (1, 3, 7, 30) in the $U = 4$ case, are reported in Figure 4.9. One more time, the spectral function $A(\omega)$ is always positive, as in the equilibrium case. Moreover, we note that the application of a large DC field
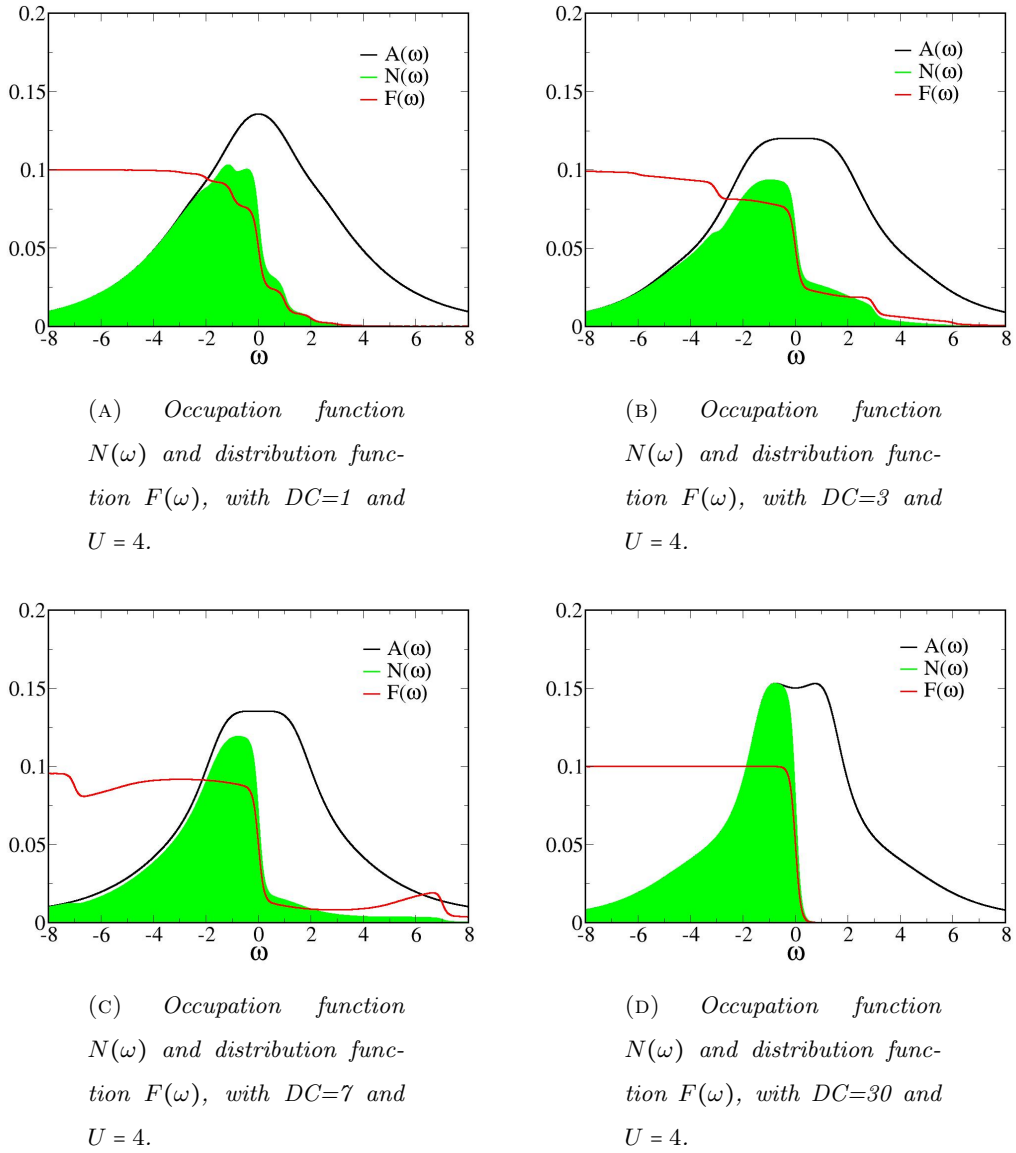
(A) *Occupation function $N(\omega)$ and distribution function $F(\omega)$, with DC=1 and $U = 4$.*

(B) *Occupation function $N(\omega)$ and distribution function $F(\omega)$, with DC=3 and $U = 4$.*

(C) *Occupation function $N(\omega)$ and distribution function $F(\omega)$, with DC=7 and $U = 4$.*

(D) *Occupation function $N(\omega)$ and distribution function $F(\omega)$, with DC=30 and $U = 4$.*

FIGURE 4.10. Out-of-equilibrium spectral functions, distribution functions and occupation functions of the $U = 4$ interacting system subjected to different DC carrier fields. Increasing the DC field, the distribution function approaches the Fermi-Dirac function. The resulting occupation (at high DC fields) traces the equilibrium one at finite temperature, with occupied electronic states below the Fermi level and unoccupied electronic states above it. One more time, a large DC field drives the dimensional crossover, that makes the system behave as in equilibrium.

affects the spectral function of the system; in fact, the initial bidimensional spectral function $A(\omega)$ acquires typical one-dimensional features, once again developing symmetrical Van Hove singularities at the edges of the reduced band.

We then repeat the calculations for the occupation and distribution functions, reported in Figure 4.10, for the $U = 4$ interacting case. One more time, increasing the carrier DC field the distribution function $F(\omega)$ approaches the Fermi-Dirac equilibrium one, and the occupation $N(\omega)$ tends to an equilibrium electronic occupation at finite temperature, as expected after the dimensional crossover.

In order to visualize the effects of the interaction U and the DC carrier field on the occupation function, we plot the profiles of the occupation functions for increasing carrier fields, both for $U = 0$ and $U = 4$, in Figure 4.11. The evolution with
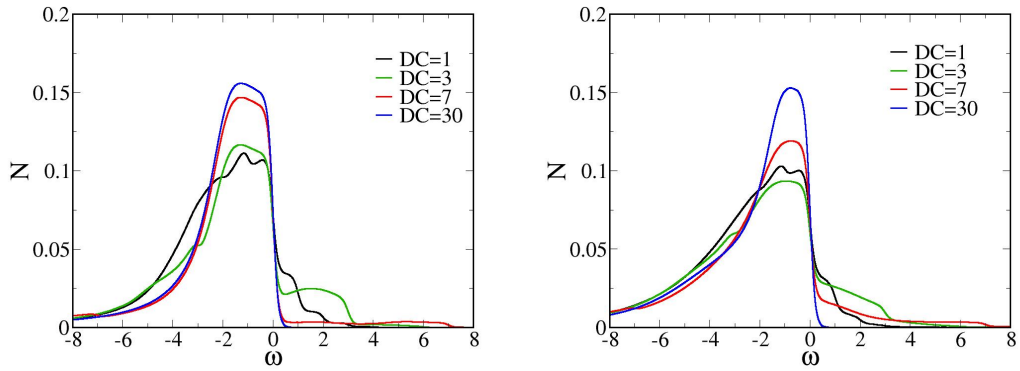
(A) *U=0 case. Increasing the carrier DC field, the occupation function near the Fermi level increases in heigth, letting the system transport more current.*

(B) *U=4 case. The behaviour of the occupation function near the Fermi level, as well as that of the current flowing in the system, is not linear with the DC field.*

FIGURE 4.11. Evolution with applied DC field of the occupation function $N(\omega)$ respectively at $U = 0$ and $U = 4$. The behaviour of the occupation function near the Fermi level with respect to the DC applied field determines the flow of current in the system, which is affected by the charge density at the Fermi level.

the carrier DC field of the occupation function $N(\omega)$ explains the behaviour of the flowing current in the system, both in case $U = 0$ and $U = 4$. In fact, the current density depends on the occupation of the low-energy levels of the system, because it is connected to the number of electronic states available near the Fermi level.

Increasing the DC carrier field, at $U = 0$ the carrier density near the Fermi level increases monotonically (see Figures 4.11a), as well as the electric current flowing in the system. When the interaction U is non-vanishing, the occupation near the Fermi level has a non-monotonous behaviour (see Figures 4.11b), descending and then going up when the carrier field increases. Viceversa, increasing U at fixed
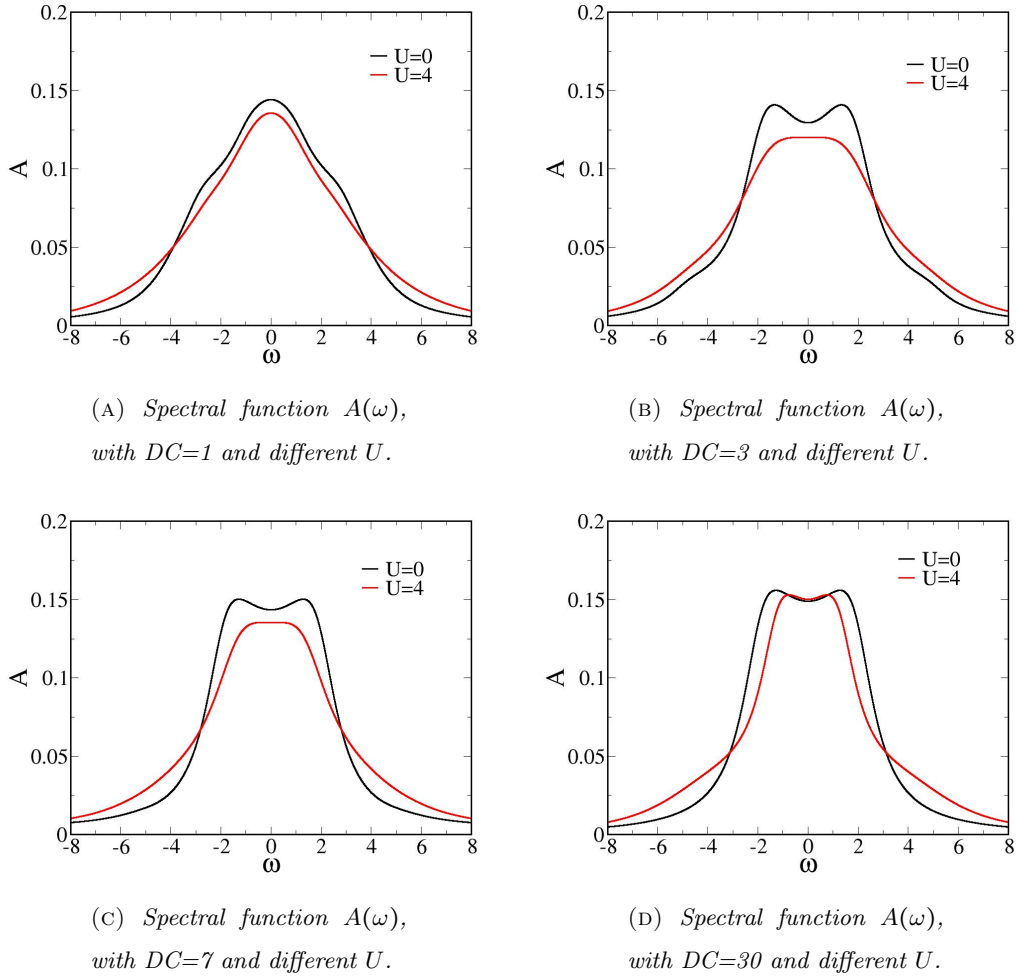

(A) *Spectral function $A(\omega)$, with DC=1 and different U.*

(B) *Spectral function $A(\omega)$, with DC=3 and different U.*

(C) *Spectral function $A(\omega)$, with DC=7 and different U.*

(D) *Spectral function $A(\omega)$, with DC=30 and different U.*

FIGURE 4.12. Out-of-equilibrium spectral functions of the system subjected to different DC carrier fields, both at $U = 0$ and $U = 4$. The evolution of $A(\omega)$ with field confirms the hypothesis of the dimensional crossover. In fact, the system acquires one-dimensional spectral features, and its spectral function is renormalized by U, as in the equilibrium case.

DC field, the spectral weight moves to higher energies, and the quasi-particle peak centred at the Fermi level shrinks, by lowering the available electronic states, localizing the system. This description supports the results found in Figure 4.4, that is

the current density is monotonous with the interaction U but non-monotonous with the field $\mathbf{E}$. The reason why at finite U the current decreases and then increases again to the asymptotic maximum, is that at low fields the electronic states initially are distributed non-linearly, according to the out-of-equilibrium $F(\omega)$. When the DC field is increased, the distribution approaches the Fermi-Dirac one, the carrier density increases as well as the current in the system. Thus, until the dimensional crossover has not happened yet (at low $\mathbf{E}_x$ fields), the current is favoured to flow in the x direction, because both the directions feel the localization caused by U, but only the x direction has enough energy (given by the field) to allow hopping. To sum up, when $\mathbf{E}_x$ comes out of the linear regime, correlated systems conduct worse with respect to non-correlated ones in the y direction, that is the steady-state current is monotonically decreasing with U, but non-monotonous with the carrier field $\mathbf{E}_x$.

In the end, we compare now the non-equilibrium spectral functions evaluated for the same DC field, by varying the interaction U, in Figure 4.12. Looking at Figure 4.12d, at high DC field (when the system has already experienced the dimensional crossover) the effect of the interaction U on the spectral function is the same as in equilibrium (see Figure 1.7). In fact, when the interaction U is switched on, the quasi-particle peak shrinks and the system localizes. Thus, this renormalization of the spectral function $A(\omega)$ at the Fermi level (occurring when U increases) can be considered as the final proof that the dimensional crossover transforms an out-of-equilibrium bidimensional problem in an equilibrium one-dimensional one.

2.2. Perpendicular DC-PULSE.

In this last section, we finally investigate the case of two different perpendicular fields applied on the system, a DC probe directed along the y axis, and a pulse carrier field in the x direction. One more time, we choose to work at $\Lambda = 0.3$, in order to obtain a stable steady-state current in a quite brief time window.

Similarly to the last case, we looked at the conductivity of the system, measuring the current $\mathbf{J}_y$ vs the applied pulse carrier field $\mathbf{E}_x$. We use a DC probe $\mathbf{E}_y = 0.1$, varying the amplitude of the carrier pulse field $\mathbf{E}_x$. The question to answer is: is the pulse field able to induce a dimensional crossover in the system? If the fields are orthogonal, their effects are decoupled, and the effect of the pulse on the system in terms of dimensional crossover can be investigated.

Due to the transient character of the pulse signal, we repeat the procedure used for

the parallel DC+PULSE fields, by evaluating the time integral ΔQ_y of the difference curve obtained subtracting the DC current to the DC+PULSE current, always collecting the current along the y direction. ΔQ_y represents the difference of flowing charge between the DC+PULSE case and the single probe case, in the simulation time interval $t = 40$ (long enough to allow the relaxation of the system with the thermal bath). The results, both at $U = 0$ and at finite values of U, are reported in Figure 4.13. We firstly note how the general behaviour is similar to Figure 4.4,
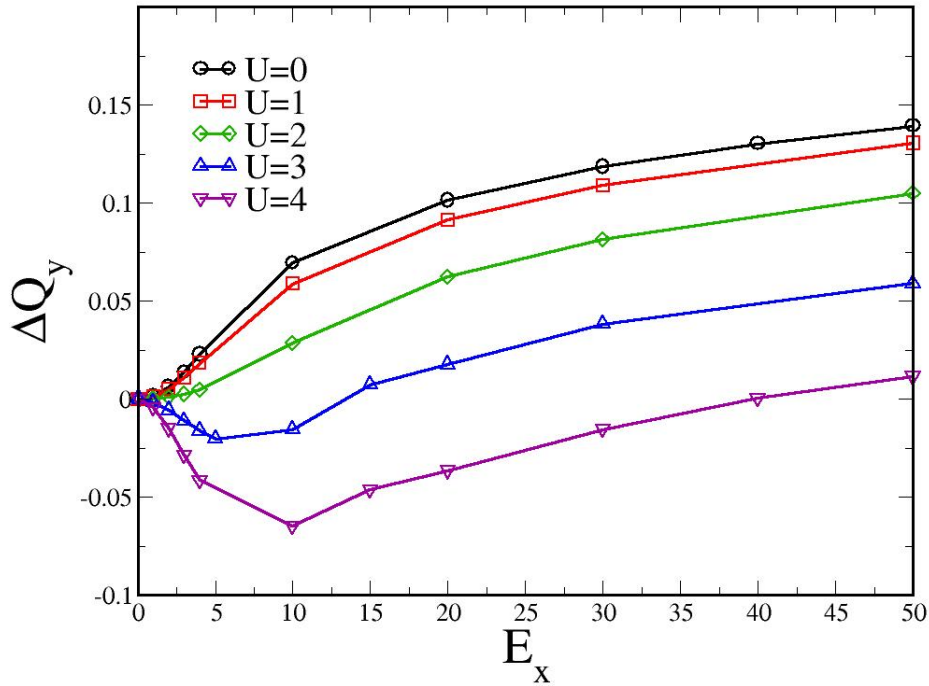

FIGURE 4.13. Difference of flowing charge ΔQ_y vs the pulse field $\mathbf{E}_x$, varying the interaction U. ΔQ_y is the time integral of the difference curve between the DC+PULSE current and the DC current alone, and represents the excess of flowing charge caused by the superposition of the electric fields.

even if the curves do not show an asymptotic maximum. However, even here the interaction U (responsible for electronic localization) competes with the dynamical localization caused by the carrier field. In fact, the correlation dampens the flowing charge, delaying the effects of the dimensional crossover. Actually, we are unable to set higher amplitude pulse fields, because the system would be heated to much by the pulse itself, invalidating the semi-classical approximation. However, the general behaviour of Figure 4.13 suggests the existence of a pulse driven dimensional
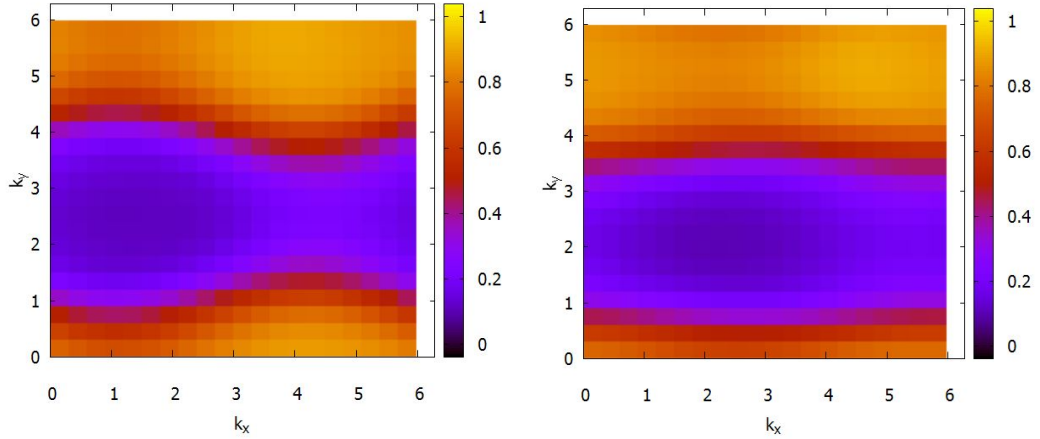
(A) *Fermi surface at t = 7 (beginning of the pulse).*

(B) *Fermi surface at t = 11 (centre of the pulse).*
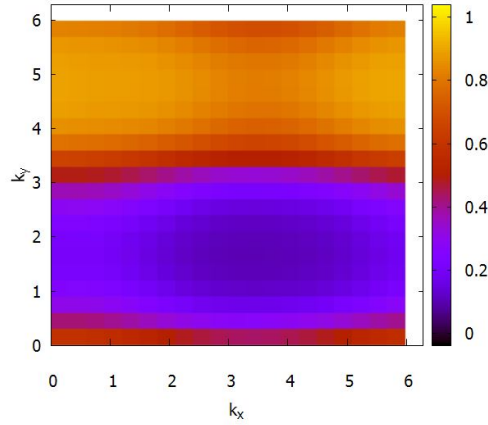
(C) *Fermi surface at t = 15 (end of the pulse).*

FIGURE 4.14. Time evolution of the Fermi surface of a system driven by a pulse field **E** = 40. Despite the transient character of the pulse signal, the Fermi surface tends to become completely one-dimensional, losing the dependence on k_x, although only at the pulse time scale. Moreover, it experiences a shift along the k_y direction, caused by the probe field.

crossover, even if less clean than the one observed with the DC field [7][8].

This weaker effect can be explained thinking to the nature of the pulse field, which is a transient signal, oscillating in time. For both this reason, the pulse driven dimensional crossover can be considered as a transient and non-effective effect (with

respect to the DC field). In order to prove the existence of a pulse driven dimensional crossover, we apply a strong pulse field $\mathbf{E}_x = 40$ on the system, keeping all the other parameters constant, and we compute the time-evolution of the Fermi surface. One more time, we investigate the system at different times ($t = 7, 11, 15$), which ideally represents the temporal beginning, the centre and the end of the pulse field. The time evolution of the Fermi surface of the system is reported in Figure 4.14.

As expected, the Fermi surface of the bidimensional system subjected to a strong pulse field tends to become one-dimensional, although for a restricted time, that corresponds to the pulse duration. This fact confirms our hypothesis that the pulse field can induce transient dimensional crossover in a bidimensional system, by modifying temporarily its bidimensional properties to one-dimensional ones.

Moreover, we note a k_y-shift of the Fermi surface caused by the DC field $\mathbf{E}_y = 0.1$, which at long time tends to move the Fermi surface along the y direction. We now
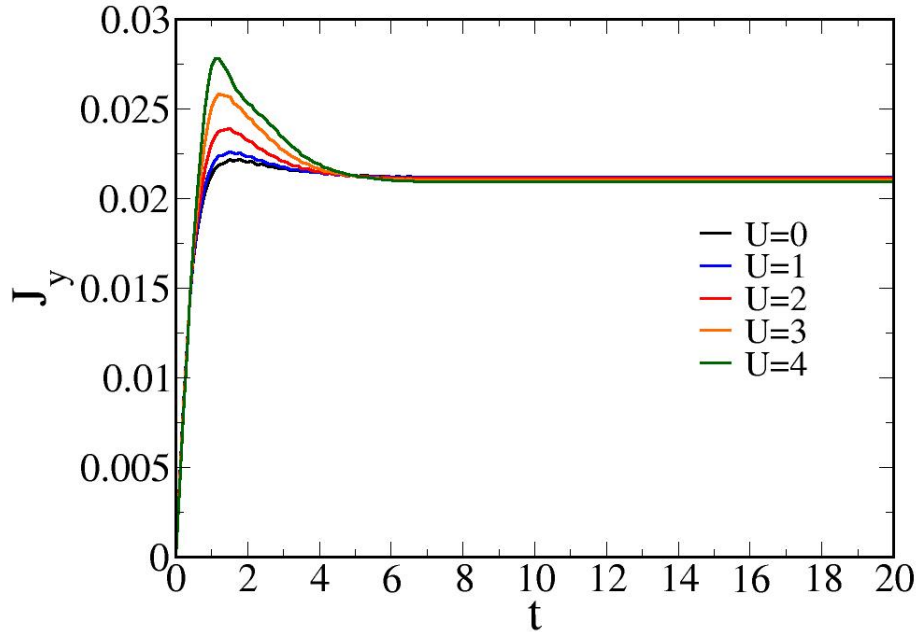

FIGURE 4.15. NESS current $\mathbf{J}_y(t)$ obtained with the only probe field $\mathbf{E}_y$, varying U. The final value of the current (when the system is completely thermalized) is universal in U, confirming that the probe field lays in the linear regime.

check if our probe DC field is really in the linear regime of fields. In order to do that, let us consider that in the linear regime the steady-state current does not depend

(A) *Time-evolution of the spectral function $A(\omega)$, with PULSE=4 and $U = 0$.*

(B) *Time-evolution of the spectral function $A(\omega)$, with PULSE=10 and $U = 0$.*

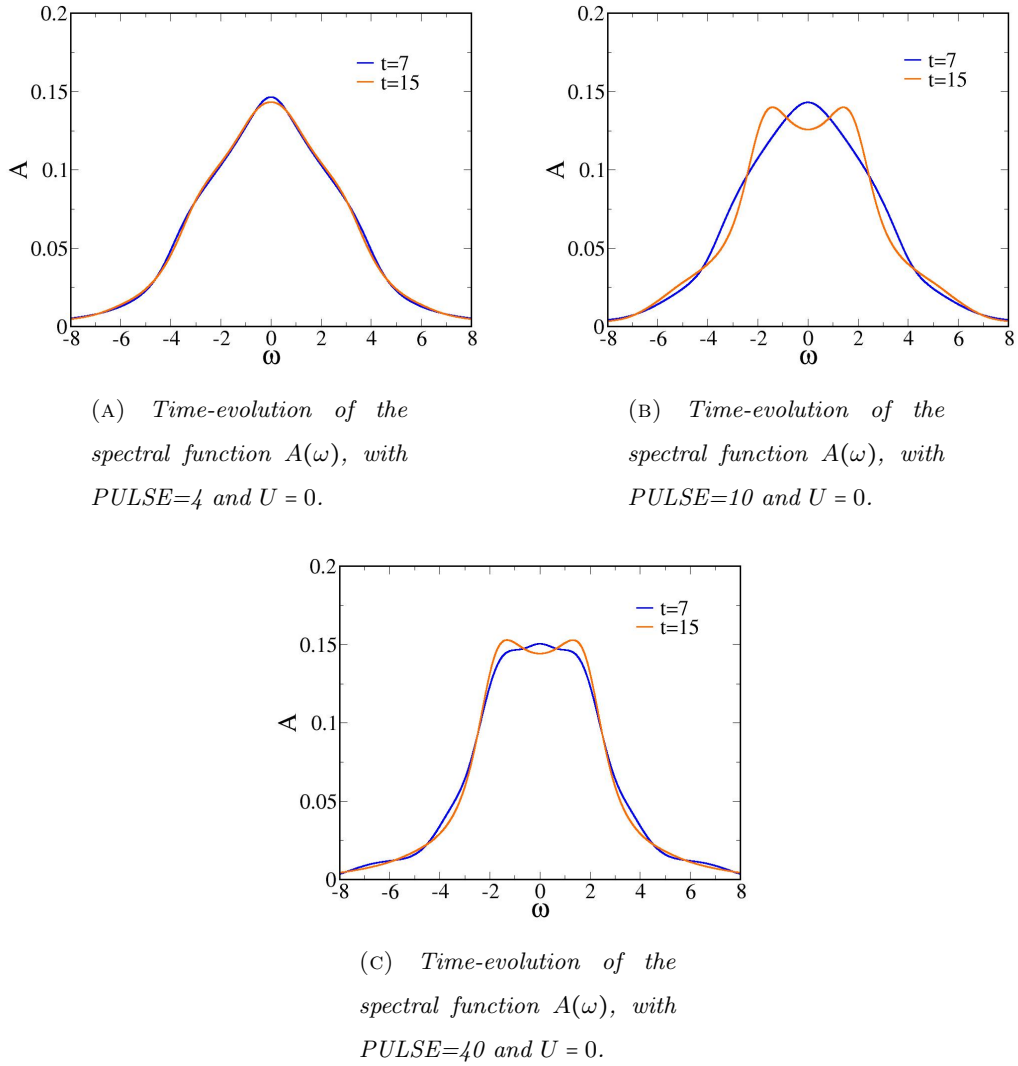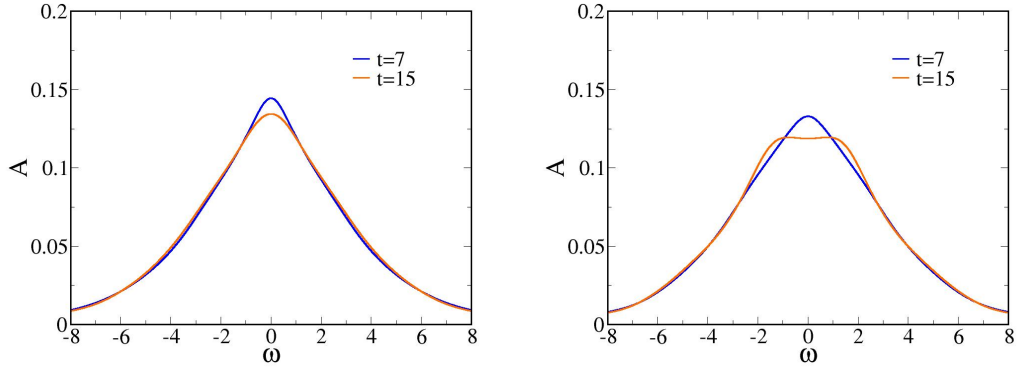(C) *Time-evolution of the spectral function $A(\omega)$, with PULSE=40 and $U = 0$.*

FIGURE 4.16. Out-of-equilibrium spectral functions of the $U = 0$ system subjected to different PULSE carrier fields, evaluated before and after the application of the pulse ($t_{av} = 7$ and $t_{av} = 15$). One more time, $A(\omega)$ acquires typical one-dimensional spectral features. The evolution of $A(\omega)$ with the pulse field represents a signal of pulse-driven dimensional crossover.

on the interaction U. Viceversa, out of the linear regime, the value of the steady-state current is a decreasing function of the interaction U. During our calculations, we always subtract the DC current from the DC+PULSE one; if our probe field would not be in the linear regime, we would subtract different quantities depending on the interaction U. In other words, if the probe would not be in linear regime, we would observe different asymptotes at large carrier field, one for every different

value of U. In Figure 4.15, we report the static current $\mathbf{J}_y(t)$ obtained at different values of U. The steady-state current value is almost constant with the interaction U, as we expected from a probe in the linear regime of fields. Finally, we examine

(A)   *Time-evolution of the spectral function $A(\omega)$, with PULSE=4 and U = 4.*

(B)   *Time-evolution of the spectral function $A(\omega)$, with PULSE=10 and U = 4.*
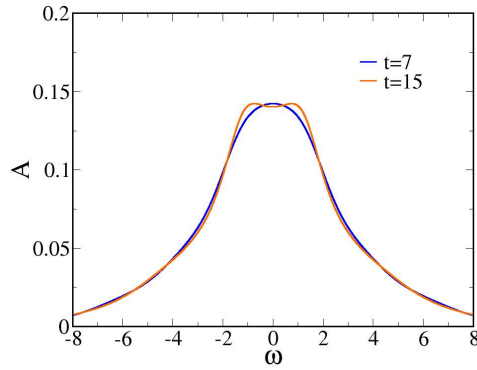
(C)   *Time-evolution of the spectral function $A(\omega)$, with PULSE=40 and U = 4.*

FIGURE 4.17. Out-of-equilibrium spectral functions of the U = 4 system subjected to different PULSE carrier fields, evaluated before and after the application of the pulse (t_{av} = 7 and t_{av} = 15). Even with the presence of interaction U = 4, $A(\omega)$ acquires one-dimensional spectral features, although at higher electric fields. One more time, the evolution of $A(\omega)$ with pulse field represents a signal of pulse-driven dimensional crossover, whose effects on the system are damped by the interaction U.

again the non-equilibrium spectral properties in the case of a pulse-carried system,

at different oscillating field amplitudes. We choose again the coupling $\Lambda = 0.3$, for the reasons already explained. In Figures 4.16 and 4.17, we plot the evolution of
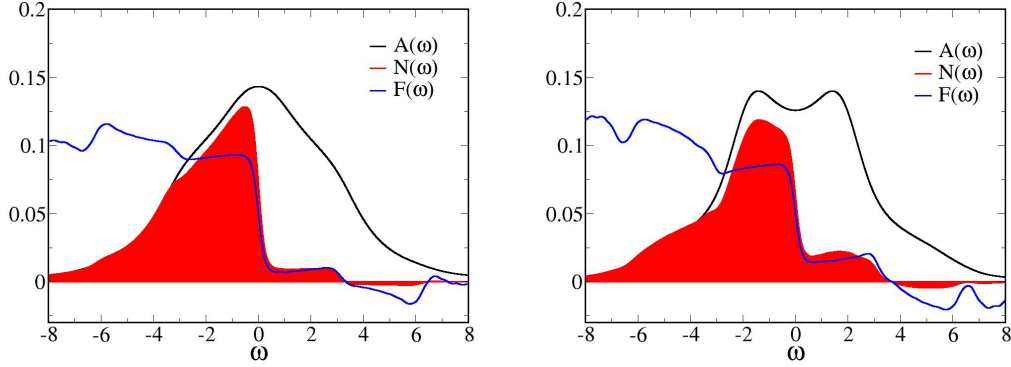
(A)   Occupation   function $N(\omega)$ and distribution function $F(\omega)$ at pulse field $\boldsymbol{E} = 4$.

(B)   Occupation   function $N(\omega)$ and distribution function $F(\omega)$ at pulse field $\boldsymbol{E} = 10$.
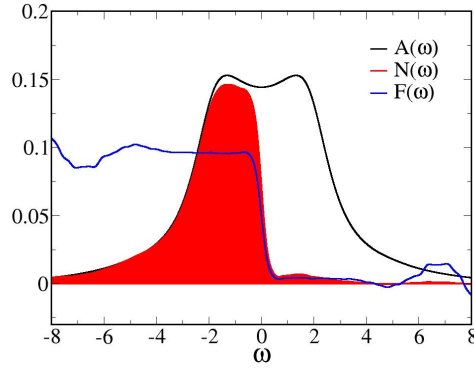
(C)   Occupation   function $N(\omega)$ and distribution function $F(\omega)$ at pulse field $\boldsymbol{E} = 40$.

FIGURE 4.18. Evolution with applied PULSE field of the occupation function $N(\omega)$ and distribution function $F(\omega)$ at $U = 0$. Increasing the pulse field, the occupation function near the Fermi level increases, letting the system transport more current. In the range $[-2, +2]$, the distribution function approaches the Fermi-Dirac equilibrium one, confirming the hypothesis of a pulse-driven dimensional crossover.

the non-equilibrium spectral function $A(\omega)$ of a system subjected to pulse fields of amplitude 4, 10, 40, both at $U = 0$ and $U = 4$.

Being the pulse a transient oscillating signal, the spectral function of course depends on time.

We choose to represent the spectral functions taken at $t_{av} = 7$ and $t_{av} = 15$, ideally considered as the beginning and the ending point of the pulse signal, in order to investigate the effect of the dimensional crossover on the system.

Looking at Figures 4.16 and 4.17, both in $U = 0$ and $U = 4$ case the spectral function acquires one dimensional features (van Hove singularities) at $t_{av} = 15$, after the action of the pulse on the system, with respect to $t_{av} = 7$, when the pulse has not impinged on it yet. When the interaction U is switched on, the system becomes more localized and the one-dimensional features of the spectral function are less pronounced, as visible in Figure 4.17. At high pulse fields, the effect of the dimensional crossover is thus damped by U, that slows down the process of dynamical localization. In fact, the localization introduced by the interaction U tends to immobilise the electrons, contrasting the effect of the dimensional crossover. In order to explain the raise of the flowing charge at high carrier pulse fields visible in Figure 4.13, we plot the distribution and occupation functions varying the pulse carrier field $\mathbf{E}_x$, looking at the effects caused by the pulse field on the system spectral features. One more time, we choose $\Lambda = 0.3$, and we compute all the spectral quantity at $t_{av} = 15$, after the effect of the pulse on the system. For both $U = 0$ and $U = 4$, we select three different pulse amplitude values (4, 10, 40). The results for the non-interacting case $U = 0$ are shown in Figure 4.18, and for the $U = 4$ case in Figure 4.19. Even if the carrier field is a transient pulse, the system experiences a dimensional crossover, although transient in time. In fact, for the highest investigated pulse field amplitude (40), the non-equilibrium distribution function $F(\omega)$ approaches the Fermi-Dirac one, that describes an equilibrium system. Of course the effect is not exact as in the DC carrier field case [7]; in fact, at very high energy the distribution function becomes also negative, a completely non-equilibrium effect that has no explanation in the equilibrium theory.

In conclusion, we numerically showed that a pulse field can drive a dimensional crossover in an Hubbard model, although transient in time and not effective as the DC-driven one [7][8].
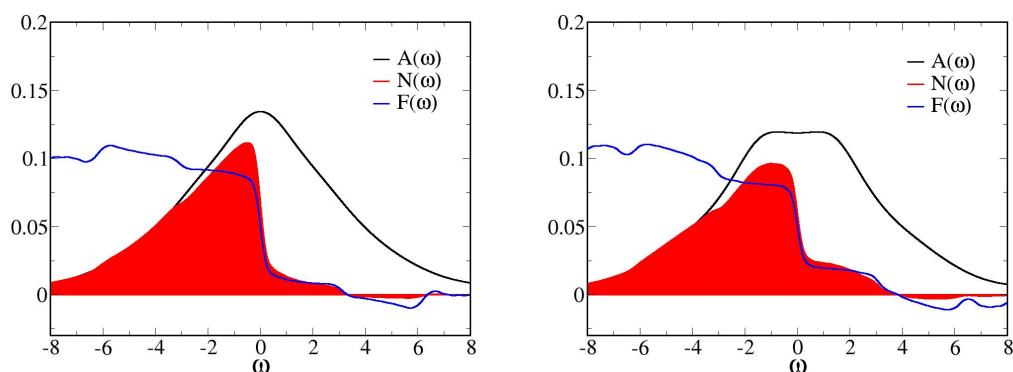
(A) *Occupation function $N(\omega)$ and distribution function $F(\omega)$ at pulse field $\boldsymbol{E}$ = 4.*

(B) *Occupation function $N(\omega)$ and distribution function $F(\omega)$ at pulse field $\boldsymbol{E}$ = 10.*
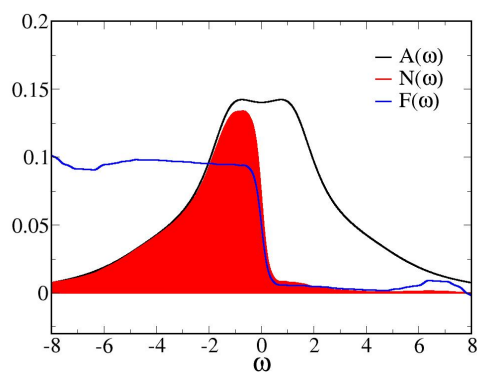
(C) *Occupation function $N(\omega)$ and distribution function $F(\omega)$ at pulse field $\boldsymbol{E}$ = 40.*

FIGURE 4.19. Evolution with the applied PULSE field of the occupation function $N(\omega)$ and distribution function $F(\omega)$ at U = 4. Increasing the pulse field, the occupation function near the Fermi level increases, letting the system transport more current. Moreover, the distribution function approaches the Fermi-Dirac distribution, describing an equilibrium system.

Conclusions

The objective of the present work was to investigate the effects of the combination of static electric fields and an intense pulse fields on the electric transport in a strongly correlated metal, coupled with an external heat bath that allows to move from coherent transport regime to diffusive transport regime.

We introduced the equilibrium dynamical mean field theory (DMFT) formalism, in order to describe the metal-to-Mott insulator phase transition, occurring in strongly correlated materials. We then introduced the non-equilibrium variant of the DMFT formalism (NEQ-DMFT), in order to investigate the non-equilibrium dynamics of a driven Hubbard model coupled to an external thermostat. We found that the presence of an external thermal bath was fundamental to reach a non-equilibrium steady-state (NESS) with a finite flowing current. In addition, we studied the properties of the NESS and their dependence respectively on the coupling to the bath Λ, on the external electromagnetic field $\mathbf{E}$ and on the strength of the interaction U.

Moreover, we were interested in the effects of large electric fields on a bidimensional lattice system, and we found that the application of a large DC field on a periodic system induces the formation of a Wannier-Stark ladder, localizing the electronic energy levels.

Finally, in the last part of our work we investigated the dynamics of a correlated Hubbard model driven out-of-equilibrium by a specific superposition of DC and pulse electric fields. In particular, we focused on the phenomenon of the dimensional crossover, obtaining numerical evidences that a bidimensional system undergoes a dimensional reduction and behaves as an equilibrium system when a large pulse field is applied on it. This important result proves that even an ultra-short pulse with a temporal duration of few femtoseconds, and not only a DC field, can induce a dimensional crossover in the system, although transient.

Moreover, we found that the directionality of the fields plays a crucial role in determining the physical properties of the system, such as the flowing electric charge. In particular, we managed to obtain an excess of flowing charge in the direction of

application of a DC probe, by applying a varying pulse field along the orthogonal direction. This result can be considered of great interest also from an experimental point of view, because it allows to control photo-current in bidimensional correlated systems, simply directing the external electromagnetic fields one orthogonal to the other.

The possibility to manipulate correlated systems with intense pulse fields would allow to control their electronic quantum properties, thus paving the way to exploit coherent transport phenomena in correlated oxides, which are key materials for future implementation of quantum technologies.

Bibliography

[1] M. Eckstein and P. Werner. "Ultra-fast photo-carrier relaxation in Mott insulators with short-range spin correlations". In: *Scientific Reports* (2016).

[2] M. Eckstein and P. Werner. "Ultrafast Separation of Photodoped Carriers in Mott Antiferromagnets". In: *Physical Review Letters* (2014).

[3] C. Giannetti et al. "Disentangling thermal and nonthermal excited states in a charge-transfer insulator by time- and frequency-resolved pump-probe spectroscopy". In: *Phys. Rev. B 80, 235129* (2009).

[4] C. Giannetti et al. "Ultrafast optical spectroscopy of strongly correlated materials and high-temperature superconductors: a non-equilibrium approach". In: *Advances in Physics* 65.2 (2016), pp. 58–238.

[5] M. Eckstein and P. Werner. "Photoinduced States in a Mott Insulator". In: *Phys. Rev. Lett. 110, 126401* (2013).

[6] A. Georges et al. "Dynamical mean-field theory of strongly correlated fermions systems and the limit of infinite dimensions". In: *Reviews of Modern Physics* 68 (1996).

[7] C. Aron, G. Kotliar, and C. Weber. "Dimensional Crossover Driven by an Electric Field". In: *Phys. Rev. Lett. 108, 086401* (2012).

[8] C. Aron, G. Kotliar, and C. Weber. "Proof of the Electric Field Driven Dimensional Reduction". In: *Phys. Rev. Lett. 108, 086401* (2012).

[9] P. Coleman. *Introduction to Many-Body Physics*. UK: Cambridge University Press, 2016.

[10] E. Pavarini et al. *Quantum Materials: Experiments and Theory*. Forschungszentrum Jülich GmbH, Institute for Advanced Simulation, 2016.

[11] Giuseppe Grosso and Giuseppe Pastori Parravicini. *Solid State Physics*. Elsevier, 2014.

[12] B. Radzimirski and R.J. Wojciechowsy. "Dynamical Mean Field within Iterative Perturbation Theory". In: *Acta Physica Polonica A* (2007).

[13] L. V. Keldysh. "Diagram technique for nonequilibrium processes". In: *Soviet Physics Jetp* (1965).

[14]   H. Aoki et al. "Nonequilibrium dynamical mean-field theory and its applications". In: *Reviews of Modern Physics* (2014).

[15]   M. Eckstein et al. "Hopping on the Bethe lattice: Exact results for densities of states and dynamical mean-field theory". In: *Phys. Rev. B 71, 235119* (2005).

[16]   M. Scüler et al. "NESSi: The Non-Equilibrium Systems Simulation package". In: *Computer Physics Communications* (2019).

[17]   John H. Davies. *The physics of low-dimensional semiconductors, an introduction.* Cambridge University Press, 1998.

[18]   A. Amaricci et al. "Approach to a stationary state in a driven Hubbard model coupled to a thermostat". In: *Physical review B 86, 085110* (2012).

[19]   J.E Han. "Solution of electric-field-driven tight-binding lattice coupled to fermion reservoirs". In: *Phys. Rev. B 87, 085119* (2013).

[20]   J. Skolimowski, A. Amaricci, and M. Fabrizio. "The perils of minimal coupling to electromagnetic field in quantum many-body systems". In: *Phys. Rev. B 101, 121104* (2020).

[21]   A.V. Joura, J.K. Freericks, and A.I. Lichtenstein. "Long-lived nonequilibrium states in the Hubbard model with an electric field". In: *Physical Review B* 91 (2015).

[22]   M. Eckstein and P. Werner. "Damping of Bloch Oscillations in the Hubbard Model". In: *Phys. Rev. Lett. 107, 186406* (2011).

[23]   J.K. Freericks. "Quenching Bloch oscillations in a strongly correlated material: Nonequilibrium dynamical mean-field theory". In: *Physical Review B* (2008).

[24]   C. Zener. "A Theory of the Electrical Breakdown of Solid Dielectrics". In: *Proceedings of the Royal Society of London. Series A, Containing Papers of a Mathematical and Physical Character* (1934).

[25]   M. Glück et al. "Calculation of Wannier-Bloch and Wannier-Stark states". In: *The european physical journal* (1998).

[26]   J. Rammer. *Quantum Field Theory of Non-Equilibrium States.* Cambridge University Press, 2007.

[27]   O. P. Matveev et al. "Nonequilibrium response of an electron-mediated charge density wave ordered material to a large dc electric field". In: *Physical review B 93, 045110* (2016).

[28]   C. M. Kropf et al. "Electric-field assisted optimal quantum transport of photo-excitations in polar heterostructures". 2020.

[29] J. Li and M. Eckstein. "Nonequilibrium steady-state theory of photodoped Mott insulators". 2020.

[30] K. Balzer et al. "Nonthermal Melting of Néel Order in the Hubbard Model". In: *Physical Review X* (2015).

[31] G. Sangiovanni et al. "Static versus dynamical mean-field theory of Mott antiferromagnets". In: *Physical Review B* (2006).

[32] C. Taranto et al. "Signature of antiferromagnetic long-range order in the optical spectrum of strongly correlated electron systems". In: *Physical Review X* (2012).

[33] H.F. Fotso and J.K. Freericks. "Characterizing the Nonequilibrium Dynamics of Field-Driven Correlated Quantum Systems". May 2020.

[34] C.M. Kropf et al. "Towards high-temperature coherence-enhanced transport in few-atomic layers heterostructures". In: *Phys. Rev. B 100, 035126* (July 2019).

[35] E.H. Lieb and F.Y. Wu. "Absence of Mott transition in an exact solution of the short-range, one-band model in one dimension". In: *Physical Review Letters* 20.25 (June 1968).

[36] Y. Murakami and P Werner. "Nonequilibrium steady states of electric field driven Mott insulators". In: *Physical Review B* 98 (Aug. 2018).

[37] C. Giannetti, F. Cilento, S. Dal Conte, et al. "Revealing the high-energy electronic excitations underlying the onset of high-temperature superconductivity in cuprates". In: *Nature communications* (2011).

[38] D. Fausti et al. "Light-Induced Superconductivity in a Stripe-Ordered Cuprate". In: *Science, Vol. 331, Issue 6014* (2011).

[39] M. Eckstein, T. Oka, and P. Werner. "Dielectric Breakdown of Mott Insulators in Dynamical Mean-Field Theory". In: *Phys. Rev. Lett. 105, 146404* (2010).